UNIVERSIDADE ESTADUAL PAULISTA
"JÚLIO DE MESQUITA FILHO"
Campus de Ilha Solteira

PROGRAMA DE PÓS-GRADUAÇÃO EM CIÊNCIA DOS MATERIAIS

"Molecular dynamics investigation of the mechanical, thermal and surface properties of tricalcium silicate and its early hydration"

JÉRÔME CLAVERIE

Orientador: Prof. Dr. João Manuel Marques Cordeiro
Co-Orientador: Prof. Dr. Fabrice Bernard

Tese apresentada ao Institut National des Sciences Appliquées - INSA – Rennes, França, para obtenção do título de Doutor em Ciência dos Materiais.

Área de conhecimento: Física da Matéria Condensada

Ilha Solteira – SP
dezembro/2019

unesp

UNIVERSIDADE ESTADUAL PAULISTA

Câmpus de Ilha Solteira

CERTIFICADO DE APROVAÇÃO

TÍTULO DA TESE: Molecular dynamics investigation of the mechanical and thermal properties and of the early hydr ation of tricalcium silicate

AUTOR: JÉRÔME CLAVERIE
ORIENTADOR: JOAO MANUEL MARQUES CORDEIRO

Aprovado como parte das exigências para obtenção do Título de Doutor em CIÊNCIA DOS MATERIAIS, área: Física da Matéria Condensada pela Comissão Examinadora:

Prof. Dr. JOAO MANUEL MARQUES CORDEIRO
Departamento de Física e Química / Faculdade de Engenharia de Ilha Solteira

Prof. Dr. ANDREY KALINICHEV
Departamento Subatech / Mines de Nantes, França

Prof. Dr. ALI ZAOUI
Departement Mécanique Cité Scientifique / Université de Lille, França

Prof. Dr. RICARDO GARGANO
Departamento de Física / Universidade de Brasília - UnB

Prof. Dr. FABRICE BERNARD
Departamento LGCGM / INSA de Rennes, França

Prof. Dr. SIHAM KAMALI-BERNARD
Departamento LGCGM / INSA de Rennes, França

Ilha Solteira, 10 de dezembro de 2019

FICHA CATALOGRÁFICA
Desenvolvido pelo Serviço Técnico de Biblioteca e Documentação

C617m

Claverie, Jérôme.
Molecular dynamics investigation of the mechanical, thermal and surface properties of tricalcium silicate and its early hydration = Investigação da dinâmica molecular das propriedades mecânicas, térmicas e de superfície do silicato tricálcico e sua hidratação precoce / Jérôme Claverie. -- Ilha Solteira: [s.n.], 2019
142 f. : il.

Tese (doutorado) - Universidade Estadual Paulista. Faculdade de Engenharia de Ilha Solteira. Área de conhecimento: Física Da Matéria Condensada, 2019

Orientador: João Manuel Marques Cordeiro
Co-orientador: Fabrice Bernard
Inclui bibliografia

1. Silicato tricálcico. 2. Hidratação. 3. Dinâmica molecular. 4. Energia de clivagem. 5. Interface.

João Josué Barbosa
Serviço Técnico de Biblioteca e Documentação
Diretor Técnico
CRB 8-5642

Acknowledgements

First, I want to thank God for giving me the opportunity to realize this thesis, for having discovered a field that I really like and having learned a lot of things in such a short period of time. He put wonderful people in my life who helped me when a needed it the most.

Thanks to my beautiful wife Katriny who encouraged me every moment of this thesis, and gave me the strength to go through this work. Actually we went through this together. She had the patience to support me all the time when this project was the only thing on my mind.

Thanks to my parents Christine and Bernard and my brother Bertrand, for being an amazing family with whom I acquired a curiosity about life and science. I am grateful to have such an open minded family. All the conversations we had about life, sciences and philosophy were not in vain. Thanks to all my family in France and in Brazil for having supported me and giving me love at every moment.

Thanks to my amazing supervisors, Fabrice, Siham and João, they gave me all the support I needed, not only scientifically, but above all humanely. I had difficulties to believe in my abilities and the confidence they had in me and my works helped me a lot. I can not thank you enough.

Of course, I would like to thank all the people I have met in Brazil and in France, who directly or indirectly participated to this thesis. Thanks to Douglas for its help with Linux, that I did not know when I started this work. Thanks to Glauco for having introduced me to molecular dynamics, for all the discussions about biochemistry, science in general, and life in general. Thanks to Luciano for being a reference for me as a young researcher, and having influenced me in going deep in science and studies. Thanks to my Cambodians friends Yeak Leang, Sok Visal, Sounean and to all the students and staff of the LGCGM. Thanks to Baladji

Raghavan for our long discussions about science, fitness, healthiness and many other things. Thanks to Laurent Pedesseau for his kindness and for having responding to all my questions about DFT and surface science. Thanks to Benoît Khamchane for his gentleness and technical support.

To finish, I would like to thank all the specialists I have contacted during this thesis. As a beginner in atomistic simulation, I had the chance to encounter, or contact references in the field. Thanks very much to Andrey Kalinichev for having received me at his laboratory when I was starting this project and for having responded to all my questions with patience. Thanks to Hegoi Manzano, for giving me support and encouraging me. Thanks to Hendrik Heinz and to Gabriele Tocci for their useful advices.

Abstract

The energetical and environmental problematic related to the cement production is a very sensitive issue. As every other field, the construction industry must go through drastic change in the design of concrete and cement-based materials. The understanding of the physical and chemical properties of the Portland cement (PC) clinker is important to improve its design. Tricalcium silicate C_3S, or alite, is the main phase of PC clinker and has been largely studied since it is the first responsible for the strength development of the cement paste. On the other hand, the development of computational methods at the molecular scale has made possible the modelling of structural, dynamical and energetic properties, sometimes hardly measurable by experimental means. Such methods are relatively new in the field of cement chemistry, but have been increasingly employed over the last 15 years. In this project, density functional theory (DFT), classical molecular dynamics (MD), and *ab initio* molecular dynamics (AIMD) are employed towards a better understanding of mechanical, thermal, and superficial properties of monoclinic C_3S, as well as C_3S/water interface features. The present thesis consists of five chapters.

The first chapter presents a review of the literature on the chemistry of cement, and more particularly on the hydration process modeling. The various phases which compose the Portland cement clinker are introduced, then the the different polymorphs of C_3S are described, in particular the M_1 and M_3 forms, which are studied in this thesis. Then, several models of hydration are discussed, from the first single particle models, to the last attempts of investigations at the atomic scale.

The second chapter provides an overview of the fundamental principles related to atomistic simulations. It describes the fundamentals of calculations based on the electronic density in many particle systems. The Density Functional Theory (DFT) revolutionized the study of these

systems since it considers the electronic density as only calculation variable, greatly reducing the calculation time. The classical molecular mechanics is then introduced, with the notion of fields of empirical forces to describe interatomic forces. Then, the calculation methods based on the minimization of energy are explained, as well as the molecular dynamics (MD), where the integration of Newton's equation of motion allows to simulate a system at finite temperature. The principles of *ab initio* molecular dynamics (AIMD), based on calculations of interatomic forces by DFT, are explained. Then some concepts of statistical mechanics, important in MD, are introduced. Finally, different force fields, already used to describe the C_3S/water interface and the initial hydration of C_3S are reviewed.

The third chapter presents the results of calculations of cleavage energy, and of mechanical and thermal properties of C_3S M_1 and M_3. The elastic constants are firstly calculated from the stiffness matrices, using the Voigt-Reuss-Hill homogenization method. These calculations are made by a static method, minimizing the energy of the unit cell at each deformation step. In addition, the calculation of the bulk modulus is performed by equilibrium molecular dynamics (EMD) under different hydrostatic pressure. The stress-strain curves are also obtained by non-equilibrium MD (EMD), applying a continuous deformation during the dynamics of the system. The elastic constants are also deduced from these calculations. The specific heat is determined by a direct method, from the rate of change of enthalpy as a function of the temperature of the system, constant pressure. The expansion coefficients are also calculated according to the variation of the volume with respect to the temperature under the same conditions. A more accurate method, based on the density of phonon states (DOS) is employed. DOS are calculated from the Fourier transform of the autocorrelation function of atomic velocities. In general, the calculated mechanical and thermal properties were in good agreement with the experimental measurements. Finally, the cleavage energies of C_3S M_1 and M_3 were calculated from the difference in energy of unified and cleaved systems. The superficial ions are relaxed to their minimum energy configuration applying steep temperature gradients. The equilibrium shapes of the M_1 and M_3 crystals are constructed from the energies calculated, employing the Wulff construction method, which is based on the minimization of free energy during crystal growth.

The fourth chapter presents a study by MD of the behavior of interfacial water as a function of the degree of hydration of the (040) surface of the M_3 C_3S, with a hydration model including the typical range of pH values of cement solutions. The interface energy is calculated according to the hydration degree of the surface. The structure and dynamics of the water molecules at the interface are evaluated by analysis of the obtained trajectories. Atomic densities at the interface, as well as the different binding modes of water molecules on the surface are highlighted. The orientation of water molecules and coordination spheres of the different chemical species present at the interface are analyzed. The dynamics of water molecules is quantified from the diffusion coefficient as a function of their distance from the C_3S surface. Analyses also make possible the quantification of the number and the type of hydrogen bond at the interface, as well as their life time. It is observed that, during hydration, the behavior of the water at the interface changes radically. The hydrogen bond network existing between the water molecules in contact with the anhydrous C_3S decomposes upon protonation of oxide ions and silicates.

The fifth chapter presents an AIMD study of proton transfers at the C_3S/water interface, on the same surface and the same polymorph as previously. Three types of hydroxyl groups are analyzed: hydroxides formed on oxide ions, hydroxyls in silanol groups and hydroxides resulting from the dissociation of water molecules. Hydroxides formed on oxide ions are very stable. Conversely, the number of two other types fluctuate according to proton transfers. These transfers have been quantified in terms of frequency and energy barrier. Furthermore, the importance of the environment of the superficial oxide ions on their protonation, this parameter was not considered in the previously used model, which only account for the pKa of hydroxide and silicic acid in solution. In addition, analyses show that the orientation of water molecules on the surface greatly influenced by its topology. Electron density analysis allows to highlight regions of abundance depletion of electrons due to the adsorption of water molecules, and occurring during proton exchanges. The size of these regions around hydroxyl groups is a function of the stability of the group. Generally speaking, the results obtained in this thesis allow for a better understanding of the behavior of C_3S at the atomic scale and its early hydration, occurring systematically even before mixing with water.

Keywords: Tricalcium silicate. Hydration. Molecular dynamics. Cleavage energy. Interface.

Resumo

A produção de cimento envolve questões energéticas e ambientais muito relevantes. Em função disso, a indústria da construção deve sofrer mudanças radicais na concepção de concreto de materiais cimentícios. A compreensão das propriedades físicas e químicas do clínquer de cimento Portland (PC) é importante para melhorar seu design. O silicato tricálcico (C_3S), ou alita, é a fase principal do clínquer de PC e tem sido amplamente estudado uma vez que é o principal responsável pelo desenvolvimento da resistência da pasta de cimento. Por outro lado, o desenvolvimento de métodos de cálculo na escala molecular possibilitou a modelagem de propriedades estruturais, dinâmicas e energéticas, às vezes difícil de medir por meios experimentais. Esses métodos são relativamente novos no campo da química do cimento, mas tem sido cada vez mais empregados nos últimos 15 anos anos. Neste trabalho, a teoria de funcional da densidade (DFT), a dinâmica molecular clássica (MD) e a dinâmica molecular ab initio (AIMD) são utilizadas para permitir uma melhor compreensão das características mecânicas, térmicas e de superfície do C_3S monoclinico, bem como propriedades da interface C_3S/água.

Esta tese consiste em cinco capítulos: O primeiro capítulo apresenta uma revisão da literatura sobre a química dos cimento e, mais particularmente, sobre o processo de hidratação e sua modelagem. Introduzimos as diferentes fases que compõem o clínquer de cimento Portland, em seguida, a estrutura e os diferentes polimorfos de C_3S são descritos, em particular os polimorfos M_1 e M_3 que são estudados nesta tese. Em seguida, vários modelos de hidratação são discutidos, desde primeiros modelos monoparticular, até as últimas tentativas de investigação em escala atômica.

O segundo capítulo apresenta uma visão geral dos princípios fundamentais relacionados à simulações atomísticas. Descreve os fundamentos dos cálculos com base na densidade eletrônica em sistemas compostos por um grande número de partículas. A teoria funcional

da densidade (DFT) revolucionou o estudo desses sistemas, uma vez que considera a densidade eletrônica como única variável de cálculo, reduzindo muito o tempo computacional. A mecânica molecular clássica é então introduzida, com a noção de campos de forças empíricas que permitem descrever as forças interatômicas. Nós explicamos os métodos de cálculo baseados na minimização de energia e os de dinâmica molecular (MD), onde a equação de movimento de Newton permite simular um sistema a temperatura finita. Princípios de AIMD baseados em cálculos de forças interatômicas por DFT, são explicados, bem como alguns conceitos de mecânica estatística, importantes em MD. Finalmente, diferentes campos de forças, já utilizados para descrever a interface C_3S/água e a hidratação inicial do C_3S são apresentados.

O terceiro capítulo apresenta os resultados dos cálculos de energia de clivagem, e das propriedades mecânicas e térmicas de $C_3S\,M_1$ e M_3 As constantes elásticas são primeiramente calculadas a partir das matrizes de rigidez, usando-se o método de homogeneização de Voigt-Reuss-Hill. Esses cálculos são realizados por um método estático, minimizando a energia da célula unitária a cada incremento de deformação. Além disso, o cálculo do módulo volumétrico é realizado por dinâmica molecular em equilíbrio (EMD) sob diferentes pressões hidrostáticas. As curvas tensão-deformação também são obtidas por dinâmica molecular não-equilibrada, aplicando uma deformação contínua durante a dinâmica do sistema. As constantes elásticas também são deduzidas a partir desses cálculos. O calor específico é determinado a por um método direto, a partir da variação da entalpia em função da temperatura do sistema à pressão constante. Os coeficientes de expansão foram calculados de acordo com a variação do volume em função da temperatura nas mesmas condições. Um método mais preciso, baseado na densidade dos estados fonon (DOS), é empregada. O DOS é calculado a partir da transformação de Fourier da função de autocorrelação das velocidades atômicas. Em geral, as propriedades mecânicos e térmicas calculadas estão de acordo com os resultados experimentais. Finalmente, o cálculo das energias de clivagem do $C_3S\,M_1$ e M_3 é realizada a partir de diferenças energéticas de sistemas unificado e clivado. Os íons de superfície são relaxados para suas configurações de energia mínima aplicando fortes gradientes de temperatura. As energias obtidas permitem construir as formas de equilíbrio dos cristais de M_1 e M_3, usando o método Wulff, com base no crescimento de cristais minimizando a energia livre.

O quarto capítulo apresenta um estudo por MD sobre o comportamento da água de interface em função do grau de hidratação da superfície (040) do $C_3S\,M_3$, com um modelo de

hidratação incluindo a faixa típica de valores de pH das soluções de cimento. A energia da interface é calculada de acordo com o grau de hidratação da superfície. A estrutura e dinâmica das moléculas de água na interface são avaliadas pela análise das trajetórias obtidas. Densidade atômicas na interface, bem como os diferentes modos de ligação das moléculas de água na superfície são realçadas. A orientação das moléculas de água e as esferas de coordenação das diferentes espécies químicas presentes na interface são analisadas. A dinâmica das moléculas de água é quantificada a partir do coeficiente de difusão em função da distância da superfície C_3S. As análises também permitem quantificar o número e o tipo das ligações de hidrogênio na interface, bem como seus tempo de vida. Observa-se que, durante a hidratação, o comportamento da água na interface muda radicalmente. A rede de ligações de hidrogênio existente entre as moléculas de água em contato com o C_3S anidro se destroi com a protonação dos íons óxidos e dos silicatos.

O quinto capítulo apresenta um estudo por AIMD da transferência de prótons na interface C_3S/água, na mesma superfície e no mesmo polimorfo que anteriormente. Três tipos de grupos hidroxilas são analisados: hidróxidos formados em íons óxidos, hidroxilas de grupos silanol e hidróxidos resultantes da dissociação de moléculas de água. Hidróxidos formados nos íons óxidos são muito estáveis. Por outro lado, no caso dos outros dois tipos do grupo hidroxila, seus números flutuam de acordo com as transferências de prótons. Essas transferências foram quantificadas em termos de frequência e de barreira energética. Também discute-se a importância do ambiente dos óxidos na superfície em sua protonação, parâmetro que não foi considerado no modelo utilizado anteriormente, levando em consideração apenas o pKa do hidróxido e do ácido silícico em solução. Além disso, as análises mostram que a orientação das moléculas de água na superfície é muito influenciada pela sua topologia. A análise da densidade de elétrons torna possível destacar regiões de abundância e de deficiência de elétrons devido à adsorção de moléculas de água, bem como durante trocas de prótons. O tamanho dessas regiões no entorno dos grupos hidroxilas é função da estabilidade do grupo. Em geral, os resultados obtidos nesta tese nos permitem entender melhor o comportamento do C_3S na escala atômica e da sua hidratação precoce, produzindo-se antes mesmo de misturar com a água de amassadura.

Keywords: Silicato tricálcico. Hidratação. Dinâmica molecular. Energia de clivagem. Interface.

Contents

General introduction **1**

1 Review of Portland cement chemistry and hydration **5**

1.1 Clinker formation and composition 5

1.2 Tricalcium silicate polymorphism and structure 8

1.3 Tricalcium silicate hydration 11

2 Atomistic simulation fundamentals **17**

2.1 Electronic structure methods 17

2.2 The Density Functional Theory 19

2.3 Molecular Mechanics 20

2.3.1 Short-Range Interactions 21

2.3.2 Long-Range Interaction 21

2.4 Energy Minimisation Methods 22

2.5 Molecular Dynamics 24

2.6 *ab initio* Molecular Dynamics 25

2.7 Statistical Mechanics 26

2.8 Thermostat Algorithms . . . 28
2.9 Force Fields . . . 30
2.9.1 INTERFACE FF . . . 30
2.9.2 ClayFF Force Field . . . 32
2.9.3 ReaxFF Force Field . . . 33

3 Mechanical, thermal, and surface properties of tricalcium silicate 37

3.1 Elastic properties . . . 38
3.1.1 Methods . . . 41
3.1.2 Results . . . 44
3.2 Thermal properties . . . 51
3.3 Methods . . . 53
3.4 Results . . . 54
3.5 Cleavage energies and equilibrium shapes . . . 58
3.5.1 Methods . . . 60
3.5.2 Energy calculation . . . 61
3.6 Conclusion . . . 64

4 MD simulation of C_3S/water interface: influence of the protonation state on water's behavior 67

4.1 Methods . . . 68
4.2 Results and discussion . . . 70
4.2.1 Energy calculation . . . 70

4.2.2 Structural properties 71

4.2.3 Dynamical properties 76

4.3 Conclusion 81

5 AIMD simulation of C_3S/water interface: protonation state and proton transfer analysis 83

5.1 Computational Methods 84

5.2 Results 88

5.2.1 Water structure 88

5.2.2 Proton transfer analysis 92

5.3 Conclusion 95

General conclusion and perspectives 97

List of Figures

1 Global process emissions from cement production, with a 95 % confidence interval [1]. 1

1.1 BSE image of a dry clinker grain realized during this thesis (left). Phases in light grey are C_4AF, grains in dark grey are C_3A and grains in medium grey are calcium silicate phases. EDXS analysis associated to the pointer (right). . . 7

1.2 Photomicrography of alite (blue-grey), belite (brown-tan) grain, and interstitial aluminoferrite phase, magnified 1000 times [19]. 8

1.3 Relation between the formation of M_1 and M_3 polymorph with the relative amounts of MgO and SO_3 [28]. 9

1.4 Typical evolution of the heat flow and degree of hydration of alite at water/alite = 0.5 [8] 11

2.1 A general AIMD algorithm. 25

3.1 Unit cells of M_1 C_3S (cell parameters: a = 27.874 Å, b = 7.059 Å, c = 12.257 Å, β = 116.03°) [36] and M_3 C_3S (cell parameters: a = 12.235 Å, b = 7.073 Å, c = 9.298 Å, β = 116.31°) [34]. Color code: calcium cations in green, oxygen anions and silicate oxygen in red, silicon atoms in yellow, and silicate polyhedra in blue. 38

3.2 Distribution of elastic moduli in space for the M_1 C_3S, computed with IFF. . . . 47

3.3 Distribution of elastic moduli in space for the M_3 C_3S, computed with IFF. . . . 48

3.4 Strain and volume variation as function of the hydrostatic pressure. 48

3.5 Radial distribution function of Ca-Os pairs as a function of the hydrostatic pressure. 49

3.6 Stress-strain curves of NEMD simulations and static MM calculation with IFF. 50

3.7 Phonon density of states with VACF in insets (top), and partial density of states (bottom) of M_1 and M_3 C_3S obtained with IFF. 56

3.8 Phonon density of states with VACF in insets (top), and partial density of states (bottom) of M_1 and M_3 C_3S obtained with ClayFF. 56

3.9 Specific heat of M_1 and M_3 C_3S obtained by the direct and VACF method, plotted as function of the temperature. The transparent areas represent the error. Previously computed value from VACF calculation, as well as fitting of experimental measurements [126] and direct measurements [127] are plotted in addition to the results. 58

3.10 Workflow of the cleavage simulations. 61

3.11 Equilibrium shapes of M_1 and M_3 C_3S 63

3.12 Equilibrium form of C_3S, adapted from Maki and Chromý [21, 25]. 63

3.13 Zonal structure with M_3 overgrowing M_1. Reflected light image adapted from Maki [21] 64

4.1 Workflow of the interface simulations. 69

4.2 Atomic density profiles of the interface for a) Dry C_3S (pH $\gg$15), b) 1st hyd. (pH >15), c) 2nd hyd. (pH ~15), d) 3rd hyd. (pH ~13.5), e) 4th hyd. (pH ~11.5). The interface (z = 0) is defined as the average position of the uppermost layer of silicon atoms. Code for atom nomination: Os for silicate oxygen, Oi for oxygen anion, Oh and Hh for hydroxyl oxygen and hydrogen, Osi and Hsi for silanol oxygen and hydrogen, Ow and Hw for water oxygen and hydrogen. . . 72

4.3 Atomic density maps for dry C_3S / water interface of water molecules of the first layer (0.5 Å < z < 2.4 Å) (left). Zoom on the three hydrogen bonding types: a) two Hw–Oi, b) two Hw–Os bonds, c) one Hw–Oi and one Hw–Os bond (right). Color map: Ca in green, Oi in red, Si in yellow, Os in violet, Ow in red dotted line, Hw in blue dotted line. 73

4.4 OPD of water molecules within 2.5 Å from the surface with variation of the degree of hydration. 74

4.5 Radial distribution function of a) Oi-Hw and Oh-Hw, b) Os-Hw and Osi-Hw, c) Ca-Ow, d) Ow-Ow, for different degrees of hydration. 75

4.6 Evolution of the diffusion coefficient of water molecules with distance from the C_3S surface with variation of the degree of hydration. The interface ($z = 0$) is defined as the average position of the uppermost layer of silica atoms. 77

4.7 Evolution of the number of hydrogen bonds per water molecules along the z axis with variation of the degree of hydration: a) Dry C_3S(pH ≫15), b) 1st hyd. (pH >15), c) 2nd hyd. (pH ~15), d) 3rd hyd. (pH ~13.5), e) 4th hyd. (pH ~11.5). The interface ($z = 0$) is defined as the average position of the uppermost layer of silica atoms. 79

5.1 Structure of the investigated C_3S(040)/water interface. 85

5.2 General analysis scheme using Python and the MDAnalysis library 87

5.3 Atomic structure of the (040) surface. Color code: calcium cations in green, oxygen anions and silicate oxygen in red, silicon atoms in yellow and hydrogen in hydroxide H-Oi in white. The snapshot shows the position of the water molecule before protonation of the oxide. The ions of the surface are in the same layer, except for the calcium indicated by blue circles, having perpendicular coordinate z ~2 Å larger. 88

5.4 Number of hydroxyl groups formed at the surface on oxide ions (Oi-H), oxygen in silicates (Os-H), and from water dissociation (Odw-H) for (a) AIMD simulation, (b) ReaxFF simulation. 89

5.5 Atomic density profile of water molecules along the z axis for AIMD. The origin adopted is the average coordinate of the uppermost oxygen silicate layer. The layering observed results from the hydrogen bond network created between the strong interaction between the water molecules and the ionic surface. 90

5.6 Radial distribution function H-Oi, H-Os, and Ow-Ca pairs for AIMD and ReaxFF simulations. 90

5.7 (a) Probability distribution of the angle θ between the water dipole moment and the z axis, perpendicular to the surface. Lighter regions correspond to higher probabilities (b) Density mapping of θ for water molecules within 3 Å from the surface. Color code: Ca in green, Os and Oi in red, Si in yellow, H in hydroxide H-Oi in white. 91

5.8 Normalized probability distribution of the H-Os (blue) and H-Odw groups (red). 92

5.9 Frequency of PT as a function of its lifetime τ (left). Evolution of the total number of hops within the simulation time (right). 92

5.10 Free energy contour plot of PT between Ow and Os as a function of the distance $d_{\text{Oa-Ob}}$ between oxygen atoms, and of $\delta_{\text{a-b}} = d_{\text{Oa-H}} - d_{\text{Ob-H}}$. The red circles shows the local free energy minima, corresponding to the most stable configurations before and after the proton jump. The red square is the saddle point, where the proton is equidistant from both oxygen atoms. 93

5.11 Snapshots of the isosurface of electron density difference. Orange and cyan isosurface represent positive and negative $\Delta\rho$, respectively. a) A water molecule between a silicate and a silanol group. b1) Electron density delocalization during a proton exchange between a molecular water and a hydroxide. b2) Electron abundance and depletion regions around an hydroxide created upon water dissociation. 94

List of Tables

1.1 Quantitative EDXS analysis at the region pointed in Figure 1.1. 7

1.2 Unit cells found in literature for rhombohedral, monoclinic and triclinic C_3S (not exhaustive). Color code: calcium cations in green, oxygen anions and silicate oxygen in red, silicon atoms in yellow, and silicate polyhedra in blue. Sites not fully filled in color represent partial occupancies. 10

2.1 INTERFACE FF parameters for dry and hydrated C_3S [71]. Hh and Oh are hydrogen and oxygen in hydroxides. Hs and Os are hydrogen and oxygen in silicates. Hsi and Osi are hydrogen and oxygen in silanol groups. 31

2.2 ClayFF parameters for dry C_3S [73] 33

3.1 Stiffness constants homogenized elastic constants of M_1 C_3S in GPa. 45

3.2 Stiffness constants and homogenized elastic constants of M_3 C_3S in GPa. [a]Calculated on the same M_3 model by Mumme [34]. [b]Calculated on the M_3 model proposed by de la Torre [35]. 46

3.3 Elastic moduli and Poisson's ratio obtained from NEMD simulations with IFF. [a]Results from previous stress controlled NEMD. 51

3.4 Lattice parameters of M_1 and M_3 C_3S, from EMD and DFT calculations. 55

3.5 Lattice parameters of M_1 and M_3 C_3S, from EMD and DFT calculations. 57

3.6 Cleavage energies of M_1 and M_3 C_3S. Only the lowest energy plane is given in the (100) direction for M_1. 62

4.1 Interfacial energy for different degree of hydration 71

4.2 Lifetime of hydrogen bonds with variation of the degree of hydration. 80

General introduction

Concrete is fairly the most used material on Earth and constitutes most of the infrastructure of our society. The universal and systematic use of concrete in the construction industry induces serious drawbacks in the environment. The CO_2 emissions from cement production has increased drastically since the end of World War II, and at a higher rate since 2000, despite a slight decline in 2016 (see Figure 1) [1].

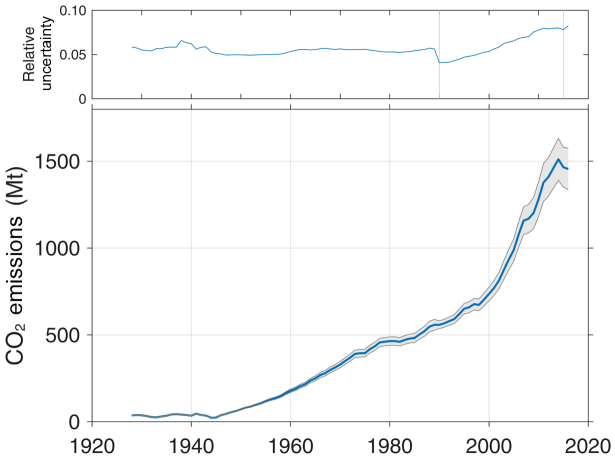

Figure 1. Global process emissions from cement production, with a 95 % confidence interval [1].

These emissions have two sources: the first comes from the decarbonation reaction of the calcium carbonate contained in limestone. These "process" emissions contributes to about 5 % of the total emissions [2]. A second source is the combustion of fossil fuels, which represents 60 % of the "process" emissions, according to the International Energy Agency [3], giving a total contribution of cement production to global CO_2 emissions of about 8 % [1]. Advances in cement and concrete science are traditionally made by a laboratory, macroscale approach, carrying studies on mechanical, rheological or chemical properties. At the macroscale, the environmental impact is commonly lowered by the optimization of mixtures with the lowest cement content possible. Several strategies are used, from plasticizer addition to lower the

water/cement ratio, to the use of supplementary cementitious materials from the industry and agriculture, or the optimization of concrete packing density [4, 5]. Although low clinker ratio cements are increasingly employed, the development of new clinker types is one of the main strategy to reduce greenhouse gas emissions. In a context of durable design, considerable efforts are being made for a better understanding of Portland cement (PC) hydration [4, 6–12]. Considering the hydration of all the clinker phases together would turn the study highly complex. Most of the time, the tricalcium silicate (C_3S) received a particular attention, due to its predominance in original Portland cement clinker (about 50% to 70% by mass). C_3S is the main responsible for calcium silicate hydrates (C – S – H) setting and strength development. As a reasonably recent field, atomistic simulations represent a powerful tool in material sciences in attempt to understand properties observed at the macroscale. These methods are inexpensive and allow to capture mechanisms invisible to our eyes, and in non-reproducible conditions in laboratory. They have been increasingly used to design new materials or to predict their behavior.

Macroscale to microscale modeling provides descriptions generally based on few parameters, most of the time empirical and relying on a proper calibration. In order to develop satisfying and reliable models, some thermodynamical, mechanical or chemical data are needed. With the development of computational sciences and technology, simulations at the molecular scale, and from *first principles* are now widely employed. This means that a down to upscale modelling is possible starting from quantum mechanics. In addition to the improvement of the fundamental understanding of matter and of the mechanisms occurring during a physical or a chemical process, the results of atomistic simulations can serve as a database for models at larger scales. Moreover, from an atomistic point of view, several processes such as clinker grinding [13], clinker hydration and dissolution [14], C – S – H precipitation and setting [15] can be studied individually. As a matter of fact, processes that change the surface topography of minerals such as adsorption, desorption, dissolution, and growth reaction are difficult to observe directly at the atomic scale with analytical methods such as atomic force microscopy (AFM), scanning force microscopy (SFM) or vertical scanning interferometry (VSI) [10]. Atomistic simulation methods make it possible to go beyond the current limits of technology and scale, but also to analyze the behavior of systems under conditions that cannot be produced experimentally.

Objectives

The main objectives of this thesis are:

- The characterization of the mechanical and thermal properties, as well as the cleavage energies of the M_1 and M_3 C_3S by means of atomistic simulations. The computational methods used are compared and discussed. Also, the equilibrium shapes of both polymorph are determined.
- The investigation of the behavior of superficial water with the increase of the hydration degree of the first atomic layer. An existing atomistic hydration model for C_3S will be used. The structural and dynamical properties of water will be emphasized.
- The study the proton transfer occurring at the C_3S/water interface by means of *ab initio* MD. The frequency and energy of these transfers will be quantified. Moreover, the structure of water, and the protonation state of the surface will be studied and compared with the previously used hydration model.

Chapter 1

Review of Portland cement chemistry and hydration

1.1 Clinker formation and composition

The Portland cement (PC) is widely used in the construction industry and is mainly made of clinker, as a result of the heating process of a grinded clay and limestone mixture up to 1450 °C. The clinker formation process can be conveniently divided into three phases:

1. Below 1300 °C, oxides are formed, on one hand, by the decomposition of calcium carbonate $CaCO_3$ contained in limestone, into calcium oxyde CaO (decarbonation reaction). On the other hand, clay minerals are decomposed in silica SiO_2, aluminate Al_2O_3 and ferrite Fe_2O_3. Among other compounds, belite Ca_2SiO_4, tricalcium aluminate $Ca_3Al_2O_6$ and tetracalcium aluminoferrite $Ca_4Al_2Fe_2O_{10}$ are formed, respectively, following these reactions:

$$\begin{aligned} 2\,CaO + SiO_2 &\longrightarrow Ca_2SiO_4 \\ 3\,CaO + Al_2O_3 &\longrightarrow Ca_3Al_2O_6 \\ 4\,CaO + Al_2O_3 + Fe_2O_3 &\longrightarrow Ca_4Al_2Fe_2O_{10} \end{aligned} \tag{1.1}$$

2. Between 1300 and 1450 °C, in the presence of a melt mainly formed by aluminate and ferrite, belite reacts with free CaO to form alite:

$$Ca_2SiO_4 + CaO \longrightarrow Ca_3SiO_5 \tag{1.2}$$

3. During the cooling, the aluminate and ferrite phases from the melt crystallize, and the alite and belite experience polymorphic transitions. Afterwards, the clinker is grinded and mixed with gypsum to prevent flash settings of aluminate.

The main phases present in PC clinker are thus: alite (50 to 70 %), belite (15 to 30 %), tricalcium aluminate C_3A[1](5 to 10 %) and tetracalcium aluminoferrite C_4AF (5 to 15 %) [16]. Alite is the principal component of Portland cement and is the impure form of tricalcium silicate C_3S. It reacts relatively quickly with water and is the principal phase responsible for strength development, in particular during the early ages of hydration. Belite is the chemically modified form of dicalcium silicate (C_2S). Its hydration rate is slower than that of C_3S, and it contributes much less to the strength development during the first 28 days, but in a greater extent at later ages. The higher reactivity of alite compared to belite is due to the reactive sites around its oxide ions [17, 18]. C_3A reacts rapidly with water and can cause an undesirable fast setting, inhibiting the hydration of the other phases unless gypsum is added to control its setting. The aluminoferrite phase can vary in composition and hydration rate depending on the Al/Fe ratio [16].

The Figure 1.1 presents a backscattered electron image (BSE) of well polished section of Portland cement and resin mixture. A clinker grain composed of the different phases corresponding to different grey level is shown at the center of the image. The brightness of the phases in the BSE image is related to the atomic number of the elements with which the incident electrons interact. According to the EDS point analysis and particularly the atomic proportions, the selected point corresponds to alite and likely M_3 polymorph, which seems to suggest the proportions of magnesium and sulfur (see Table 1.1). It is often difficult to predict the phase of a grain in SEM images, without quantitative analysis nor coloring techniques. C_2S grains are known to have rounder shape whereas C_3S grains are often more angular (see Figure 1.2). Nonetheless, some C_3S grain are rounder and can be confounded with C_2S.

[1]The cement chemistry notation is used to shorten the chemical formulas, therefore: C = CaO; S = SiO_2; A = Al_2O_3; F = Fe_2O_3; H = H_2O. e.g., C_3S = Ca_3SiO_5 and C – S – H = $(CaO)_x - (SiO_2) - (H_2O)_y$.

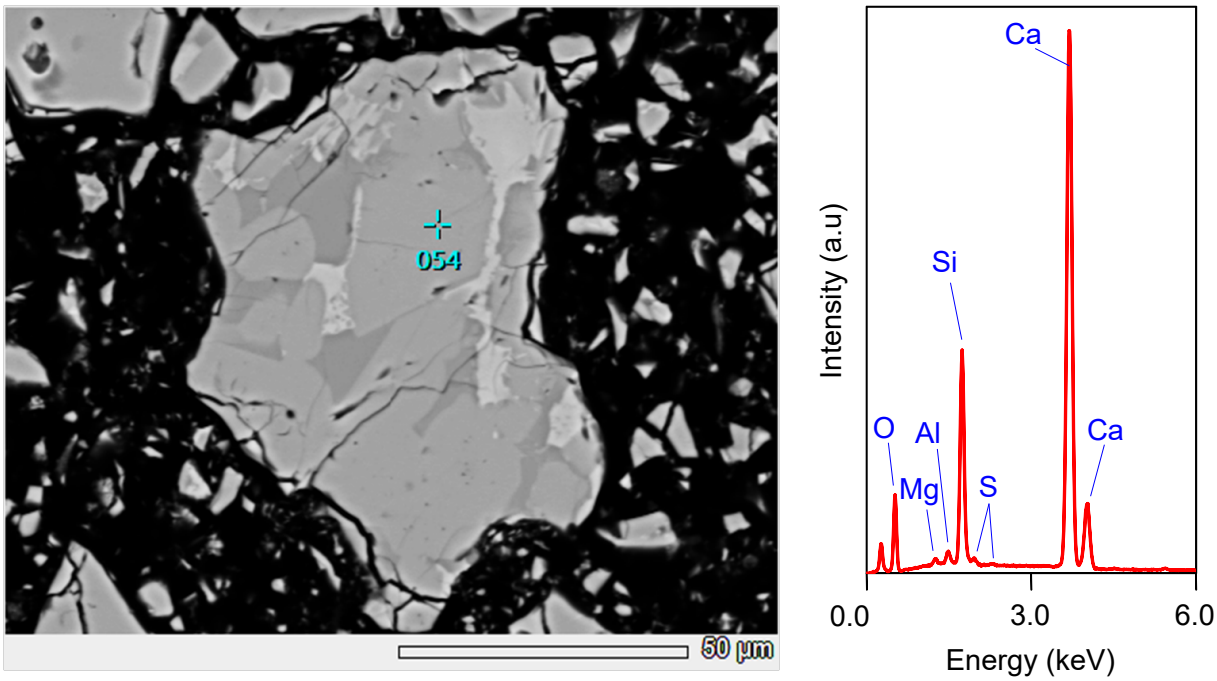

Figure 1.1. BSE image of a dry clinker grain realized during this thesis (left). Phases in light grey are C_4AF, grains in dark grey are C_3A and grains in medium grey are calcium silicate phases. EDXS analysis associated to the pointer (right).

Element	Energy (keV)	Mass (%)	Atom (%)
Al	1.486	0.60	0.54
Ca	3.690	48.29	29.46
Mg	1.253	0.41	0.41
O	0.525	38.71	59.16
S	2.307	0.08	0.06
Si	1.739	11.91	10.37

Table 1.1. Quantitative EDXS analysis at the region pointed in Figure 1.1.

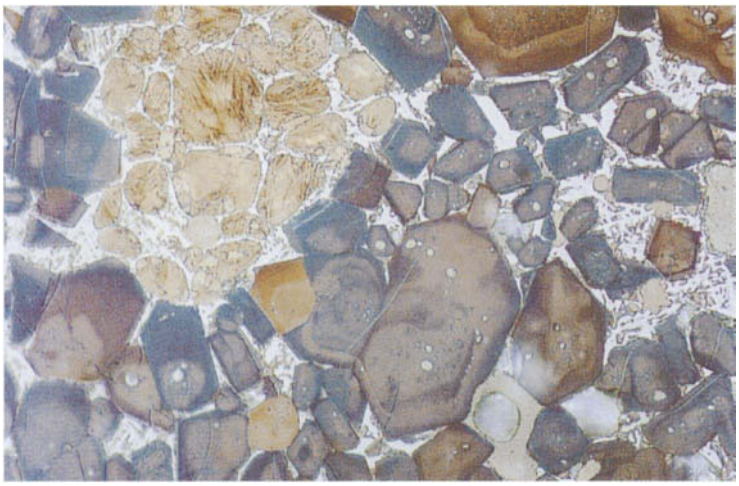

Figure 1.2. Photomicrography of alite (blue-grey), belite (brown-tan) grain, and interstitial aluminoferrite phase, magnified 1000 times [19].

1.2 Tricalcium silicate polymorphism and structure

When heated and analysed by Differential Thermal Analysis (DTA) coupled with high-temperature X-ray diffraction (HT-XRD) and high-temperature optical microscopy (HTOM), C_3S can transform into seven different phases, from three different crystal systems: triclinic (T), monoclinic (M) and rhombohedral (R) [20–26]:

Pure C_3S: $T_1 \xleftrightarrow{620\,^\circ C} T_2 \xleftrightarrow{920\,^\circ C} T_3 \xleftrightarrow{980\,^\circ C} M_1 \xleftrightarrow{990\,^\circ C} M_2 \xleftrightarrow{1060\,^\circ C} R$

Impure C_3S (Mg or Zn doped): $M_1 \xleftrightarrow{990\,^\circ C} M_2 \xleftrightarrow{1060\,^\circ C} M_3 \xleftrightarrow{1070\,^\circ C} R$

The room temperature structure of alite is thus influenced by the content and the nature of impurities present in the melt [27]. Whereas the pure compound stabilizes as T_1 at room temperature, in normal production clinker, the C_3S crystallizes into M_1 and M_3 because of impurities. The M_3 form does not exist in pure C_3S and its stabilization is favored by an increase in foreign ions [28]. C_3S is made of silicate tetrahedra SiO_4^{4-}, calcium cations Ca^{2+} and oxide anions O^{2-} and vary particularly with regards to the orientations and organization of the SiO_4^{4-}. These structural changes affect the coordination of the Ca^{2+} ions and the oxygen atoms of the SiO_4^{4-}, and thus the reactivity with water. High magnesium oxide MgO contents favour the stabilization of M_3 over M_1, which stabilize at high sulfate SO_3 contents [16, 28] (see Figure 1.3).

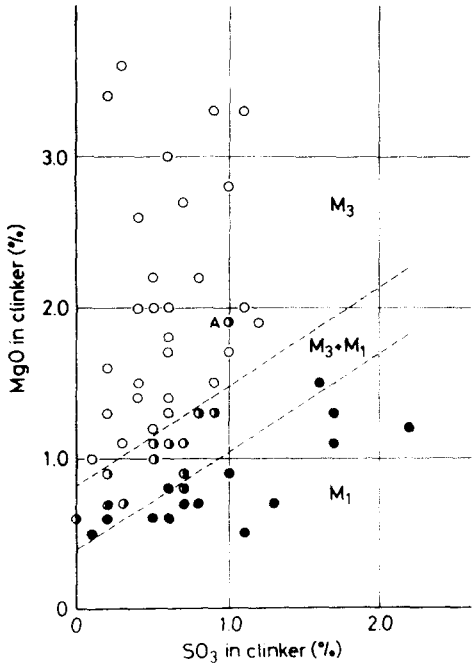

Figure 1.3. Relation between the formation of M_1 and M_3 polymorph with the relative amounts of MgO and SO_3 [28].

The cooling and quenching conditions also affect significantly the structure alite at ambient temperature [27]. At low MgO content, high cooling rates influence the formation of M_3 over M_1 [27, 28]. The limit of substitution of MgO was found to be 2 wt% at 1550 °C, and 1.5 wt% at 1420 °C [16]. Furthermore, experiments suggests that a higher content of M_1 leads to an increase in compressive strength [29]. The Table 1.2 summarizes the structure found in the literature.

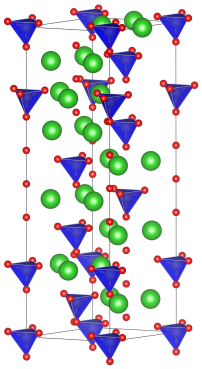

R ($R3m$)
$a = 7$ Å, $c = 25$ Å
Jeffery, 1952 [30]

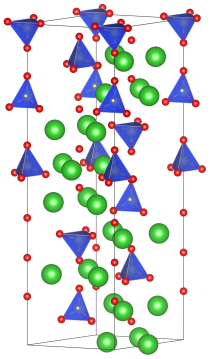

R ($R3m$)
$a = 7.057$ Å, $c = 24.974$ Å
Il'inets et al., 1985 [31]

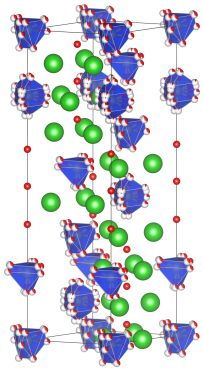

R ($R3m$)
$a = 7.135$ Å, $c = 25.586$ Å
Nishi and Takéuchi, 1984 [32]

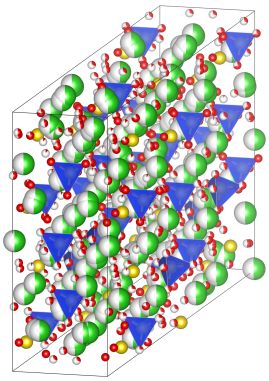

M_3 (Cm)
$a = 33.083$ Å, $b = 7.027$ Å,
$c = 18.499$ Å, $\beta = 94.12°$
Nishi et al., 1985 [33]

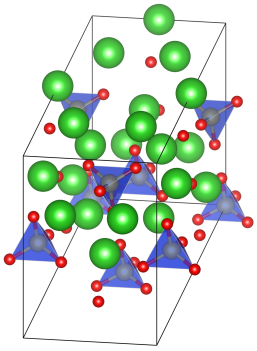

M_3 (Cm)
$a = 12.235$ Å, $b = 7.073$ Å,
$c = 9.298$ Å, $\beta = 116.31°$
Mumme, 1995 [34]

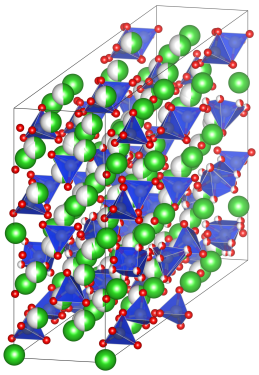

M_3 (Cm)
$a = 33.1078$ Å, $b = 7.0355$ Å,
$c = 18.5211$ Å, $\beta = 94.137°$
de la Torre et al., 2002 [35]

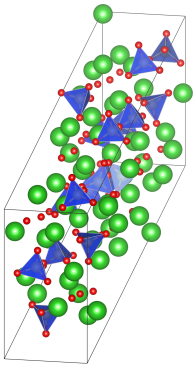

M_1 (Pc)
$a = 27.874\,38$ Å, $b = 7.0591$ Å,
$c = 12.2578$ Å, $\beta = 116.03°$
de Noirfontaine et al., 2012 [36]

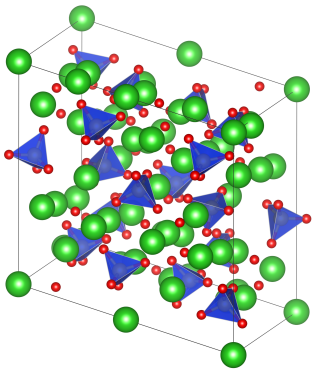

T_1 ($P\bar{1}$)
$a = 11.6389$ Å, $b = 14.1716$ Å,
$c = 13.6434$ Å, $\alpha = 104.982°$,
$\beta = 94.622°$, $\gamma = 90.107°$
de la Torre et al., 2008 [37]

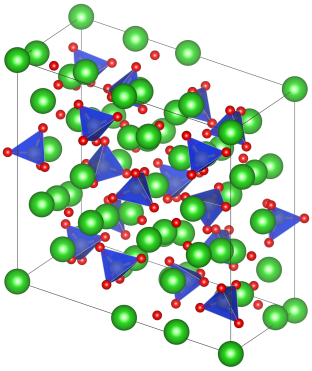

T_1 ($P\bar{1}$)
$a = 11.67$ Å, $b = 14.24$ Å,
$c = 13.72$ Å, $\alpha = 105.3°$, $\beta = 94.2°$
Golovastikov et al., 1975 [38]

Table 1.2. Unit cells found in literature for rhombohedral, monoclinic and triclinic C_3S (not exhaustive). Color code: calcium cations in green, oxygen anions and silicate oxygen in red, silicon atoms in yellow, and silicate polyhedra in blue. Sites not fully filled in color represent partial occupancies.

1.3 Tricalcium silicate hydration

The cement paste resulting of the hydration of PC is mostly composed of two components: amorphous calcium silicate hydrate (C – S – H) and crystalline calcium hydroxide $Ca(OH)_2$ (CH), also called portlandite. Ettringite and monosulfate are also present in cement paste but with relatively low content. As a consequence of the relative abundance and structure of C – S – H and CH, the contribution of the CH to the mechanical performance of cement paste can be depreciated compared to C – S – H. Although the majority of PC is blended with supplementary cementitious materials, the early age strength is mainly due to the hydration process of clinker phases. Because of its predominance in clinker constitution, alite controls the hydration kinetics of PC and is the most studied phase of the clinker. The hydration process can be divided into the C_3S dissolution reaction, and the C – S – H and CH precipitation reactions:

$$\begin{aligned} Ca_3SiO_5 + 5\,H_2O &\longrightarrow 3\,Ca^{2+} + 6\,OH^- + H_4SiO \\ x\,Ca^{2+} + 2xOH^- + H_4SiO_4 &\longrightarrow (CaO)_x{-}(SiO_2){-}(H_2O)_b + (2{+}x{-}b)H_2O \\ y\,Ca_2{}^{+} + 2yOH^- &\longrightarrow Ca(OH)_2 \end{aligned} \tag{1.3}$$

with $x + y = 3$. The silicate specie H_4SiO_4 is used for convenience, but $H_3SiO_4{}^-$ and $H_2SiO_4{}^{2-}$ are also presents, with respective concentration depending on the pH of the solution [8]. Isothermal calorimetry is one of the principal experimental method to study alite hydration (see Figure 1.4).

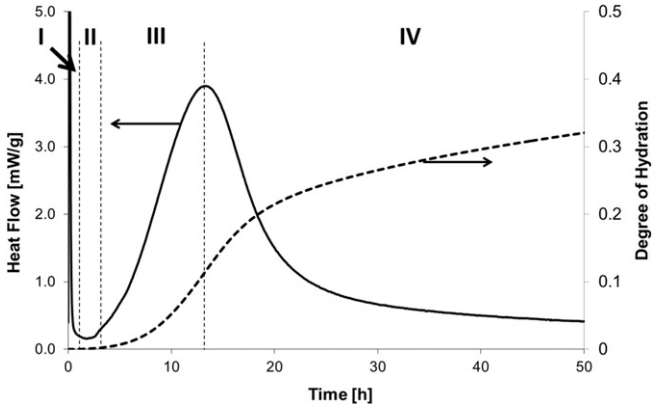

Figure 1.4. Typical evolution of the heat flow and degree of hydration of alite at water/alite = 0.5 [8]

The heat evolution curve obtained reveals four periods: the initial period, the induction period, the acceleration period and the deceleration period. The initial period is characterized by a fast exothermic reaction. The heat released during this period comes from the wetting

and dissolution of alite. The cause of the induction, or "dormant" period is still under debate. As a first explanation, the hypothesis of a metastable barrier of C – S – H forming on the dry, unreacted C_3S has been argued. However, a "geochemical theory", which associates the rate of dissolution to the saturation level of the solution, could explain experimental observations such as etch-pits at the surface of cement grains, making the formation of a barrier unlikely [4, 7, 9]. This hypothesis is based on the fact that, as they have chemical elements in common, C_3S dissolution and C – S – H/CH precipitation are driven by the deviation from equilibrium [39]:

$$\underset{\longleftarrow\ undersaturation}{\mu_i^{C_3S}} > \mu_i^{solution} > \underset{supersaturation\ \longrightarrow}{\mu_i^{C-S-H/CH}} \tag{1.4}$$

where μ_i is the chemical potential of a specie i common to C_3S and C – S – H/CH. The diffusion can be a limiting factor when a specie diffuses slower than it dissociates, accumulating close to the surface and decreasing the undersaturation locally. The surface energy, which is determined by the orientation of the crystal face, can be seen as an indicator of the surface stability: a larger surface energy traduces the presence of uncoordinated atoms. The low coordination between atoms at the surface can lead to stronger interaction with water, and possibly to an higher reactivity [14]. However, this relation was not verified by atomistic simulation methods and in fact, the initial hydroxylation of superficial silicates and oxides, as well as the dissociation of calcium modify the surface property, preventing from any correlation with the surface plane [14]. Another interesting fact is that the evolution of the dissolution surface area of C_3S, which should be monotonic because of isotropic conditions, has shown to be increased by the extension of etch-pits [8, 39]. Etch-pits are created by enlargement of crystal defects such as screw, and edge. Defects in the mineral structure generally arise from the amount of impurities and quenching conditions [11, 39]. The effect of etch-pits and growth terraces has already been studied by atomistic simulation on calcite, indicating that the water exchange frequencies for surface calcium ions vary by up to one order of magnitude depending on surface structure, and thus, that the surface reactivity is controlled by the topology [40, 41].

Many models have been developed during decades in order to describe the hydration kinetic of cement. Most of them focused on the C_3S because of its predominant role in the overall reaction. The first models were single-particle models, with an assumption of a spherical particle with radial growth of hydration product. The first models assumed a metastable

C – S – H layer, hindering the dissolution of the dry core, and separating the outer product area and the inner product area. Some experiments indicate that the formation of C – S – H is the rate-controlling process of the early hydration. The precipitation reaction (see Equation (1.3)) occurs in two steps: a small ionic cluster is formed on an energetically favourable site. A nucleus is considered stable when it overpass a critical size at which the thermal fluctuations cannot interrupt its growing process. After that, the nucleus start growing at a rate depending on the thermodynamic driving force and the unoccupied volume. In the Johnson-Mehl-Avrami-Kolmogorov (JMAK) nucleation model, nuclei of infinitely small size form at random positions in the considered volume at the start of the transformation, the growth is spherical with a linear rate G and the volume fraction of transformed material increases exponentially with time [10, 42]:

$$X(t) = 1 - \exp(-X^e(t)) \tag{1.5}$$

where X^e is the sum of the volume fraction of every sphere ignoring interference between them, also called "extended" volume fraction. Under the site saturation assumption N_V^0 nuclei are present at the start of the transformation and no nucleus forms during it:

$$X^e(t) = \frac{4\pi G^3 N_V^0}{3} t^3 \tag{1.6}$$

where G is the linear growing rate. If we consider that the nucleation occurs during the growth of nuclei, with a rate I_V:

$$X^e(t) = \frac{4\pi}{3} \int_\tau^t I_V G^3 (t-\tau)^3 \mathrm{d}\tau \tag{1.7}$$

However, the strong assumption regarding the random distribution of the nucleation sites must be achieve for the Equation (1.5) to be respected, and for C_3S, it has been well established that the growth of the hydration product occurs preferentially on the surface of the dry particles. The Boundary Nucleation and Growth (BNG) is a nucleation model that describes the growing of hemispheres of hydrated product on dry planar surfaces, at a constant rate G, as in the JMAK model. The impingement can occurs between two hemispheres growing on the same surface, or between two hemispheres growing on two different surfaces [42]. The BNG model reproduces an initial acceleration of the heat released in good agreement with experimental results. However, it predicts an increase of the heat peak and of deceleration period with the water/cement ratio (w/c). The assumption that the growth rate of C – S – HH is linearly dependent on the supersaturation of the cement solution w.r.t C – S – H precipitation can overcome this issue [42]. The model was calibrated for different minerals and the

ΔG_{crit} obtained were in good agreement with experimental results. However, the BNG model is limited by the fact that it rely on four parameters: the growth rate, the number of nuclei per unit surface area, the molar volume of the gel, and the opacity of the gel with regards to ion diffusion. These parameters are really difficult to obtain experimentally but can be accessed by simulations of nanoparticles, using a more fundamental level of theory. kinetic Monte Carlo (kMC) modelling of C_3S dissolution and C – S – H precipitation provide more physically meaningful results, and an insight on mechanisms occurring at the nanoscale. The most common methods are based on transition state theory, considering the removal or addition of an atom, a molecule, a coarse-grain or a block with specific rates dissolution and precipitation rate k^- and k^+, respectively [43, 44]:

$$k^- = f \exp -\frac{nE^-}{kT} \tag{1.8}$$

$$k^+ = f \exp -\frac{nE^+ - \Delta G^*}{kT} \tag{1.9}$$

where k is the Boltzmann constant, T is the temperature, $nE^\pm$ is the activation energy for the dissociation to occur, n is the number of nearest neighbors and f is the fundamental frequency. The Equation (1.8) is directly derived from the Arrhenius law, while the G^* term in Equation (1.3) is the free energy accounting for the concentration of the solute [44]. The crystal surface topology is often represented as a cubic lattice through a Kossel's surface model, considering lattice positions, such as terraces, kinks, vacancies or adatoms. These types of position determine the number of nearest neighbors of a lattice site. The net dissolution is:

$$k = k^- - k^+ = A\left(1 - \exp\left(\frac{\Delta G^*}{kT}\right)\right) \tag{1.10}$$

As a last advance in modelling C_3S dissolution by kMC, Martin et al. proposed a model including the precipitation term ΔG^* [44]. The authors observed three dissolution mechanisms, influencing the dissolution free energy ΔG:

- dissolution of the initial irregularities of the surface, closed to the initial equilibrium
- pit opening and step retreat at critical free energy ΔG_{crit}
- vacancy opening far from the equilibrium condition

A recently proposed off-lattice kinetic Monte Carlo (kMC) model considering nanoparticles allowed to predict precipitation mechanisms and kinetics in agreement with the BNG prediction. kMC simulations provides a more fundamental approach to calibrate the BNG model,

making him more consistent regarding to chemical and physical mechanisms occurring at the nanoscale [15, 42]. The time scale that kMC can cover is typically larger than the simulation time of MD which cannot overcome few nanoseconds. However, differently from classical Monte Carlo (MC) methods, it requires information on the rates of all possible event occurring which are typically infinite [15]. In this context, atomistic simulation methods can provide important information.

In recent years, many scientific contributions of atomistic simulations of C – S – H [45–53], tobermorite [54, 55], portlandite (CH) [56–60] and clinker constituents [14, 61–69] were carried out, giving rise to a force field review and a database of parameters to describe the interactions between atoms in cementitious materials [70]. Although many studies are focused on the main hydration product (C – S – H), first insights on the early hydration of C_3S were provided with reactive [14], and classical MD [71]. Two classical force fields; namely INTERFACE FF (IFF) [72], and ClayFF [73], and the reactive force field ReaxFF [74] were already used to simulate the interface between C_3S and water at the atomic scale. A recent work, employing ClayFF, allowed to assess structural and dynamical properties of water and ions, as well as dissolution of C_3S in sodium sulfate solution [75]. However, at the molecular scale, a quantitative approach of the dissolution of C_3S in water should be performed with precautions. A classical MD investigation cannot describes accurately dissociation mechanisms which are mainly related to reactive events. This is because classical does not consider charge transfer between species and depending of its environment, the charge of an ion do vary. Atomistic simulations methods are powerful tools which can provides valuable information, but has any other modelling tool, their limitation must be known to provide meaningful results.

Chapter 2

Atomistic simulation fundamentals

Atomistic simulation methods can be divided in two large categories: quantum mechanical simulations (QM) and molecular mechanical simulations (MM). The former, also called *ab initio* methods, consider the electronic contribution to solve the Schrödinger equation by the way of approximations, resulting in accurate, but computationally costly calculations. The later neglect the electronic motion, the atoms are defined as classical particle, and the energy of the system is calculated as a function of their positions, using Newton classical mechanics, thus reducing drastically the computation time [10]. The most commonly used MM methods are Monte Carlo (MC) and molecular dynamics (MD), though their algorithms can be employed for simulation at larger scale. The difference between these two method is that MC is a stochastic method while MD is purely deterministic. In this thesis, density functional theory (DFT), derived from electronic structure methods, classical MD and *ab initio* MD were combined to characterize mechanical, thermal, superficial, and interfacial properties of C_3S at the molecular scale.

2.1 Electronic structure methods

Electronic structure methods consist in the resolution of the time-independent Schrödinger equation [76]:

$$\hat{\mathcal{H}}\Psi_i(\mathbf{r}) = E_i\Psi_i(\mathbf{r}) \tag{2.1}$$

$\hat{\mathcal{H}}$ is the general form of the Hamiltonian operator, $\Psi_i(\mathbf{r})$ is the eigenfunction of the system, at state i, that is function of the position vector $\mathbf{r}$. E_i is the energy of the system at state i, or eigenvalue associated to the eigenfunction $\Psi_i(\mathbf{r})$. The Hamiltonian operator is called the energy functional, since it assigns a scalar (an energy E_i) to a function ($\Psi_i(\mathbf{r})$). For a molecular system containing M nuclei and N electrons, it can be expressed in atomic units as follow [77]:

$$\hat{\mathcal{H}} = -\frac{1}{2}\sum_{i}^{N}\nabla_i^2 - \frac{1}{2}\sum_{A}^{M}\frac{1}{m_A}\nabla_A^2 - \sum_{i}^{N}\sum_{A}^{M}\frac{Z_A}{r_{iA}} + \frac{1}{2}\sum_{i}^{N}\sum_{j\neq i}^{N}\frac{1}{r_{ij}} + \frac{1}{2}\sum_{A}^{M}\sum_{B\neq A}^{M}\frac{Z_A Z_B}{r_{AB}} \tag{2.2}$$

or

$$\hat{\mathcal{H}} = \hat{T}_e + \hat{T}_n + \hat{V}_{ne} + \hat{V}_{ee} + \hat{V}_{nn} \tag{2.3}$$

where A and B run over the nuclei and i and j over the electrons. $\hat{T}_e$ and $\hat{T}_n$ represents the kinetic energy of the electrons and nuclei respectively. $\hat{V}_{ne}$ represent the attractive potential resulting from the electrostatic interactions between the nuclei and the electrons, $\hat{V}_{ee}$ and $\hat{V}_{nn}$ are the repulsive potentials due to the electron-electron and nucleus-nucleus interactions respectively. m_A and Z_A are respectively the mass and the number of protons of the nucleus A. r_{pq} is the distance between the particles p and q. ∇^2 is the Laplacian operator. The factor of $1/2$ in the two last terms avoid to double counting interactions (since $1/r_{ij} = 1/r_{ji}$).

The Schrödinger equation can be solved exactly for only a few problems, and for molecular systems, the Born-Oppenheimer approximation [78] is necessary. It allows to concentrate on the electronic motion by decoupling it from the motion of the nuclei. This approximation is based on the fact that the masses of the nuclei are much greater than the masses of the electrons (approximately 1800 times for the proton), meaning that the nuclei move much slower than the electrons. Thus, the electrons can be considering as moving in a static field of nuclei. The electronic Hamiltonian can then be written as follow:

$$\hat{\mathcal{H}}_e = -\frac{1}{2}\sum_{i}^{N}\nabla_i^2 - \sum_{i}^{N}\sum_{A}^{M}\frac{Z_A}{r_{iA}} + \sum_{i}^{N}\sum_{j\neq i}^{N}\frac{1}{r_{ij}} = \hat{T}_e + \hat{V}_{ne} + \hat{V}_{ee} \tag{2.4}$$

where $\hat{V}_{ne}$ can also be called V_{ext}, and is the only term dependent on the positions and charges of the nuclei. Thus the total energy of the system can be expressed as the sum of the electronic and nuclear contribution:

$$E_{tot} = E_e + E_n \quad with \quad E_n = \sum_{A}^{M}\sum_{B>A}^{M}\frac{Z_A Z_A}{r_{AB}} \tag{2.5}$$

In order to solve the Schrödinger equation for an arbitrary molecule, firstly, the Hamiltonian operator of the system must be set up. The above Hamiltonian shows that the only system-

dependent parameters are the number of electrons in the system, as well as the positions and charges of the nuclei. Secondly, the eigenfunctions Ψ_i and corresponding eigenvalues E_i of $\hat{\mathcal{H}}$ have to be found. However, except in a few, trivial cases, the eigenfunctions cannot be found analytically and some methods are needed to approach it. Two classes of theories exist: the wave function-based methods and the density-based theories, where the variational method is used to find an upper bound value of the ground true energy of the ground state using trials of the eigenfunction or density function, respectively.

2.2 The Density Functional Theory

The density functional theory (DFT) is based on the Hohenberg-Kohn theorems [79]. The interest of the Hohenberg-Kohn theorems is the consideration of the electron density as the only variable to solve a many-body problem whereas wave function theories consider a N-electron wave function depending on 3N spatial, and N spin degrees of freedom. The first theorem states that for any system of interacting electrons submitted to an external potential $V_{ext}(\mathbf{r})$, the external potential acting on a system of interacting electrons is a unique functional of the density $n(\mathbf{r})$. The second theorem says that a universal functional for the energy $E[n(\mathbf{r})]$ can be defined in function of the electronic density. The exact ground state of the system is the global minimum value of this functional. This means that for any external potential $V_{ext}(\mathbf{r})$, the ground state energy E_0 is a functional of the ground state density $n_0(\mathbf{r})$ and can be determined by the variational method:

$$E_0 = E[n_0(\mathbf{r})] \leq E[n(\mathbf{r})] \tag{2.6}$$

In order to solve the Kohn-Sham equation, the self-consistent procedure must be followed:

1. Guess of the initial density $n_0(\mathbf{r})$ from an initial set of orbitals $\psi_0(\mathbf{r})$.

2. Calculate the electron density $n(\mathbf{r})$ and the Kohn-Sham effective potential $v_{KS}^{\sigma}(\mathbf{r})$:

$$n(\mathbf{r}) = \sum_{\sigma} n(\mathbf{r}, \sigma) = \sum_{\sigma} \sum_{i=1}^{N^{\sigma}} \left|\psi_i^{\sigma}(\mathbf{r})\right|^2 \tag{2.7}$$

$$v_{KS}^{\sigma}(\mathbf{r}) = v_{ext}(\mathbf{r}) + \int \mathrm{d}^3 r \, \frac{n(\mathbf{r}\prime)}{|\mathbf{r} - \mathbf{r}\prime|} + \frac{\delta E_{xc}}{\delta n(\mathbf{r}, \sigma)} \tag{2.8}$$

3. Solve the N single particle system, writing $\psi_i^\sigma(\mathbf{r})$ as a linear combination of single particle orbitals. i.e by diagonalizing the matrix $\left(-\frac{1}{2}\nabla^2 + v_{KS}^\sigma(\mathbf{r})\right)\psi_i^\sigma(\mathbf{r})$:

$$\left(-\frac{1}{2}\nabla^2 + v_{KS}^\sigma(\mathbf{r})\right)\psi_i^\sigma(\mathbf{r}) = \epsilon_i^\sigma \psi_i^\sigma(\mathbf{r}) \qquad i = 1, 2, ..., N \tag{2.9}$$

4. Recompute the density $n(\mathbf{r})$ from Equation (2.7) and check for convergence.

2.3 Molecular Mechanics

Because of a high computational cost, large scale systems cannot be handled by quantum mechanics program. In order to deal with systems containing many atoms, the electronic motions has to be ignored. Empirical force field (FF) methods, used in molecular dynamics, can give a reasonably accurate interpretation of a system by calculating the total energy as a function of the nuclear positions only. Molecular mechanics methods are based on two assumptions: the first is the Born-Oppenheimer approximation, i.e the nuclei are assumed frozen with respect to the electrons. The second is that each nucleus is treated as a classical particle. That is, every forces acting on the particle of the system obey the laws of classical mechanics. One example of the functional form of a simple molecular force field is the following:

$$\begin{aligned}\mathcal{U}(\mathbf{r}) &= E_{bond} + E_{angle} + E_{torsion} + E_{Coulomb} + E_{LJ} \\ &= \sum_{bonds} \frac{k_{ij}}{2}(r_{ij} - r_{ij,0})^2 + \sum_{angles} \frac{k_{ijk}}{2}(\theta_{ijk} - \theta_{ijk,0})^2 + \sum_{torsions} \frac{V_n}{2}(1 + cos(n\omega - \gamma)) \\ &+ \sum_{i=1}^{N}\sum_{j=i+1}^{N} \frac{q_i q_j}{4\pi\varepsilon_0\varepsilon_r r_{ij}} + \sum_{i=1}^{N}\sum_{j=i+1}^{N} 4\varepsilon_{ij}\left[\left(\frac{\sigma_{ij}}{r_{ij}}\right)^{12} - \left(\frac{\sigma_{ij}}{r_{ij}}\right)^{6}\right]\end{aligned} \tag{2.10}$$

$\mathcal{U}(\mathbf{r})$ is the total interaction potential, function of the position vector $\mathbf{r}$ of N particles. In this case, it is composed of five contributions: bond stretching E_{bond}, angle bending E_{angle}, bond rotation (torsion) $E_{torsion}$, non-bonded electrostatic interaction $E_{Coulomb}$ and short range interaction E_{LJ}. In the bonded interaction potential, k_{ik} and k_{ijk} are the stretching and bending force constants, r_{ij} and θ_{ijk} are the current bond lengths and angles, $r_{ij,0}$ and $\theta_{ijk,0}$ are the reference bond lengths and angles, V_n is the torsional rotational force constant, ω is the current torsional angle, n is the multiplicity factor and γ is the phase factor. Most of the time, excepted for angles and dihedrals interactions, pair potentials are employed. In the non-bonded interactions, the short range interaction term is described as a Coulomb potential: q_i and q_j

are the atomic charges of a pair of atoms i and j separated by a distance r_{ij}, ε_0 is the vacuum permittivity and ε_r is the dielectric constant. The short range interactions are modelled by a common Lennard-Jones (LJ) function, where ε_{ij} is the depth of the potential well, and σ_{ij} is the distance between two atoms i and j at which the potential is zero ($r_{ij} = \sigma_{ij}$).

2.3.1 Short-Range Interactions

Short range interactions only consider particles within a cutoff distance between each others. Most of the time, being r the separating distance of a pair of atoms, this computational artifact is used for Lennard-Jones potential, for which the repulsive ($\propto r^{-12}$ or $\propto r^{-9}$) and attractive contributions ($\propto r^{-6}$) drop down to zero much faster than a Coulomb potential ($\propto 1/r$). For a pair of atoms i and j, separated by a distance r_{ij}, with parameters σ_i, ϵ_i and σ_j, ϵ_j respectively, the 12-6 Lennard-Jones potential is:

$$u_{LJ}(r_{ij}) = 4\varepsilon_{ij}\left[\left(\frac{\sigma_{ij}}{r_{ij}}\right)^{12} - \left(\frac{\sigma_{ij}}{r_{ij}}\right)^{6}\right] \tag{2.11}$$

Several mixing, or combining rules can be employed to calculate the parameters of a pair of atoms of different species:

- the arithmetic, or Lorentz-Berthelot rule:

$$\sigma_{ij} = \frac{\sigma_i + \sigma_j}{2} \qquad \varepsilon_{ij} = \sqrt{\varepsilon_i \varepsilon_j} \tag{2.12}$$

- the geometric rule:

$$\sigma_{ij} = \sqrt{\sigma_i \sigma_j} \qquad \varepsilon_{ij} = \sqrt{\varepsilon_i \varepsilon_j} \tag{2.13}$$

- the sixth-power rule:

$$\sigma_{ij} = \left(\frac{\sigma_i^6 + \sigma_j^6}{2}\right)^{1/6} \qquad \varepsilon_{ij} = \frac{2\sqrt{\varepsilon_i \varepsilon_j}\sigma_j^3 \sigma_j^3}{\sigma_j^6 + \sigma_j^6} \tag{2.14}$$

2.3.2 Long-Range Interaction

Classically, the Coulomb contribution to the potential energy of a cubic system of length L, electrically neutral and containing N particles, i.e. $\sum_i q_i = 0$, is:

$$E_{Coulomb} = \frac{1}{2}\sum_{i=1}^{N} q_i \phi(r_i) \tag{2.15}$$

where q_i is the charge, and $\phi(r_i)$ is the electrostatic potential of the ion i, which can be written as follows:

$$\phi(r_i) = \sum_{j \neq i, \mathbf{n}} \frac{q_j}{\left|\mathbf{r}_{ij} + \mathbf{n}L\right|} \tag{2.16}$$

where the sum is over all particles j different from i in all periodic images $\mathbf{n}$, including the images of i.

In systems such as ionic solids, where the electrostatic interactions are leading and acting up to several nanometers, truncation of the Coulomb potential would lead to inaccurate results. However, the calculation of pair interactions one by one would be computationally expensive (proportional to the square of the number of particles). To prevent this arduous calculation, several methods have been developed to handle long-range interactions. Among them, the Ewald summation remains the most widely used. The Ewald sum method consists in neutralizing the charge of ions at long range by superposing at their center a spherical Gaussian distribution of opposite charge. This first part is the short range term, computed in real space. To compensate the introduction of these Gaussian distribution, a set of Gaussian distribution with the same charge as the original ions is introduced. The electrostatic potential due to this charge distribution is obtained from the Poisson's equation (also used in DFT), and solved as a Fourier series in the reciprocal space. In addition to these two contributions, the total electrostatic potential includes correction terms for self-interaction and surface dipole [80].

2.4 Energy Minimisation Methods

When studying statically a system which potential energy is described by a molecular FF, it is important to reach an energetically favourable configuration of the system. The purpose of energy minimisation (EM) methods is to find atomical arrangements for which the system is the most stable. Though it is very useful to perform static calculations at low computational cost, EM does not include entropic contribution. In principle, for solids, this contribution is very small and negligible compared to the cohesive energy contribution. However, a dynamical study is often preferred over a static one for two reasons:

1. the sample can be simulated under desired temperature condition;

2. thermal treatment and time integration allow for statistical interpretation;

Nonetheless, when the positions of atoms are *a priori* known, EM is usually performed before starting a MD simulation to find the closest minimum energy configuration using a specific force field.

The potential energy functional is often referred as the potential energy surface (PES) or hypersurface. Actually, the visualization of the PES is only possible when the potential energy is only function of one or two variables. For the PES of an entire system, there may exist various local energy minima, the lowest of them is called global energy minimum. Since traditional EM methods find the nearest local minima, the computed lower energy will largely depends on the initial configuration of the system. To find the lowest energy configuration of a system, EM methods use derivatives of the potential energy. Indeed, the force acting on the atoms is minus the gradient of its potential energy, and the second derivatives represent the curvature of the energy function, which can be used to predict where the function will change of direction. The Taylor series expansion of the potential energy about the current configuration $\mathbf{r}_i$ of the system can be written as follows:

$$\mathcal{U}(\mathbf{r}) = \mathcal{U}(\mathbf{r}_i) + (\mathbf{r} - \mathbf{r}_i)\frac{\mathrm{d}\mathcal{U}(\mathbf{r}_i)}{\mathrm{d}\mathbf{r}} + \frac{1}{2}(\mathbf{r} - \mathbf{r}_i)^T \cdot \frac{\mathrm{d}^2\mathcal{U}(\mathbf{r}_i)}{\mathrm{d}\mathbf{r}^2} \cdot (\mathbf{r} - \mathbf{r}_i) + \dots \tag{2.17}$$

The position vector $\mathbf{r}$ of N atoms has $3N$ components, so $\mathrm{d}\mathcal{U}(\mathbf{r}_i)/\mathrm{d}\mathbf{r}$ is a $3N$ vector composed of the partial derivatives of the potential function with respect to the respective coordinates, and $\mathrm{d}^2\mathcal{U}(\mathbf{r}_i)/\mathrm{d}\mathbf{r}^2$ is a $3N\times3N$ second derivative matrix, called the *Hessian* matrix of $\mathcal{U}(\mathbf{r})$. The steepest descent and conjugate gradient are first derivative methods which change the atoms positions at each iteration from the initial to the more energetically stable configuration, using the gradient $\mathbf{g}_k$ to find the direction $\mathbf{v}_k$ of the movement on the PES. In the steepest descent method, the evaluation of the energy is done by moving in directions parallel to the gradient, while in the conjugate gradient method, directions are *conjugate* [81, 82]:

$$\mathbf{v}_k = -\mathbf{g}_k + \gamma_k \mathbf{v}_{k-1} \tag{2.18}$$

where γ_k is a constant scalar given by

$$\gamma_k = \frac{\mathbf{g}_k \cdot \mathbf{g}_k}{\mathbf{g}_{k-1} \cdot \mathbf{g}_{k-1}} \tag{2.19}$$

The second order Newton-Raphson method makes use of the *Hessian* matrix, i.e the matrix of the second derivatives of the function to minimize. Considering a Taylor expansion (Equation (2.17)) of the first order of the potential energy $\mathcal{U}$ at a configuration $\mathbf{r}_i$ near from a stationary point and differentiating:

$$\frac{\mathrm{d}\mathcal{U}(\mathbf{r})}{\mathrm{d}\mathbf{r}} = \frac{\mathrm{d}^2\mathcal{U}(\mathbf{r}_i)}{\mathrm{d}\mathbf{r}^2} + (\mathbf{r} - \mathbf{r}_i)\frac{\mathrm{d}\mathcal{U}(\mathbf{r}_i)}{\mathrm{d}\mathbf{r}} = 0 \tag{2.20}$$

The iterative scheme can thus be written:

$$\mathbf{r}_{i+1} = \mathbf{r}_i - \frac{\mathrm{d}^2\mathcal{U}(\mathbf{r}_i)\,/\,\mathrm{d}\mathbf{r}^2}{\mathrm{d}\mathcal{U}(\mathbf{r}_i)/\mathrm{d}\mathbf{r}} \tag{2.21}$$

2.5 Molecular Dynamics

In molecular dynamics simulation, in addition to the potential energy, the kinetics energy contribution is introduced by integrating Newton's laws of motion. The energy of a system of particles is defined by its Hamiltonian, sum of the potential and kinetic energies, noted $\mathcal{U}$ and $\mathcal{K}$ respectively:

$$\mathcal{H}(\mathbf{q}, \mathbf{p}) = \mathcal{U} + \mathcal{K} = \mathcal{U}(\mathbf{q}) + \frac{1}{2}\mathbf{p}^T\mathbf{M}\mathbf{p} \tag{2.22}$$

The potential energy is a function of the position vector $\mathbf{q}$ (in phase space), the kinetic energy is function of the momentum vector $\mathbf{p}$ and mass matrix $\mathbf{M}$ (time-independent). The Hamilton's equations of motion allows to update particles positions and momenta at each step:

$$\dot{\mathbf{p}} = -\boldsymbol{\nabla}_{\mathbf{q}}\mathcal{H} \qquad \dot{\mathbf{q}} = \boldsymbol{\nabla}_{\mathbf{p}}\mathcal{H} \tag{2.23}$$

Since the momentum vector $\mathbf{p} = \mathbf{M}\dot{\mathbf{q}}$, and the kinetic energy $\mathcal{K}$ depends only on $\mathbf{p}$, the first Hamilton's equation can be reduced to the Newton's equation of motion:

$$\mathbf{F}(\mathbf{q}) = -\boldsymbol{\nabla}_{\mathbf{q}}\mathcal{U} = \mathbf{M}\ddot{\mathbf{q}} \tag{2.24}$$

Therefore, a trajectory of every particle of the system can be produced, specifying their position and velocity variation over the time. The most employed algorithm to integrate the equation of motion is the Verlet algorithm. It uses a Taylor series expansions to express the position vector $\mathbf{r}$ at a time t and $t + \delta t$ in function of the positions, the velocity vector $\mathbf{v}$ and the acceleration vector $\mathbf{a}$ at time t:

$$\mathbf{r}(t + \delta t) = \mathbf{r}(t) + \delta t\mathbf{v}(t) + \frac{1}{2}\delta t^2\mathbf{a}(t) + \mathcal{O}\left(t^3\right) \tag{2.25}$$

$$\mathbf{r}(t - \delta t) = \mathbf{r}(t) - \delta t\mathbf{v}(t) + \frac{1}{2}\delta t^2\mathbf{a}(t) - \mathcal{O}\left(t^3\right) \tag{2.26}$$

When adding Equations (2.25) and (2.26), we obtain the velocity independent relation:

$$\mathbf{r}(t+\delta t) = 2\mathbf{r}(t) - \mathbf{r}(t-\delta t) + \frac{1}{2}\delta t^2 \mathbf{a}(t) + O\left(t^4\right) \tag{2.27}$$

The velocities can be derived as follows by subtracting Equations (2.25) and (2.26):

$$\mathbf{v}(t) = [\mathbf{r}(t+\delta t) - \mathbf{r}(t-\delta t)]/2\delta t + O\left(t^2\right) \tag{2.28}$$

At the first iteration, Equation (2.25) is used to compute $\mathbf{r}(\delta t)$ as a function of the initial positions and velocities.

2.6 *ab initio* Molecular Dynamics

The classical molecular dynamics uses predefined potential parameters, where the topology of the system is fixed during simulation. This can be considered as a limitation for systems where chemical reactions occurs. *ab initio* molecular dynamics (AIMD) overcomes this limitation by computing forces acting on atomic nuclei from electronic structure calculation such as DFT (see Figure 2.1).

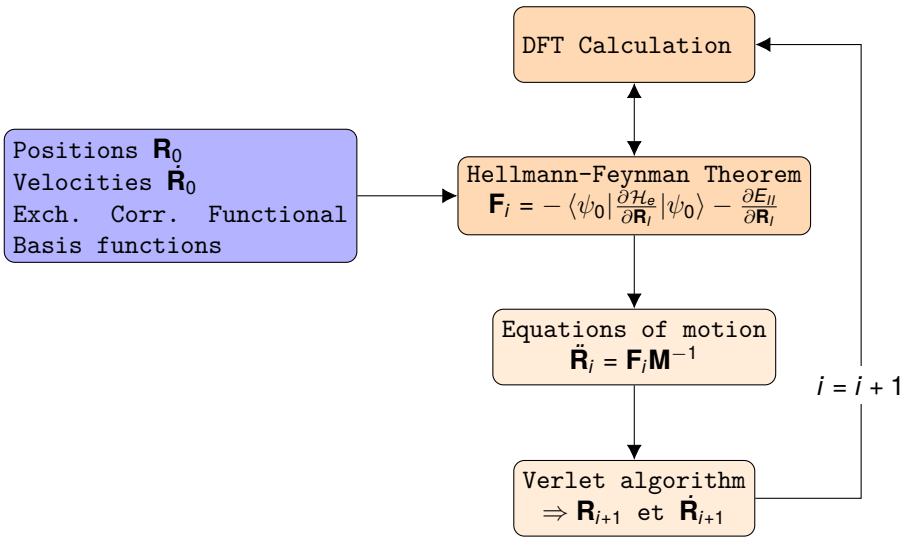

Figure 2.1. A general AIMD algorithm.

The first approach was proposed by Car and Parrinello, and called by their names as Car-Parinello molecular dynamics (CPMD). In this method, the self consistent loop expressed in Section 2.2 is solved one time, and the electronic motion is computed fictitiously when integrating the equations of motion. The most accurate method is the Born-Oppenheimer molecu-

lar dynamics (BOMD), were the self-consistent loop is solved at each time step. The Hellmann-Feynman theorem states that, knowing the spatial distribution of electrons, every forces in the system can be computed using classical electrostatics:

$$-\frac{\partial E}{\partial \mathbf{R}_I} = -\langle\psi|\frac{\partial\hat{\mathcal{H}}}{\partial \mathbf{R}_I}|\psi\rangle - \frac{\partial E_{II}}{\partial \mathbf{R}_I} = -\int \mathrm{d}^3 n(\mathbf{r})\,\frac{\partial v_{ext}(\mathbf{r})}{\partial \mathbf{R}_I} - \frac{\partial E_{II}}{\partial \mathbf{R}_I} \tag{2.29}$$

where $\mathbf{R}_I$ is the nuclei coordinate vector and E_{II} is the energy due to the interaction between nuclei.

2.7 Statistical Mechanics

As MM methods are based on the principle that an empirical, classical mechanics model can describe an atomic system, basics law of statistical mechanics must be used to link particles interactions and motion to bulk properties such as volume, pressure or temperature. Over the time t, the instantaneous value of a property A fluctuates because of particles motion and interaction. Thus, A is a function of the position vector $\mathbf{q}(t)$ and the momentum vector $\mathbf{p}(t)$. The precision of a measurement will increase with the time τ over which the measure is made, and one defined as *time average* the average of a measured value over a sufficiently long time.

$$\langle A\rangle = \lim_{\tau\to\infty}\frac{1}{\tau}\int_{t=0}^{\tau} A(\mathbf{q}(t),\mathbf{p}(t))\mathrm{d}t \tag{2.30}$$

Let us consider a *closed system*, that is, a system that can exchange energy but no matter with his surrounding. Thus, this system has a fix volume V and number of particles N and is in constant thermal equilibrium with the environment, at a temperature T. It can be described, at any instant, by its energetic configuration, where N_0 particles are in the energy state E_0, N_1 in E_1, and so on. Thus, the distribution of populations of the energy states i can be described by the Boltzmann distribution, which is the probability p_i to find a subsystem composed by N_i particles with an energy ε_i:

$$p_i = \frac{N_i}{N} = \frac{\exp(-\varepsilon_i/kT)}{\sum_j \exp\left(-\varepsilon_j/kT\right)} = \frac{\exp(-\varepsilon_i/kT)}{q} \tag{2.31}$$

where T is the temperature of the system, k is the Boltzmann's constant and the denominator q is called *partition function*. This function is then a normalization constant, because the sum of the probabilities p_i must be equal to 1. From the energy distribution, the energy of the system

can be computed in function of the partition function and the temperature:

$$E_i = \sum_i \varepsilon_i p_i = -\frac{\partial \ln q}{\partial(1/kT)} \tag{2.32}$$

The *phase space* of a dynamical system is the space containing all possible states of this system. An *ensemble* is an imaginary collection of replicated systems moving in the phase space. This concept allows to reproduce the configuration of the system of interest as many time as we like and to define a canonical distribution function, where Q is the canonical partition function:

$$\frac{\tilde{N}_i}{\tilde{N}} = \frac{\exp(-E_i/kT)}{Q} \quad \text{with} \quad Q = \sum_j \exp\left(-E_j/kT\right) \tag{2.33}$$

$\tilde{N}$ is the total number of systems in the ensemble, and $\tilde{N}_i$ is the number of systems with an energy E_i. Several ensembles exist:

1. The *microcanonical ensemble* (NVE) is a collection of systems with a fix volume V, number of particles N and total energy E. The systems are isolated from their environment, meaning that they cannot exchange energy between them.

2. The *canonical ensemble* (NVT) is a collection of systems with a fix volume V and number of particles N in constant thermal equilibrium with their environment, at a temperature T. The systems of this ensemble can thus exchange energy as heat.

3. The *isobaric-isothermal ensemble* (NpT) is a collection of systems with a fix pressure p and number of particles N in constant thermal and pressure equilibrium with their environment, at a temperature T, and pressure p. These systems can exchange energy as heat and work to equilibrate.

4. The *grand canonical ensemble* (μVT) is a collection of systems with a fix volume V, temperature T and chemical potential μ. These systems can exchange heat and atoms between them.

The concept of ensemble allows to average a property over a great number of configuration that satisfies the same thermodynamic state, this is called an *ensemble average*:

$$\langle A \rangle = \iint \mathrm{d}\mathbf{q}\mathrm{d}\mathbf{p} A(\mathbf{q}, \mathbf{p}) P(\mathbf{q}, \mathbf{p}) \tag{2.34}$$

where $A(\mathbf{q}, \mathbf{p})$ is the property value in one point of the phase space and $P(\mathbf{q}, \mathbf{p})$ is the probability of the system to be in that point. The *ergodic hypothesis* states that, for an isolated system at

the equilibrium, all the accessible states are equally probable over a long time period, and are independent of the initial configuration of the system. This assumption is very convenient in MD where a property of a many-particle system is averaged over time and means that for a sufficient simulation time, this average is equal to the average over a large number of replication of the system – i.e., *ensemble average*.

2.8 Thermostat Algorithms

In many MD studies, the canonical ensemble is used to describe the system at a desired temperature. In such ensemble, the instantaneous temperature fluctuates around the thermostat temperature T_0 and different algorithms exist to simulate a canonical ensemble. The instantaneous temperature T of a canonical system with N particles can be derived from the equipartition theorem:

$$\mathcal{K} = \sum_{i=1}^{N} \frac{\mathbf{p}_i}{2m_i} = \frac{kT}{2} N_f \tag{2.35}$$

where, $\mathbf{p}_i$ and m_i are the momentum and mass of the particle, $N_f = 3N - N_c$ is the number of degrees of freedom and N_c the number of constraints. The Berendsen formulation consists to scale the velocities in the system such that the deviation from T_0 decays exponentially with a time constant τ:

$$\frac{\mathrm{d}T}{\mathrm{d}t} = \frac{T_0 - T}{\tau} \tag{2.36}$$

This method allows a fast equilibration of the system but does not generate a correct canonical ensemble. So it is preferentially used in an equilibration run, during which the system is allowed to relax until its energy is stable. On the other hand, a Nosé-Hoover thermostat is a better choice for a production run, during which the desired physical quantities (e.g., positions, velocities) are collected to be post-treated.

The Nosé-Hoover thermostat is based on the integration of the heat bath in the system. This introduces an additional degree of freedom s to the Hamiltonian, with an associated effective mass Q. s represents the external contribution of the heat bath on the system of N particles. It can be interpreted as scaling factor of the time step, between the physical system defined by the real variables t', $\mathbf{r}'_i$, $\mathbf{p}'_i$ and the extended system, defined by the virtual variables

t, $\mathbf{r}_i$, $\mathbf{p}_i$:

$$\mathbf{r}'_i = \mathbf{r}_i, \quad \mathbf{p}'_i = \mathbf{p}_i/s, \quad s' = s, \quad p'_s = p_s/s, \quad \Delta t' = \Delta t/s \tag{2.37}$$

Moreover, a potential energy $g \ln s\ \beta$ is associated to the variable s, and the Hamiltonian of the extended system is:

$$\mathcal{H}_{Nose} = \sum_{i=1}^{N} \frac{\mathbf{p}_i}{2m_i s^2} + \mathcal{U}(\mathbf{r}) + \frac{p_s^2}{2Q} + g\frac{\ln s}{\beta} \tag{2.38}$$

where $p_s = Q\dot{s}$ is the conjugate momentum of s and g is a parameter essentially equal to the number of degrees of freedom. This Hamiltonian leads to the following equation of motions:

$$\begin{aligned}
\dot{\mathbf{r}}_i &= \frac{\partial \mathcal{H}_{Nose}}{\partial \mathbf{p}_i} = \frac{\mathbf{p}_i}{m_i s^2} \\
\dot{\mathbf{p}}_i &= -\frac{\partial \mathcal{H}_{Nose}}{\partial \mathbf{r}_i} = -\frac{\partial \mathcal{U}(\mathbf{r})}{\partial \mathbf{r}_i} \\
\dot{s} &= \frac{\partial \mathcal{H}_{Nose}}{\partial p_s} = \frac{p_s}{Q} \\
\dot{p_s} &= -\frac{\partial \mathcal{H}_{Nose}}{\partial s} = \left(\sum_{i=1}^{N} \frac{\mathbf{p}_i}{2m_i s^2} - \frac{g}{\beta}\right)/s
\end{aligned} \tag{2.39}$$

To avoid fluctuations of time step, it is more convenient to sample the equation of motion for the real formulation, thus expressing the Equation (2.39) as derivatives with respect to t'. The resulting equations of motion are (conserving the dot notation) [83, 84]:

$$\begin{aligned}
\dot{\mathbf{r}}'_i &= \frac{\mathbf{p}'_i}{m_i s} \\
\dot{\mathbf{p}}'_i &= -\frac{\partial \mathcal{U}(\mathbf{r}')}{\partial \mathbf{r}'_i} - \xi \mathbf{p}'_i \\
\dot{\xi} &= \left(\sum_{i=1}^{N} \frac{\mathbf{p}'^2_i}{m_i} - \frac{g}{\beta}\right)/s
\end{aligned} \tag{2.40}$$

with $\xi = s' p'_s/Q$ being a thermodynamic friction coefficient, $g = 3N$ in the real formulation and $g = 3N + 1$ in the virtual formulation. The following quantity is conserved, but is not an Hamiltonian, because the equation of motion cannot be derived from it [80, 83]:

$$\mathcal{H}'_{Nose} = \sum_{i=1}^{N} \frac{\mathbf{p}'_i}{2m_i s^2} + \mathcal{U}(\mathbf{r}') + \frac{s'^2 p'^2_s}{2Q} + g\frac{\ln s'}{\beta} \tag{2.41}$$

The Nose-Hoover method is thus often called as non-Hamiltonian dynamics method. The magnitude of the effective mass of the heat bath Q controls the strength of the coupling with the system. Too large values of Q will result in a poor coupling, while a too small Q could cause undesired high-frequency temperature oscillations.

2.9 Force Fields

2.9.1 INTERFACE FF

The INTERFACE FF (IFF) is an extension of existing force fields (PCFF, COMPASS, CVFF, CHARMM, AMBER, OPLS-AA), offering parameters for a broad range of materials, including clays and construction ones [72]. There are two expressions of the potential energy, depending on the FF employed, where $E_{out-of-plane}$ is the bending energy of an atom out of the plane formed by other atoms, and E_{Hbonds} is the hydrogen bonds energy:

$$\begin{aligned} E_{pot} = & \underbrace{\sum_{ij} K_{r,ij}(r_{ij} - r_{0,ij})^2}_{E_{bond}} + \underbrace{\sum_{ijk} K_{\theta,ijk}(\theta_{kij} - \theta_{0,ijk})^2}_{E_{angle}} \\ & + \underbrace{\sum_{ijkl} V_{\varphi,ijkl}[1 + cos(\varphi_{ijkl} - \varphi_{0,ijkl})]}_{E_{torsion}} + \underbrace{\sum_{ijkl} K_{\chi,ijkl}(\chi_{ijkl} - \chi_{0,ijkl})^2}_{E_{out-of-plane}} \\ & + \underbrace{\frac{1}{4\pi\varepsilon_0\varepsilon_r}\sum_{ij}\frac{q_i q_j}{r_{ij}}}_{E_{Coulomb}} + \underbrace{\sum_{ij}\varepsilon_{0,ij}\left[\left(\frac{\sigma_{ij}}{r_{ij}}\right)^{12} - 2\left(\frac{\sigma_{ij}}{r_{ij}}\right)^{6}\right]}_{E_{vdWaals}} + E_{Hbond} \end{aligned} \tag{2.42}$$

$$\begin{aligned} E_{pot} = & \sum_{ij}\sum_{n=2}^{4} K_{r,ij}(r_{ij} - r_{0,ij})^n + \sum_{ijk}\sum_{n=2}^{4} K_{\theta,ijk}(\theta_{ijk} - \theta_{0,ijk})^n \\ & + \sum_{ijkl}\sum_{n=2}^{3} V_{\varphi,ijkl}[1 + cos(\varphi_{ijkl} - \varphi_{0,ijkl})] + \sum_{ijkl} K_{\chi,ijkl}(\chi_{ijkl} - \chi_{0,ijkl})^2 \\ & + \frac{1}{4\pi\varepsilon_0\varepsilon_r}\sum_{ij}\frac{q_i q_j}{r_{ij}} + \sum_{ij}\varepsilon_{0,ij}\left[2\left(\frac{\sigma_{ij}}{r_{ij}}\right)^{9} - 3\left(\frac{\sigma_{ij}}{r_{ij}}\right)^{6}\right] + E_{Hbond} \end{aligned} \tag{2.43}$$

Regarding to nonbonded interactions, these two expressions vary on their Lennard-Jones (LJ) potential (9-6 for Class II FF and 12-6 Class I FF). For bonded interactions, Class II FF (PCFF, COMPASS) contains cubic and quartic bond, angle and torsion terms compared to Class I FF. However, only quadratic bonded terms where parametrized for C_3S (see Table 2.1).

The PCFF and COMPASS potentials expressed in Equation (2.43) uses a sixth-power mixing rule, and excludes non-bonded interactions for 1-2 and 1-3 bonded atoms. On the contrary, Class I FF are based on arithmetic (AMBER, CHARMM) or geometric (CVFF, OPLS-AA) mixing

Non-bonded (9-6 PCFF LJ)			
Atom	charge (e)	$r_{0,ij}$ (Å)	$\varepsilon_{0,ij}$ (kcal mol^{-1})
Ca	+1.50	3.70	0.24
Hh	+0.30	1.098	0.013
Hsi	+0.40	1.098	0.013
Oi	-1.5	3.80	0.06
Oh	-1.05	3.60	0.12
Os	-1.0	3.40	0.06
Osi	-0.65	3.60	0.12
Si	+1.0	4.80	0.40

Bonds			Angles		
Bond	$r_{0,ij}$ (Å)	$K_{r,ij}$ (kcal Å^{-2})	Angle	$\theta_{0,ij}$ (°)	$K_{\theta,ij}$ (kcal rad^{-2})
Hh-Oh	0.929	495	Hh-Oh-Si	109.5	160
Hsi-Osi	0.929	495	Hsi-Osi-Si	109.5	160
Os-Si	1.68	250	Os-Si-Os	115	50

Table 2.1. INTERFACE FF parameters for dry and hydrated C_3S [71]. Hh and Oh are hydrogen and oxygen in hydroxides. Hs and Os are hydrogen and oxygen in silicates. Hsi and Osi are hydrogen and oxygen in silanol groups.

rules. The IFF offers consistent descriptions of chemical bonding and dipole moments, allowing to describe both bulk and surface properties accurately. It reproduces structural properties of $M_3\,C_3S$ in good agreement with experimental results, and was used to compute cleavage energies. Moreover, the initial hydration, and adsorption of organic molecules from grinding aids onto the (040) surface were investigated in dry or wet conditions [64]. The wetting of the alite surface was modeled by hydration of the superficial oxide ions including parameters for oxygen and hydrogen. The same research group introduced parameters for tricalcium aluminate C_3A to provide understanding on the hydration reaction, surface agglomeration and interaction with organic molecules [85]. They reproduced atomic coordinates, elastic moduli, thermal expansion and cleavage energies in excellent agreement with experimental data. More recently, the first model, including parameters for the dry C_3S as well as superficial hydroxyl group [64] was extended to take into account further hydration steps, by adding parameters for silanol groups. The new parameters allowed to simulate the adsorption of aluminate ions on an hydroxylated C_3S surface [71] at low pH values. The simulations performed by the authors started with intermediate steps of hydration, defined by the number of hydroxylated molecular layers. The authors showed that above a pH of 13, desorption of aluminates occurs because of the interaction between the surface and ions of high charge. Despite the pertinence of these results, and the larger space and time scale reachable by this classical force field, it cannot capture the evolution of the bonds during the simulation, which is a limitation when investigating reactive systems.

2.9.2 ClayFF Force Field

ClayFF is a general force field initially developed to describe interfaces between various mineral systems and water [73], and in particular adsorption of ions, with environmental application among others. It uses a flexible single point charge (SPC) water model and its potential energy functional is relatively classic:

$$E_{pot} = E_{Coul} + E_{vdW} + E_{bond} + E_{angle} \tag{2.44}$$

A 12-6 Lennard-Jones potential describes the van der Waals energy term:

$$E_{vdW} = \sum_{i \neq j} D_{0,ij} \left[\left(\frac{R_{0,ij}}{r_{ij}}^{12} \right) - 2 \left(\frac{R_{0,ij}}{r_{ij}}^{6} \right) \right] \tag{2.45}$$

The LJ mixing rule is originally arithmetic, although some recent investigations are performed with geometric mixing rules [86]. Its originality is based on the fact that only hydroxyl groups are represented by bonded, harmonic terms. This philosophy makes ClayFF a very versatile force field. In counterpart, the covalent contribution of bonds is underestimated when compared to the ionic contribution. In silicates for example, the charge for tetrahedral silicon (2.1e) is more than two times the charge employed in IFF (1.0e), to balance for the lack of covalent interaction. In the context of cementitious materials, ClayFF has been used extensively to simulate interfaces of C – S – H and others hydrated phases with water, and particularly the adsorption of ions on C – S – H surfaces [87–89], but also to investigate screw dislocations in C_2S and C_3S [61, 62]. The parameters for C_3S are presented in Table 2.2.

Atom	charge (e)	$D_{0,ij}$ (Å)	$R_{0,ij}$ (kcal mol^{-1})
Ca	+1.05	5.0298×10^{-6}	6.2428
O	-1.05	0.1554	3.5532
Si	+2.1	1.8405×10^{-6}	3.7064

Table 2.2. ClayFF parameters for dry C_3S [73]

2.9.3 ReaxFF Force Field

The ReaxFF reactive FF was developed to bridge the gap between classical MD and QM, allowing atoms to move from one chemical species to another and thus to describe reactive events. Its overall energy functional is described as follows:

$$E_{system} = E_{bond} + E_{over} + E_{angle} + E_{tors} + E_{vdWaals} + E_{Coulomb} + E_{specific} \tag{2.46}$$

where E_{bond} is function of bond-orders and associated dissociation energies. E_{over} is a energy penalty for overcoordinated atoms. $E_{specific}$ includes energy terms specific for particular systems, as hydrogen bonding and lone pairs in water molecules, or conjugation for hydrocarbon systems. All of these partial energies are function of the bond order between pairs of atoms, that is empirically calculated from the interatomic distance [90, 91]. The shielded Coulomb potential $E_{Coulomb}$ is calculated by the electronegativity equalization method (EEM) [92] similar to the charge equilibration (QEq) method, proposed by Rappe and Goddard [93], that allows

the charges to adjust with regard to changes in their surrounding. This method minimizes the electrostatic energy of system from the ionization potential, electron affinities and atomic radii. The total electrostatic energy is integrated from the following system of equations, including a zeroed total charge condition and the electronegativity equalization principle:

$$\frac{\partial E_q}{\partial q_1} = \chi_1 + 2q_1\eta_1 + C \cdot \sum_{i=1}^{n} \frac{q_i}{\left(r_{1,i}^3 + \left(\frac{1}{\gamma_{1,i}}\right)^3\right)^{1/3}}$$

$$\vdots \tag{2.47}$$

$$\frac{\partial E_q}{\partial q_n} = \chi_n + 2q_n\eta_n + C \cdot \sum_{i=1}^{n} \frac{q_i}{\left(r_{n,i}^3 + \left(\frac{1}{\gamma_{n,i}}\right)^3\right)^{1/3}}$$

$$\sum_{i=1}^{n} q_i = 0 \tag{2.48}$$

$$\chi_1 = \ldots = \chi_i = \ldots = \chi_n \tag{2.49}$$

where n is the atom number, χ_i are atom electronegativities, η_i are atom hardness, $\gamma_{i,j}$ are shielding parameters between atom pairs, $r_{i,j}$ are interatomic distances, q_i are atom charges.

In the case of tricalcium silicate hydration reaction, the ReaxFF reactive FF application is particularly justified by its capability to model: 1) the water dissociation and hydroxyl formation at the surface, 2) the portlandite $Ca(OH)_2$ precipitation, 3) the proton hopping phenomenon, which refers to the diffusion of hydrogen cation into the solid, interfering in the interactions between Ca^{2+} cations and silicates, and leading to the diffusion of Ca^{2+} in the opposite direction [14, 70]. In 2015, investigations on hydration mechanisms of C_2S and C_3S, using ReaxFF and a combination of two sets of parameters for Ca-O-H [59] and Si-O-H [94] reproduced unit cell parameters and elastic properties in good agreement with experimental and DFT values [14, 63]. Surface energies were calculated, and adsorption energy surface (AES) were built permitting to compute the water dissociation energy barrier in the most energetically favorable adsorption location. The dynamics allows to show the water dissociation at the surface and the dissolution of Ca^{2+} cations. A water tessellation phenomena was observed in (001) surface of C_3S. Static properties did not show any correlation in both case, and are counter intuitive in the case of C_2S where most reactive, β polymorph, exhibits lowest cleav-

age and adsorption energies than γ polymorph. Manzano et al. conclude that static properties cannot predict early hydration mechanisms and that dynamics are necessary to understand the reactions occurring during this process [14]. Despite its ability to capture bond breaks occurring during the hydration process such as dissociation of water, protonation of superficial anions, as well as the proton hopping phenomenon [14], ReaxFF is limited by its computational cost and its charge equilibration method. This method has been improved to correct unrealistic charge-transfer issues, but has not been implemented in the Ca-Si-O-H description yet [70, 91].

Chapter 3

Mechanical, thermal, and surface properties of tricalcium silicate

As a matter of fact, even at high water/cement ratio (w/c), the total hydration of Portland Cement is never achieved. Previous quantitative X-ray diffraction analyses estimated at about 85 % the amount of hydrated alite after 65 days [95] for $w/c = 0.45$. The hydration degree of cement paste obtained by deconvolution technique applied to nanoindentation experiments reached 90 % at $w/c = 0.4$ [96]. The computation of thermal and mechanical properties can thus provides important information and be helpful in the context of a multiscale modelling. Furthermore, from the computation of surface energies, the shape of C_3S grains can be theoretically constructed for different polymorphs. Determination of such properties by experimental methods are most of the time limited, especially in the case of surface energies [97]. In all cases, a proper synthesis procedure of pure C_3S is necessary, and the determination of the amount of each polymorph in a sample is neither trivial nor accurate.

The atomistic systems investigated in this thesis were built from the pure M_1 [36] and M_3 [34] crystal structures (Figure 3.1). While the later has already been used [14, 64, 98], this is the first time that a M_1 C_3S model is employed in atomistic simulations. The b parameters of these two cells are equivalent, as well as the c parameter of the M_1 model, and the a parameter of the M_3 model. Also, the two models are shifted by 1/4 in cell units in the (010) direction, meaning that the (010) plane of the M_1 model corresponds to the (040) plane of M_3 model. The a parameter of the M_1 unit cell is approximately 3 times larger than the c parameter for M_3,

and the two unit cells differ mainly by their structure in these two directions (namely (100) for M_1 and (001) for M_3).

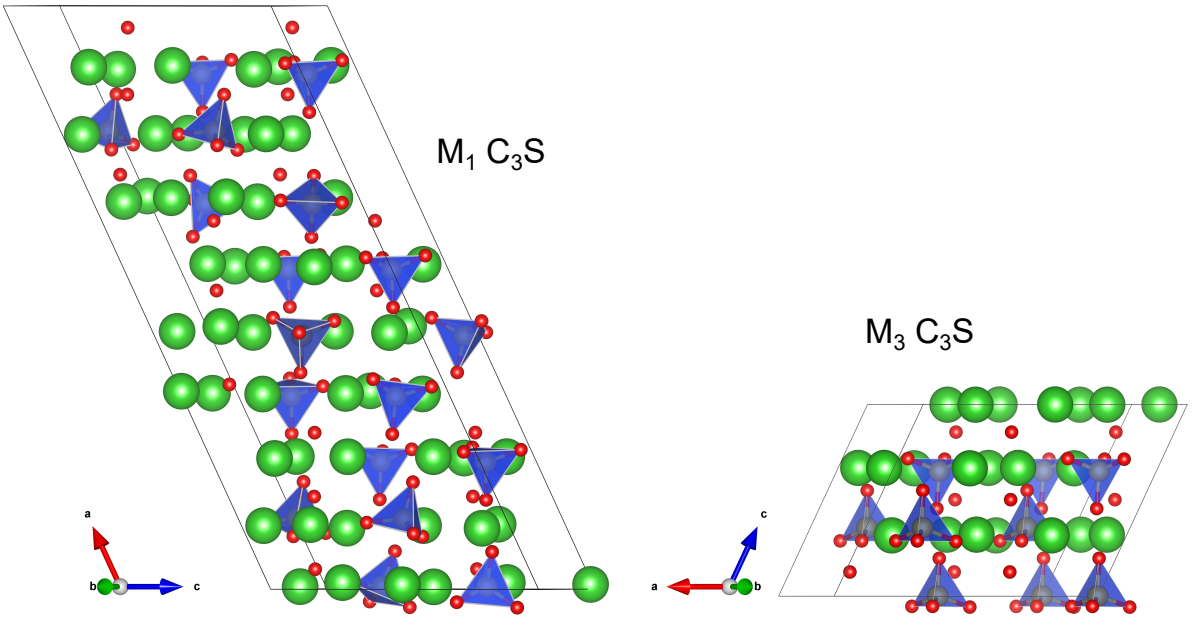

Figure 3.1. Unit cells of M_1 C_3S (cell parameters: a = 27.874 Å, b = 7.059 Å, c = 12.257 Å, β = 116.03°) [36] and M_3 C_3S (cell parameters: a = 12.235 Å, b = 7.073 Å, c = 9.298 Å, β = 116.31°) [34]. Color code: calcium cations in green, oxygen anions and silicate oxygen in red, silicon atoms in yellow, and silicate polyhedra in blue.

3.1 Elastic properties

Understanding the mechanical properties of C_3S is important for two reasons: 1) as mentioned above, the total hydration of a cement paste is never achieved so clinker components are to some extent, involved in the final microstructure of hydrated cement, 2) such properties are important to understand and optimize the grinding of clinker. The investigation of elastic properties of cementitious materials are most of the time related to hydrated products and very few data can be found in the literature concerning elastic properties of clinker components. Synthetic alite can be made by solid state sintering of decarbonated calcium oxide and fine silica, with possible addition of impurities (alumina, magnesium, sulfates), depending on the reached polymorph [99]. The elastic properties are typically determined by nanoindentation experiments and at the macroscale by resonance frequency measurements [100, 101]. Nanoindentation experiments are most of the time performed on hydrated mortar or cement

paste [96, 102, 103], and more rarely on pure and doped clinker phases [100]. Unhydrated clinker phases are known to exhibit stiffnesses by 3 to 5 times larger and hardnesses by one order of magnitude larger than hydrated phases [96, 100, 104].

According to the generalized Hooke's law, the elastic properties of anisotropic materials can be derived by the relation between the components of the stress and strain tensors σ_{ij} and ε_{kl}:

$$\sigma_{ij} = \sum_{k=1}^{3} \sum_{l=1}^{3} C_{ijkl} \varepsilon_{kl} \tag{3.1}$$

where C_{ijkl} are the 81 components of the stiffness tensor. The minor and major symmetries of the stiffness tensor allows to reduce the number of stiffness constants to 21 for a general anisotropic material:

$$\begin{bmatrix} \sigma_{11} \\ \sigma_{22} \\ \sigma_{33} \\ \sigma_{23} \\ \sigma_{13} \\ \sigma_{12} \end{bmatrix} = \begin{bmatrix} C_{1111} & C_{1122} & C_{1133} & C_{1123} & C_{1113} & C_{1112} \\ & C_{2222} & C_{2233} & C_{2223} & C_{2213} & C_{2212} \\ & & C_{3333} & C_{3323} & C_{3313} & C_{3312} \\ & & & C_{2323} & C_{2313} & C_{2312} \\ & symm. & & & C_{2313} & C_{1312} \\ & & & & & C_{1212} \end{bmatrix} \begin{bmatrix} \varepsilon_{11} \\ \varepsilon_{22} \\ \varepsilon_{33} \\ \gamma_{12} \\ \gamma_{13} \\ \gamma_{23} \end{bmatrix} \tag{3.2}$$

The more suitable Voigt notation divides the number of indices of stiffness constants by two and the number of components is reduced to 13 for a monoclinic crystal:

$$\begin{bmatrix} \sigma_{11} \\ \sigma_{22} \\ \sigma_{33} \\ \sigma_{44} \\ \sigma_{55} \\ \sigma_{66} \end{bmatrix} = \begin{bmatrix} C_{11} & C_{12} & C_{13} & 0 & C_{15} & 0 \\ C_{12} & C_{22} & C_{23} & 0 & C_{25} & 0 \\ C_{13} & C_{23} & C_{33} & 0 & C_{35} & 0 \\ 0 & 0 & 0 & C_{44} & 0 & C_{46} \\ C_{15} & C_{25} & C_{35} & 0 & C_{55} & 0 \\ 0 & 0 & 0 & C_{46} & 0 & C_{66} \end{bmatrix} \begin{bmatrix} \varepsilon_{11} \\ \varepsilon_{22} \\ \varepsilon_{33} \\ \gamma_{12} \\ \gamma_{13} \\ \gamma_{23} \end{bmatrix} \tag{3.3}$$

The elastic constant C_{ij} can be expressed as the derivative of the stress components σ_{ij} with respect to the strain components ε_{ij} and related to the strain energy $\mathcal{U}$:

$$C_{ij} = \frac{\partial \sigma_{ij}}{\partial \varepsilon_{kl}} = \frac{\partial^2 \mathcal{U}}{\partial \varepsilon_{ij} \partial \varepsilon_{kl}} \tag{3.4}$$

The elastic moduli E_i along the different directions can be derived from the compliance tensor, defined as $\mathrm{S}_{ij} = \mathrm{C}_{ij}^{-1}$, and $E_i = S_{ii}^{-1}$.

Elastic properties of solids are generally computed by applying a strain or a stress on the solid in the desired directions and by determining the strain-stress or strain-energy relations. At the atomic scale, these methods can be divided into two groups: static optimization methods and time integration methods.

Optimization methods are typically applied at 0 K, or where anharmonical vibrations can be neglected, although lattice vibration frequency can be included through quasi-harmonic approximation techniques [105]. In the so-called static method, a small strain $\Delta\varepsilon_j$ is applied positively and negatively in each direction j:

$$\begin{aligned} C_{ij}^{+} &= -\frac{\sigma_i(\Delta\varepsilon_j) - \sigma_i(0)}{\Delta\varepsilon_j} \\ C_{ij}^{-} &= \frac{\sigma_i(-\Delta\varepsilon_j) - \sigma_i(0)}{\Delta\varepsilon_j} \end{aligned} \tag{3.5}$$

The stiffness constant values can be obtained by averaging C_{ij}^{+} and C_{ij}^{-} and the symmetric constants:

$$C_{ij} = \frac{C_{ij}^{+} + C_{ij}^{-} + C_{ji}^{+} + C_{ji}^{-}}{4} \tag{3.6}$$

This method performs quick calculation, minimizing the energy of the system before and after application of a small strain $\Delta\varepsilon$. However, it does not provide the stress-strain behavior nor give a prediction of the failure point. This computational scheme can be extended by applying a strain on several step followed by an energy minimization after each step. The stiffness constant are therefore obtained by linear regression on the desired strain range.

For a system of particles with a volume V, the stress components can be computed as the sum of the kinetic and virial terms over the N particles:

$$\sigma_{ij} = \frac{\sum_k^N m_k v_{ki} v_{kj}}{V} + \frac{\sum_k^N r_{ki} f_{kj}}{V} \tag{3.7}$$

where i and j are the directions x, y and z. m_k, r_{ki}, v_{ki} are the mass, position and velocity respectively, and f_{kj} is the force applied on the particle k. In the case of a MM optimization, the kinetic term is zero. For a stress controlled simulation, the optimization is done by minimizing the generalized enthalpy H_s, as initially proposed by Parinello and Rahman [106]:

$$H_s = U + E_{el} = U + p(V - V_0) + V_0 \,\mathrm{Tr}(\boldsymbol{\tau})\boldsymbol{\varepsilon} \tag{3.8}$$

where U is the potential energy and E_{el} is the elastic energy of the lattice, p is the hydrostatic pressure applied to the system, V and V_0 are the current and reference volume respectively,

and $\boldsymbol{\tau} = \boldsymbol{\sigma} - p$ is the deviatoric stress tensor. So the first term is the internal energy, and the second and third terms are the external isotropic and deviatoric works respectively. $\mathbf{h} = \{\mathbf{abc}\}$ is the matrix of the cell vectors $\mathbf{a}$, $\mathbf{b}$, $\mathbf{c}$, and the absolute coordinates $\mathbf{r}_i$ can be written as a function as the lattice coordinates $\mathbf{s}_i$:

$$\mathbf{r}_i = \mathbf{h}\mathbf{s}_i \tag{3.9}$$

The generalized enthalpy is function of the lattice coordinates $\mathbf{s}$ and the metric tensor $\mathbf{g} = \mathbf{h}^T\mathbf{h}$, and is minimized by solving the following system:

$$\begin{aligned} \frac{\partial H_s}{\partial s} &= \frac{\partial U}{\partial s} = 0 \\ \frac{\partial H_s}{\partial g} &= \frac{\partial U}{\partial g} + \frac{1}{2}\boldsymbol{\sigma} = 0 \end{aligned} \tag{3.10}$$

Time integration methods use equilibrium MD (EMD) or non-equilibrium (NEMD) to compute the deformation of the simulation box while controlling the stress or vice versa. In EMD, the equilibrium is made before each production run, resulting in a one point averaged result. In NEMD, the strain, or the stress, is changed continuously during the run. This is convenient because only a single run is needed, however the strain/stress rate may influence the result. The simulation can be either strain or stress controlled. In the first case, a strain rate is applied on the desired direction and with a fix stress (usually 0 GPa) on the other directions. In the second case, a stress rate is applied in one direction while keeping the others at 0 GPa. The box is thus allowed to relax in the other directions.

3.1.1 Methods

Static calculations by MM

The elastic properties of M_1 and M_3 C_3S were computed from the static MM calculation method on unit cells. The enthalpy of the cell was minimized at 0 GPa, thus allowing the cell parameters and the atoms to move freely. Then a deformation was applied in the desired direction, the energy of the system was minimized, allowing the atoms to move while fixing the cell parameters. The process was repeated in each direction, negatively and positively, to calculate the 21 components of the stiffness matrix according to the Equation (3.6). The unit cells experienced maximal deformations of ±0.2, with increments of 1×10^{-4}, but the values $C_{ij}^{\pm}$ were obtained by linear fitting on values from zero to ±0.02 deformation. The LAMMPS simulation

code runs the MM simulations [107]. A LAMMPS input was created to print the variable after each deformation and minimization step, and a Python script allowed to read the output file and compute the stiffness constants. The time duration for the calculation of the stiffness constants was 4 minutes for M_3 and 8 minutes for M_1, on 4 Intel Xeon Gold 5120 CPUs @ 2.20 GHz.

Static calculations by DFT

For M_3, the results of MM calculations were compared with DFT calculations performed with the thermo_pw code, using Quantum Espresso routines [108, 109]. This open-source code is available on https://dalcorso.github.io/thermo_pw/. The M_3 unit cell of 54 atoms was optimized, at the DFT level with the Quantum Espresso code, using the PBE exchange-correlation functional with a Grimme D2 correction for van der Waals interactions. The kinetic energy cutoffs for wave functions and charge density were 45 Ry and 405 Ry, respectively. The Monkhorst-Pack method was used for the integration of the first Brillouin zone, with a $3 \times 3 \times 3$ k-point mesh. During the optimization process, the atoms were allowed to relax. Because of the size of the M_1 unit cell (162 atoms), and because this model is non-averaged, its optimization by DFT was not possible. The time duration for the geometric optimization and the calculation of stiffness constants of the M_3 unit cell was 11h36min and 9h56min, respectively, on 24 and 48 Intel Xeon Gold 5120 CPUs @ 2.20 GHz.

Voigt-Reuss-Hill approximation

Homogeneous values of bulk and shear moduli for large crystals randomly dispersed were obtained by calculating Reuss and Voigt bounds (respectively subscript R and V). The Voigt-Reuss-Hill (or VRH) estimation for monoclinic crystals is obtained as the arithmetic average of Voigt and Reuss bounds on bulk (K_V, K_R) and shear modulus (G_V, G_R) (see Equations (3.11) and (3.12)) [110]:

$$\begin{aligned} K_V &= \frac{1}{9}[C_{11} + C_{22} + C_{33} + 2(C_{12} + C_{13} + C_{23})] \\ G_V &= \frac{1}{15}[C_{11} + C_{22} + C_{33} + 3(C_{44} + C_{55} + C_{66}) - (C_{12} + C_{13} + C_{23})] \end{aligned} \tag{3.11}$$

$$
\begin{aligned}
K_R &= \Omega[a(C_{11}+C_{22}-2C_{12})+b(2C_{12}-2C_{11}-C_{23})+c(C_{15}-2C_{25}) \\
&\quad + d(2C_{12}+2C_{23}-C_{13}-2C_{22})+2e(C_{25}-C_{15})+f]^{-1} \\
G_R &= \frac{1}{15}\{4[a(C_{11}+C_{22}+C_{12})+b(2C_{12}-C_{11}-C_{23})+c(C_{15}-2C_{15}) \\
&\quad + d(C_{22}-C_{12}-C_{23}-C_{13})+e(C_{15}-C_{25})+f]/\Omega \\
&\quad + 3[g/\Omega+(C_{44}+C_{66})/(C_{44}C_{66}-C_{46}^2)]\}^{-1} \\
a &= C_{33}C_{55}-C_{35}^2 \\
b &= C_{23}C_{55}-C_{25}C_{35} \\
c &= C_{13}C_{35}-C_{15}C_{33} \\
d &= C_{13}C_{55}-C_{15}C_{35} \\
e &= C_{13}C_{25}-C_{15}C_{23} \\
f &= C_{11}(C_{22}C_{55}-C_{25}^2)-C_{12}(C_{12}C_{55}-C_{15}C_{25}) \\
&\quad + C_{15}(C_{12}C_{25}-C_{15}C_{22})+C_{25}(C_{23}C_{35}-C_{25}C_{33}) \\
g &= C_{11}C_{22}C_{33}-C_{11}C_{23}^2-C_{22}C_{13}^2-C_{33}C_{12}^2+2C_{12}C_{13}C_{23} \\
\Omega &= 2[C_{15}C_{25}(C_{33}C_{12}-C_{13}C_{23})+C_{15}C_{35}(C_{22}C_{13}-C_{12}C_{23})+C_{25}C_{35}(C_{11}C_{23}-C_{12}C_{13})] \\
&\quad - [C_{15}^2(C_{22}C_{33}-C_{23}^2)+C_{25}^2(C_{11}C_{33}-C_{13}^2)+C_{35}^2(C_{11}C_{22}-C_{12}^2)]+gC_{55}
\end{aligned}
\tag{3.12}
$$

MD calculations

In order to determine elastic properties at finite temperature, supercells of 1296 atoms ($1\times4\times2$ $2\times4\times3$ for M_1 and M_3 C_3S respectively) were created from the unit cells presented in Figure 3.1. For each polymorph, three replicas were created by using different seeds for the initial velocities of atoms. Equilibration runs were performed during 500 ps at 300 K in the NpT ensemble at hydrostatic pressure σ varying between 0 and 15 GPa, followed by a production run of 1 ns. Nose-Hoover thermostat and barostat were employed and the Newton equation of motion was integrated with the Verlet algorithm. Long-range interaction were computed with an Ewald summation with precision of 10^{-5} and a cutoff of 10 Å was applied for van der Waals interactions.

The bulk modulus was calculated from the EMD simulation in the NpT ensemble with

incremental equilibrium pressure. It is, by definition, the factor ratio between the variation of the hydrostatic pressure, and the volume variation rate, at constant temperature:

$$K = -V_0\left(\frac{\partial P}{\partial V}\right)_T \tag{3.13}$$

In the NEMD calculation scheme, the supercells underwent 1 ns runs of compression and traction at a strain rate of 1×10^8 s^{-1} up to 20 %, the stress components were computed from Equation (3.7). No noticeable influence was reported for rates of one order of magnitude above and bellow 1×10^8 s^{-1}. This is predictable because the resulting dislocation velocity is ~0.28 m s^{-1} for the largest dimension. This dislocation velocity is large when compared to macroscale tests, but is negligible compared to the velocity of acoustic waves in C_3S. Based on the values of bulk modulus K, Poisson's ratio ν and density ρ from previous acoustic measurements [111], compressive and shear waves are calculated as 7200 and 3700 m s^{-1} respectively. This ensures that atoms will respond instantaneously to the deformation of the simulation box [112, 113]. For both EMD and NEMD simulations, a Python script allowed to extract data from the LAMMPS log file and to compute the elastic constants. These were calculated by the direct relations, where $i \neq j$ are the x, y and z coordinates:

$$\begin{aligned} E_{ii} &= \frac{\sigma_{ii}}{\varepsilon_{ii}} \\ G_{ij} &= \frac{\sigma_{ij}}{\varepsilon_{ij}} \\ \nu_{ij} &= -\frac{\varepsilon_{ii}}{\varepsilon_{jj}} \end{aligned} \tag{3.14}$$

The total calculation of the elastic constants was 45 hours and 42 minutes for both M_1 and M_3 supercells, on 24 Intel Xeon Gold 5120 CPUs @ 2.20 GHz.

3.1.2 Results

The stiffness constants, homogenized elastic constants and directional elastic moduli of M_1 and M_3 C_3S, computed by DFT and static MM method are reported in Table 3.1 and Table 3.2 respectively. It stands out that the stiffness and homogenized elastic constants obtained by DFT are larger than values from MD calculation. Velez et al. measured elastic moduli of 147 ± 5 GPa and 135 ± 7 GPa by resonance frequency and nanoindentation respectively [100]. Boumiz et al. found $K = 105.2 \pm 0.5$ GPa, $G = 44.8 \pm 0.6$ GPa, $E = 117.6 \pm 0.8$ GPa and $\nu = 0.314 \pm 0.017$

	IFF	ClayFF
C_{11}	185.2(2)	89.3(2)
C_{12}	62.11(9)	29.6(4)
C_{13}	61.73(8)	27.83(7)
C_{15}	17.35(3)	−0.12(7)
C_{22}	216.1(3)	112.6(5)
C_{23}	70.77(9)	33.31(8)
C_{25}	−8.38(2)	−4.7(3)
C_{33}	212.7(3)	100.2(3)
C_{35}	−9.2(3)	−7.93(3)
C_{44}	66.54(3)	34.93(4)
C_{46}	−4.954(7)	−3.958(8)
C_{55}	66.44(3)	31.35(4)
C_{66}	65.17(3)	32.21(4)
K	111.1	53.2
G	66.7	33.5
E	166.8	83.0
ν	0.250	0.240
E_{11}	151.5	77.2
E_{22}	180.6	96.2
E_{33}	177.3	84.4
E_{44}	66.2	34.4
E_{55}	63.1	30.6
E_{66}	64.8	31.7

Table 3.1. Stiffness constants homogenized elastic constants of M_1 C_3S in GPa.

	DFT	IFF	ClayFF	ClayFF[a] [62]	ClayFF[b] [62]	Buck.[b] [104]
C_{11}	243.23	219.6(3)	118.6(2)	100.62	109.54	
C_{12}	87.17	77.54(9)	34.81(7)	23.36	39.73	
C_{13}	69.91	52.79(7)	35.98(5)	36.73	37.85	
C_{15}	28.92	4.0(1)	17.69(4)	0	8.01	
C_{22}	280.53	216.0(3)	85.9(3)	83.24	114.82	
C_{23}	62.85	52.72(8)	27.95(8)	27.17	37.35	
C_{25}	-29.89	−21.7(9)	1.39(4)	0	7.69	
C_{33}	290.81	189.6(2)	95.4(1)	144.16	94.43	
C_{35}	-14.53	−34.04(2)	6.65(3)	0	0.26	
C_{44}	68.75	37.0(7)	33.01(5)	26.95	32.24	
C_{46}	-28.25	−6.39(8)	3.28(5)	0	4.54	
C_{55}	79.04	43.4(6)	38.22(4)	30.19	34.17	
C_{66}	95.59	67.65(7)	32.16(6)	37.19	32.90	
K	139.1	104.7	53.9	53.88	60.30	103.0
G	82.2	54.3	33.5	33.97	33.07	54.5
E	206.1	139.0	83.2	95.94	84.99	138.9
ν	0.253	0.279	0.243			0.28
E_{11}	186.2	176.9	91.2			
E_{22}	225.4	174.6	71.7			
E_{33}	260.9	147.2	80.4			
E_{44}	60.4	36.3	32.7			
E_{55}	68.0	34.9	35.3			
E_{66}	84.0	66.5	31.8			

Table 3.2. Stiffness constants and homogenized elastic constants of M_3 C_3S in GPa. [a]Calculated on the same M_3 model by Mumme [34]. [b]Calculated on the M_3 model proposed by de la Torre [35].

by acoustic measurements [111]. The values obtained with INTERFACE FF (IFF) agree relatively well with these experimental measurements. When compared to experimental results, the ClayFF tends to underestimate by a factor of approximately 2 the stiffness constants and thus the elastic constants. The values obtained with this force field are closed to previous calculations on the same M_3 unit cell, obtained with the GULP code, via second derivative of the binding energy [62] (see Table 3.2). Employing the same code and computational method, the Young moduli, shear moduli, bulk moduli and Poisson's ratio were determined on the M_3 C_3S model proposed by de la Torre et al. [35], using a Buckingham force field [104] and ClayFF [62]. The homogenized elastic constants obtained by IFF are very closed to those obtained by Manzano et al. with the Buckingham FF [104]. Homogenized K, G and E are larger for M_1 than for M_3. The lowest elastic modulus is obtained in the x and z direction for the M_1 and M_3 polymorph respectively. This result is predictable because of the correspondence of the c parameter of the M_1 unit cell with the a parameter of the M_3 unit cell.

The distributions of elastic moduli in space were created from the ELATE open-source Python module [114]. The resulting shapes are illustrated in Figure 3.2 and Figure 3.3 for M_1 and M_3 C_3S respectively. The M_3 polymorph reveals a much more anisotropic elasticity than

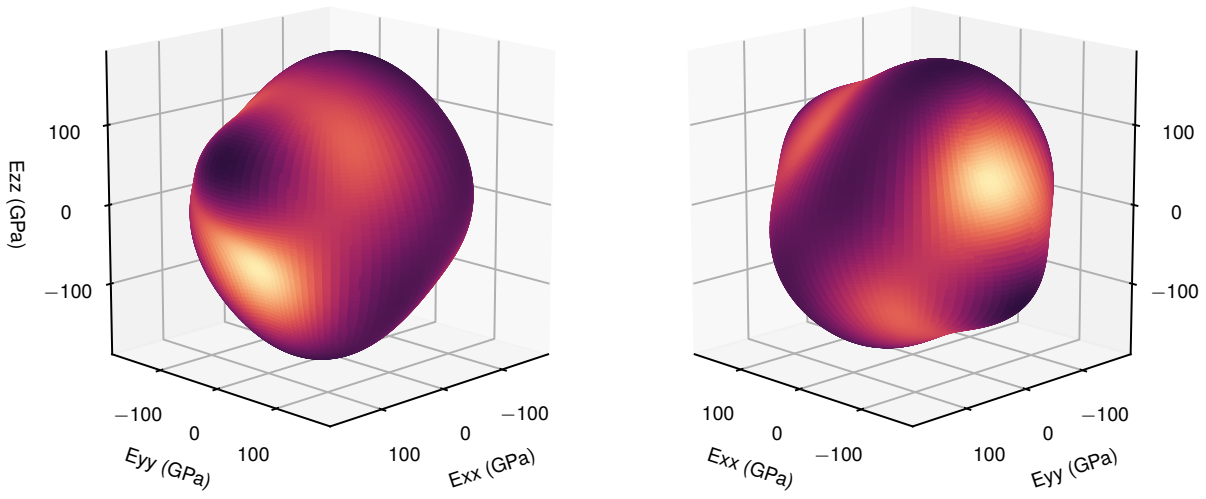

Figure 3.2. Distribution of elastic moduli in space for the M_1 C_3S, computed with IFF.

the M_1 polymorph. The strain obtained in the x, y and z direction, as well as the relative variation of volume, as a function of the hydrostatic pressure are presented in Figure 3.4. The stress-strain behavior of M_1 and M_3 are inverted in the x and z direction, due to the

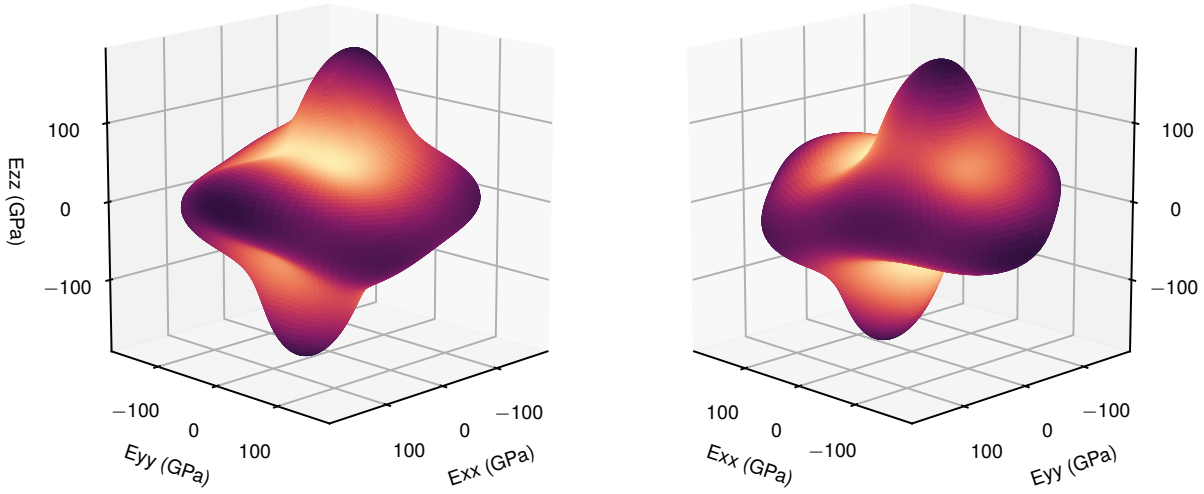

Figure 3.3. Distribution of elastic moduli in space for the M_3 C_3S, computed with IFF.

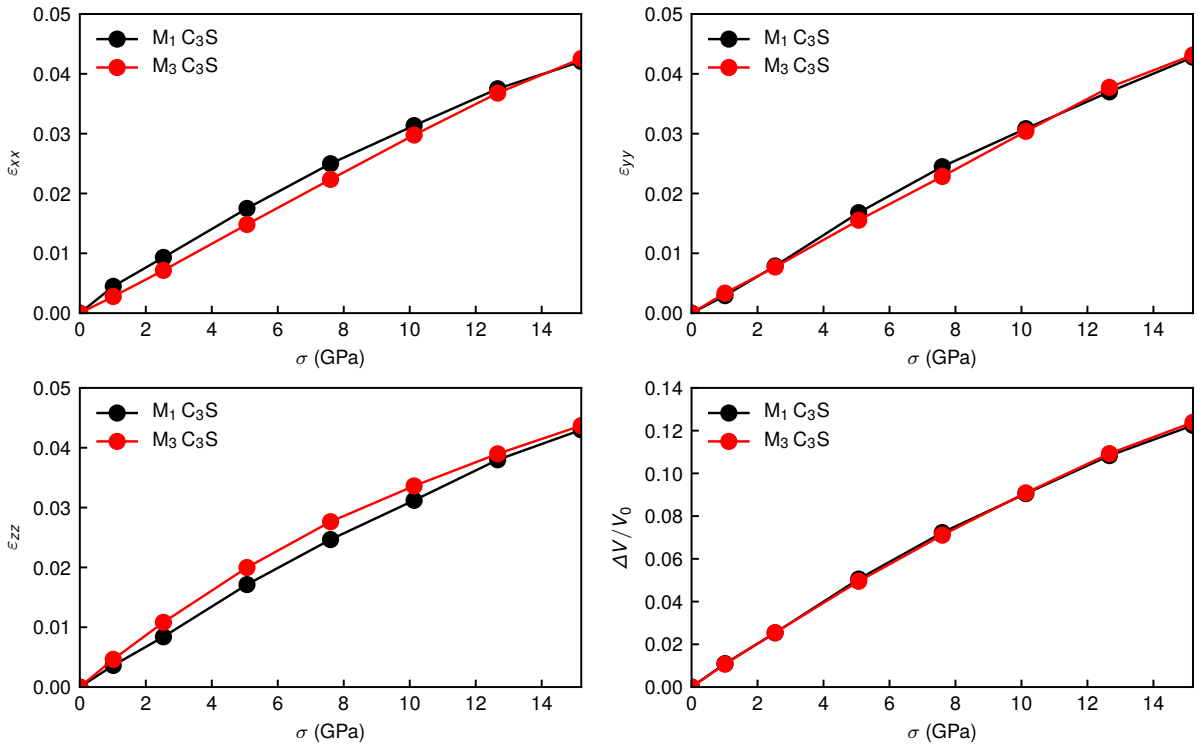

Figure 3.4. Strain and volume variation as function of the hydrostatic pressure.

correspondence of the c parameter of the M_1 unit cell with the a parameter of the M_3 unit cell. The bulk moduli obtained by linear fitting up to 5 GPa are 101 ± 2 GPa and 103 ± 2 GPa for the M_1 and M_3 C_3S respectively.

The radial distribution function (RDF), denoted $g(r)$, is a measure of the probability of finding two atoms at a distance r from each other. This parameter is recurrent in MD trajectory analysis, including in other systems [115–118]. Its mathematical expression can be written as follows:

$$g(r) = \lim_{\mathrm{d}r \to \infty} \frac{p(r)}{4\pi(N/V)r^2\mathrm{d}r} \tag{3.15}$$

where $p(r)$ is the average number of atom pairs measured at a distance between r and $r + \mathrm{d}r$ from each others, N is the number of pairs of atoms, V is the total volume of the system. The g(r) plugin implemented in the VMD program does not account for boxes whose dimensions vary during the simulation. Here, a Python script, using the MDAnalysis library was used to compute the RDF. As an important feature of the C_3S, the coordination of calcium cations Ca with the oxygen of silicates Os was analyzed by radial distribution function with variation of the hydrostatic pressure (see Figure 3.5). The increasing hydrostatic pressure seems to

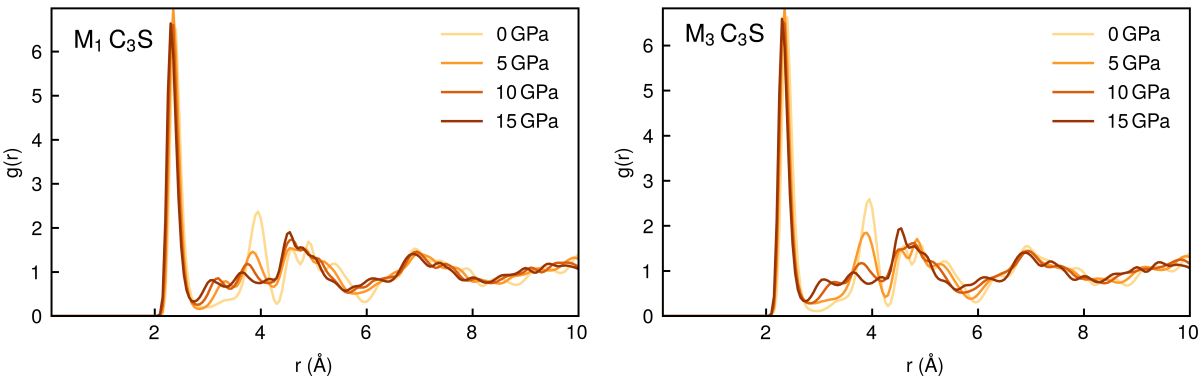

Figure 3.5. Radial distribution function of Ca-Os pairs as a function of the hydrostatic pressure.

influence the structure at short range (~4 Å). The second coordination shell peak of Ca-Os pairs is shifted to the left and is flattened by the effect of the pressure. The same behavior is observed for both polymorphs.

Next, the stress-strain curves of the NEMD simulations, and of the static MM calculation are plotted in Figure 3.6. The general behavior of the M_1 and M_3 polymorphs seems similar. However, the yield stress in compression seems to be larger for the M_1 polymorph in the x direction, and for the M_3 polymorph in the z direction. In fact, the c parameter of the M_1 unit

cell corresponds to the *a* parameter of the M_3 unit cell, which explains this result. The elastic moduli and Poisson's ratios obtained from these NEMD simulation are presented in Table 3.3. They are relatively closed to values from previous stress controlled NEMD simulations [64].

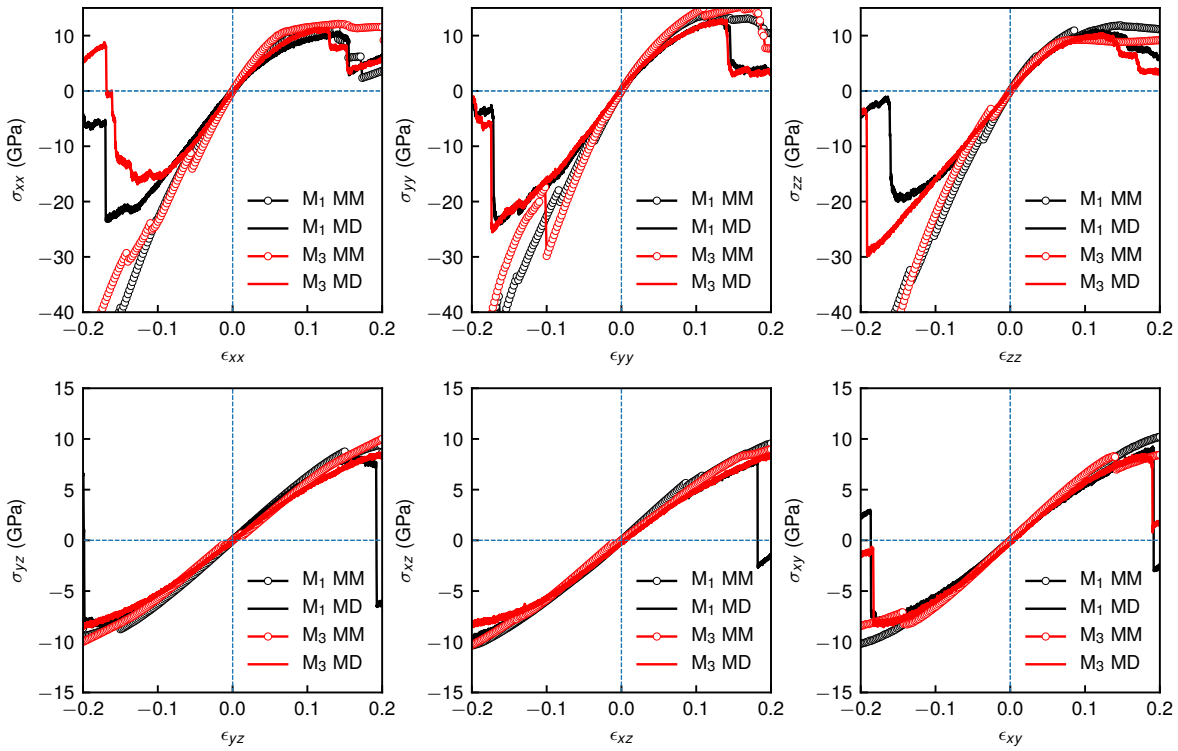

Figure 3.6. Stress-strain curves of NEMD simulations and static MM calculation with IFF.

	M_1	M_3	$M_3{}^a$ [64]
$E_{11} = E_{xx}$	141.8(2)	168.5(2)	152(6)
$E_{22} = E_{yy}$	164.4(2)	166.0(2)	176(3)
$E_{33} = E_{zz}$	155.8(2)	154.9(1)	103(11)
$E_{44} = G_{yz}$	62.6(5)	57.16(6)	
$E_{55} = G_{xz}$	59.22(7)	57.42(6)	
$E_{66} = G_{xy}$	59.77(5)	64.35(6)	
$\nu_{12} = \nu_{xy}$	0.220(1)	0.297(1)	0.303(42)
$\nu_{13} = \nu_{xz}$	0.236(2)	0.227(2)	0.273(43)
$\nu_{21} = \nu_{yx}$	0.241(2)	0.290(1)	0.225(21)
$\nu_{23} = \nu_{yz}$	0.239(2)	0.215(1)	0.197(27)
$\nu_{31} = \nu_{zx}$	0.245(2)	0.200(1)	0.372(41)
$\nu_{32} = \nu_{zy}$	0.230(1)	0.200(1)	0.299(58)

Table 3.3. Elastic moduli and Poisson's ratio obtained from NEMD simulations with IFF. ^{a}Results from previous stress controlled NEMD.

3.2 Thermal properties

During their lifetime, concrete volumes undergo temperature changes. The thermal expansion and contraction of concrete as temperature increases and decreases, respectively, is influenced by the aggregate type, but also by the cement type, and the water cement ratio. As explained in the introduction of this chapter, the complete hydration of cement is never reached. Thus, although the aggregate type has the larger influence on the expansion and contraction of concrete, the thermal properties of hydrated and dry cement is of great interest. Thermal cracking of concrete generally occurs during the first days after casting. During the exothermic hydration of cement, the temperature rises, and drops faster on the surface than in the bulk. The surface tends to contract with the cooling and stress arises because the bulk remains hotter, resulting in cracks. Naturally, this phenomena occurs to greater extent in larger volumes, called *mass concrete*. When a material is heated, its internal energy increases. Considering a system of fixed volume being heated, the heat capacity is the partial derivative of its internal energy

with respect to its temperature:

$$C_V = \left(\frac{\partial E}{\partial T}\right)_V \tag{3.16}$$

In practice, heat transfer can be measured with a calorimeter. Heat capacity of gases can be determine experimentally at constant volume. However, because of a lower compressibility, the internal energy of a liquid or a solid experience large variation with volume. For this reason, the heat capacity of a solid is, most of the time, experimentally determined at constant pressure. When the system is free to change its volume, some of the energy is consumed in the expansion work [119]. The heat capacity is thus defined as the partial derivative of enthalpy with respect to temperature:

$$C_p = \left(\frac{\partial H}{\partial T}\right)_p \tag{3.17}$$

Two methods are commonly used to compute the specific heat from a molecular dynamics simulation. In the canonical ensemble, one can derive the fluctuation relationship between specific heat and internal energy as follows:

$$C_V = \frac{\partial E}{\partial T} = \frac{\partial E}{\partial \beta}\frac{\partial \beta}{\partial T} \tag{3.18}$$

with $\beta = 1/k_B T$, where k_B is the Boltzmann constant. As derived in Chapter 2, the relation between the average energy of the system and the partition function Q is $E = -\partial \ln Q/\partial \beta$. Therefore:

$$\begin{aligned} C_V &= \frac{\beta}{T}\frac{\partial^2 \ln Q}{\partial \beta^2} \\ &= \frac{\beta}{T}\frac{\partial}{\partial x}\left(\frac{1}{Q}\frac{\partial Q}{\partial \beta}\right) \\ &= \frac{\beta}{T}\left[\frac{1}{Q}\frac{\partial^2 Q}{\partial \beta^2} - \frac{1}{Q^2}\left(\frac{\partial Q}{\partial \beta}\right)^2\right] \\ &= \frac{1}{k_B T^2}(\langle E^2\rangle - \langle E\rangle^2) = \frac{1}{k_B T^2}\left\langle (\Delta E)^2\right\rangle \end{aligned} \tag{3.19}$$

The specific heat capacity (also called specific heat) is an intensive property, which is defined as the heat capacity by amount of substance. From thermodynamical laws, the specific heat capacities c_v and c_p at constant volume and pressure, respectively, are related by the equation:

$$c_p - c_v = T\frac{\alpha^2}{\rho \beta} \tag{3.20}$$

where ρ is the density, $\alpha = (1/V)(\partial V/\partial T)_p$ is the thermal expansion coefficient, and $\beta = -(1/V)(\partial V/\partial P)_T$ is the compressibility, inverse of the bulk modulus K.

3.3 Methods

Fluctuation relations are well-established for all ensembles. By using fluctuation methods, the specific heat can be computed at any temperature with a single, long enough run. However, these methods rely strongly on the temperature relaxation parameter used to thermostat the system (and in the case of the NpT ensemble, on the pressure relaxation parameter) [120]. Moreover values obtained by fluctuation method depends on the time interval used for block averages [120], often leads to large uncertainties and to bad agreements with experimental results [121]. For this reason, the non-fluctuation, or direct method, is a more robust method. It consists on running several simulations at finite temperature and calculating the time average energies for each one. The specific heat is calculated by definition, as the slope of the total energy with respect to the temperature, at the desired temperature. Most of the time, by linear fitting of $\Delta E/\Delta T$. The chosen ΔT must be large enough to compute accurately the variation of energy between each systems, but small enough, for the linear fitting to be representative.

The specific heat capacity can also be computed from the velocity autocorrelation function (VACF) of atoms. The phonon is the quasi-particle resulting from the vibration of a crystalline solid. Considering a solid made by quantum harmonic oscillator, the phonon density of states $g(\omega)$ is proportional to the Fourrier transform of the velocity autocorrelation function of the atoms:

$$g(\omega) = \frac{1}{3NkT} \int_{-\infty}^{+\infty} \sum_{i=1}^{N} \langle \mathbf{v}_i(t) \cdot \mathbf{v}_i(0) \rangle \, e^{i\omega t} \mathrm{d}t \tag{3.21}$$

where k is the Boltzmann constant, N is the number of atoms and T is the temperature of the system. The occupational states of phonons follows a Bose-Einstein distribution f_{BE} and at energy largely below the Debye temperature, the total energy of the system can be reduced to the vibrational energy E_v [119, 122]:

$$E_v = \int_0^{+\infty} \hbar\omega \left(g(\omega) f_{BE}(\omega) + \frac{1}{2} \right) \mathrm{d}\omega \tag{3.22}$$

The specific heat in $3Nk$ units is calculated from Equation (3.16), as follows:

$$c_v = \frac{\int_0^{+\infty} \frac{u^2 e^u}{(1-e^u)^2} g(\omega) \mathrm{d}\omega}{\int_0^{+\infty} g(\omega) \mathrm{d}\omega} \tag{3.23}$$

where $u = \hbar\omega/kT$.

The specific heat and expansion coefficient were computed on three replicas of 1296 atoms supercells. The simulations were performed in the NpT ensemble with the same MD parameters as previously. The systems were relaxed during 0.5 ns, and the data were collected for 1 ns. Within the direct method, the specific heat c_p was computed by linear fitting of the enthalpy with respect to the temperature at five points around the temperature of interest (e.g., 280, 290, 300, 310 and 320 K to compute the specific heat at 300 K). The extraction of data from LAMMPS log files and the calculation were performed by a Python script. The same method was employed to calculate the expansion coefficient, fitting the volume variation with respect to the temperature. To compute c_v as function of the VACF with no external influence of thermostating or barostating, the relaxed system were equilibrated for 500 ps in the NVE ensemble, before running simulation of 100 ps, dumping the trajectory at each time step to be able to observe high vibrational frequencies. For the calculation using the ClayFF, a geometric mixing rule for LJ parameters was used. Indeed, this mixing rule provides more accurate value of density obtained during NpT simulations. The VACF were computed on ten correlation windows of 10 ps on three replica for each polymorph. The reading of velocities and calculation of VACF, DOS and c_v where performed with the LAMMPS Plugins for Thermal Conductivity provided freely by the MAGICS center of the University of Southern California on http://magics.usc.edu/software-downloads/. The code was modified to increase the number of atom types. The constant pressure specific heat c_p was calculated from Equation (3.20) to compare with experimental values.

3.4 Results

The lattice parameters obtained in our simulations are in good agreement with experimental values (see Table 3.4). The density obtained with IFF are slightly lower than experimental measurements and results from previous computational studies. This is probably due to the cutoff, and the accuracy chosen for the computation of short and long range interactions. DFT optimization with Grimme's D2 correction tends to increase the unit cell volume, though less than without vdW correction. Previously reported DFT optimization showed a similar behavior, although less pronounced [17, 123]. The β parameters obtained by DFT and MD calculations are slightly smaller than experimental values.

	Method	a (Å)	b (Å)	c (Å)	β (°)	ρ (g cm^{-3})
M_1	Exp.	27.874	7.059	12.257	116.31	3.149
	IFF	27.982(36)	7.051(8)	12.216(15)	115.88(12)	3.147(5)
M_3	Exp.	12.235	7.073	9.298	116.03	3.154
	IFF	12.218(15)	7.056(8)	9.342(12)	115.88(12)	3.139(5)
	IFF [64]	12.215	7.043	9.343	116.18	3.15
	ReaxFF [14]	12.17	7.08	9.33	116.18	3.15
	DFT	12.380	7.151	9.570	115.45	2.973
	DFT (Grimme-D2)	12.278	7.095	9.458	115.57	3.061
	DFT [17, 123]	12.46	7.20	9.38	116.23	3.014

Table 3.4. Lattice parameters of M_1 and M_3 C_3S, from EMD and DFT calculations.

The high uncertainty is due to large variations of pressure and volume in the NpT ensemble. These variations can be reduced by increasing the size of the system, the number of sample, or by changing the damping parameter for the control of pressure. The values obtained are closed to previously computed values with the CSH force field [122]. The compressibility is calculated as the inverse of the bulk modulus, previously computed by EMD simulation. At 300 K, the difference between c_p and c_v was calculated from the Equation (3.20) as 1.2×10^{-2} and 1.3×10^{-2} J g^{-1} K, for the M_1 and M_3 C_3S, respectively, in good agreement with Qomi et al. [122]. The phonon density of states (DOS) obtained from simulations in the NVE ensemble are presented in Figure 3.7 for the IFF, and Figure 3.8.

The phonon DOS obtained for M_1 and M_3 are almost identical, so as the resulting specific heat. Thus the structural difference between both polymorph does not influence the thermal properties of the polymorph. However, the force field does affect the results. The main difference between the phonon DOS obtained with IFF and ClayFF relies principally in their description of bonds in silicate. In the case of IFF, where Si-O bonds are described by harmonic oscillators in addition to the short and long range description, the partial DOS (PDOS) of Os and Si atoms form a sharped peak near 935 cm^{-1}, in agreement with infrared spectroscopy measurements [124], while the in-plane bending vibration of Os-Si-Os angles is measured as a band bellow 500 cm^{-1} [124]. This bending contribution happens at larger frequencies in our results (near 550 cm^{-1}). Wave numbers ω bellow 500 cm^{-1} are associated to stretching be-

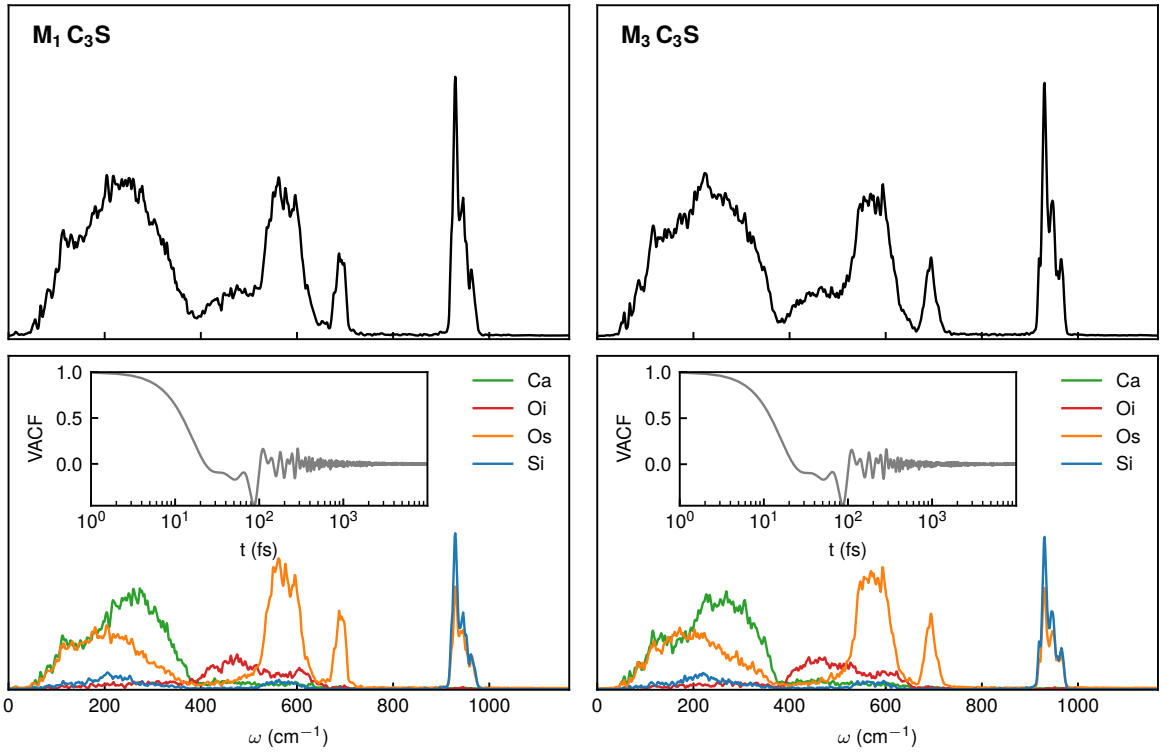

Figure 3.7. Phonon density of states with VACF in insets (top), and partial density of states (bottom) of M_1 and M_3 C_3S obtained with IFF.

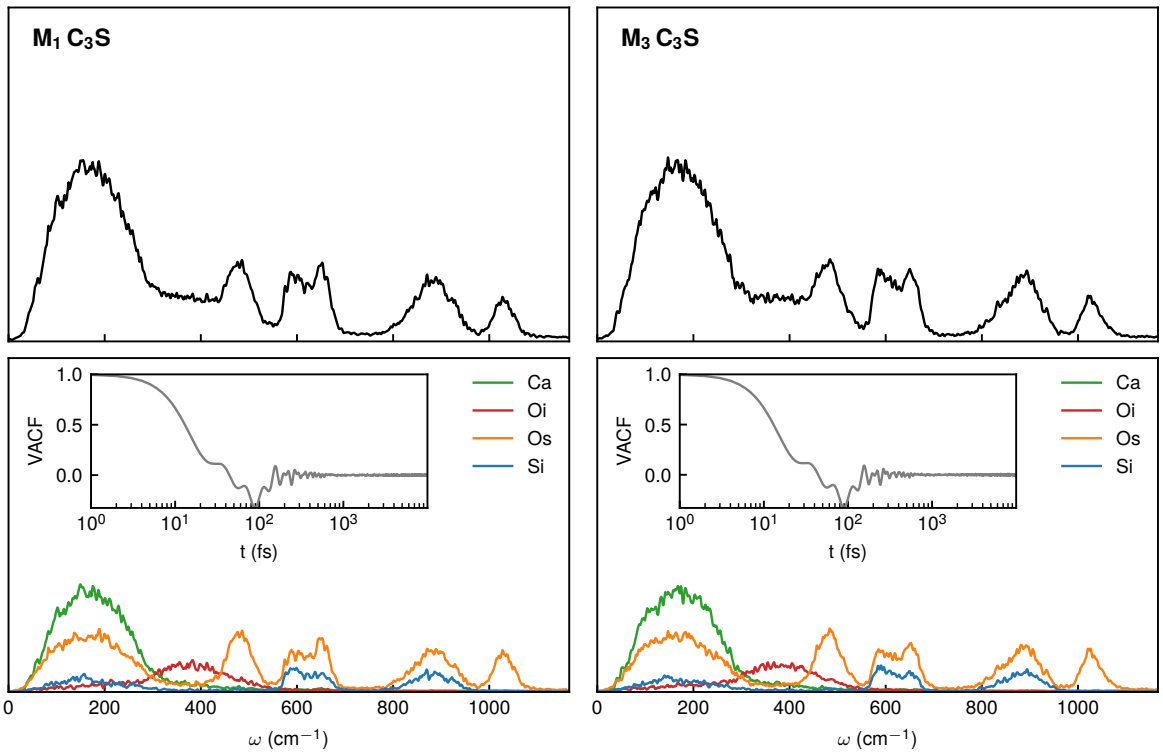

Figure 3.8. Phonon density of states with VACF in insets (top), and partial density of states (bottom) of M_1 and M_3 C_3S obtained with ClayFF.

tween calcium and oxygen atoms [122, 125], in agreement with the PDOS obtained with both IFF and ClayFF. For ClayFF, the purely non-bonded description of Si-Os bonds allows for more degrees of freedom of atoms. The PDOS obtained for Si and Os atoms are thus more sparse. Generally, for the IFF, a shift of the DOS is observed towards higher vibrational frequencies. No significant variation of the DOS was observed between 200, 300 and 400 K. The error on the calculation of the isobaric specific heat c_p are mostly related to the $c_p - c_v$ quantity, calculated from simulations in the NpT ensemble. The values of $c_p - c_v$ were calculated at 200, 300 and 400 K and extrapolated linearly, because this quantity vary proportionally with temperature (see Equation (3.20)). The expansion coefficient α, the compressibility β, and the density ρ, computed from simulations in the NpT ensemble are presented in Table 3.5.

	Temperature (K)	α (K^{-1})	β (Pa^{-1})	ρ ($g\,cm^{-3}$)	$c_p - c_v$ ($J\,g^{-1}\,K$)
M_1	200	$4.6(18) \times 10^{-5}$	$9.9(2) \times 10^{-12}$	3.147(5)	0.013(14)
	300	$4.4(15) \times 10^{-5}$	$9.7(3) \times 10^{-12}$	3.160(4)	0.019(13)
	400	$5.0(23) \times 10^{-5}$	$10.0(2) \times 10^{-12}$	3.147(6)	0.032(30)
M_3	200	$3.6(14) \times 10^{-5}$	$9.7(2) \times 10^{-12}$	3.139(5)	0.009(8)
	300	$4.0(16) \times 10^{-5}$	$9.7(3) \times 10^{-12}$	3.151(4)	0.016(13)
	400	$4.8(15) \times 10^{-5}$	$9.5(2) \times 10^{-12}$	3.128(6)	0.031(21)

Table 3.5. Lattice parameters of M_1 and M_3 C_3S, from EMD and DFT calculations.

The specific heat c_p obtained for M_1 and M_3 C_3S are plotted with respect to the temperature in Figure 3.9. The values obtained at 300 K by the direct method are 0.86 ± 0.10 and $0.87 \pm 0.04\,J\,g^{-1}\,K^{-1}$ for M_1 and M_3 C_3S respectively, which is much larger than experimental measurements. As for the phonon DOS, no significant variation of c_p was found between M_1 and M_3. The VACF method with ClayFF results in $c_p = 0.751 \pm 0.013\,J\,g^{-1}\,K^{-1}$, which is very close to experimental values of $0.756\,J\,g^{-1}\,K^{-1}$ [126] and $0.753\,J\,g^{-1}\,K^{-1}$ [127]. The IFF provided a value slightly lower than experimental measurements: $0.723 \pm 0.013\,J\,g^{-1}\,K^{-1}$.

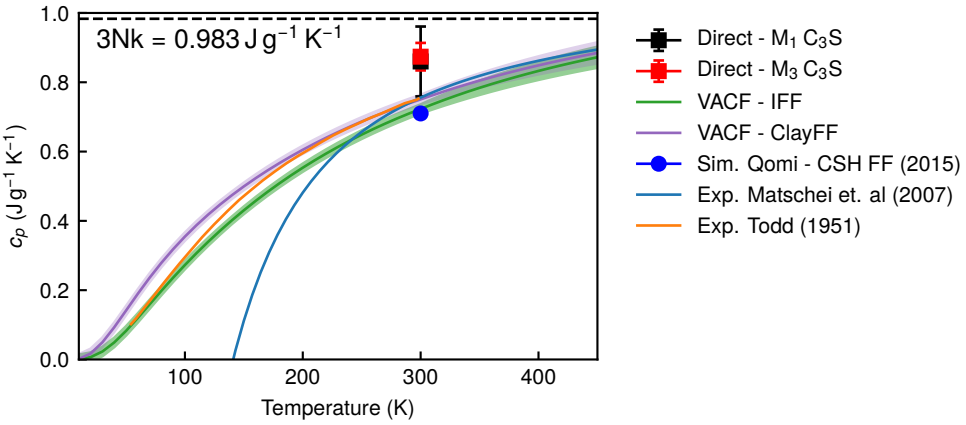

Figure 3.9. Specific heat of M_1 and M_3 C_3S obtained by the direct and VACF method, plotted as function of the temperature. The transparent areas represent the error. Previously computed value from VACF calculation, as well as fitting of experimental measurements [126] and direct measurements [127] are plotted in addition to the results.

3.5 Cleavage energies and equilibrium shapes

Surface energy is an important property of crystals since it can be an indicator of reactivity and give information on equilibrium shapes [97]. A surface can be defined by the Miller indices which give the orientation of the surface plane, and by the shift which is the displacement relatively to the unit cell origin, also corresponding to Miller indices superior to one. Charge distribution in ionic crystals can induce polar or non-polar surfaces. Tasker categorized the surface into three different types: the type 1, where the surface consists of coplanar cations and anions, resulting in a zero dipole moment; the type 2, where a sequence of cationic and anionic layers are stacking, the combination of layers hence leads to a zero dipole moment; the type 3, where the stacking sequence of charged layers lead to a non-zero dipole moment and for which all possible cleavage planes result in a polar surface [128, 129]. Type 3 surfaces cannot be stable without reconstruction, which involves the displacement of ions from the top side to the bottom side of the slab in order to maintain charge neutrality and minimize local dipole moments [64, 128, 130]. A practical way to compute the surface energy is to use three-dimensional periodicity. This method consists in creating a box composed by a slab in contact with a vacuum gap. The thickness must be sufficient so that the properties of the center of the slab converge to those of the bulk, and the vacuum region needs to be large enough, such that the surfaces do not interact through the boundaries. The cleavage energy is defined as the energy necessary to split a crystal along a specific plane. It is therefore the average of

the energies of the two surfaces created. The cleavage energy is commonly computed as the difference between the slab and the bulk energies, divided by the generated surface area:

$$E_{cleav} = \frac{E_{slab} - E_{bulk}}{2A} \tag{3.24}$$

where E_{slab} and E_{bulk} are respectively the energies of slab and bulk systems, with the same number of atoms and stoichiometry, and A is the surface area of one side of the slab. As said above, the scheme to properly compute the surface energy is to choose the vacuum length in order to nullify the interaction between periodic images. Following the same scheme, the thickness of the slab must be sufficient to reproduce bulk properties in its centre. Most of the time, the bulk energy computation by MD is performed running simulations in NpT ensemble on a supercell, with Periodic Boundary Conditions (PBC). Sun and Ceder documented some issues regarding the calculation of the bulk energy from Equation (3.24) [131]. This non-convergence arises from the difference between the converged bulk energy and the incremental increase of slab energy per layer. The authors performed surface energy computation calculating the bulk energy in different ways. The two methods which most improved the convergence were: 1) the calculation on basis transformed unit cells, eliminating inconsistencies in Brillouin zone integration, 2) the linear-fit relation introduced by Fiorentini and Methfessel [132], giving an average of the bulk energy computed over several slabs of different thickness.

$$E_{slab}(N) = 2E_{surf} + NE_{bulk} \tag{3.25}$$

where N is the number of layers forming the slab in the perpendicular direction.

Another way mostly used in MD to compute the cleavage energy, preventing from any issue related to computation of the bulk energy, is to subtract the computed energies of unified and cleaved slabs, using the following equation:

$$E_{cleav} = \frac{E_{cleaved} - E_{unified}}{2A} \tag{3.26}$$

When the surfaces computed on both sides of the slab are symmetrically equivalent, the surface energy is equal to the cleavage energy. However, for most of the minerals, such an assumption cannot be effective for all the Miller indices, and, among various existing methods, Manzano et. al [14] suggested to divide the slab in contact with a vacuum into two atomic groups and to computed the surface energy for each of them. Both groups have one side exposed to the vacuum region and the other in contact with the other group. The surface energy

of each side of the slab can be computed as follow:

$$E_{surf} = \frac{E_{slab} - E_{bulk}}{A} \tag{3.27}$$

Obviously, if the subject of the study is a reconstructed, electrically neutral slab, the surface energies computed for both subslabs are considered equals and correspond to a cleavage energy. One should note that surface energies of asymmetrical, non-reconstructed surfaces can be computed by DFT or reactive force field. However, this is not in accordance with the classical electrostatic criteria stipulated by Tasker [128, 129] and could lead to unrealistic charge distribution. In addition to redistribution of the atomic charge on the two faces of the slab, other methods such as temperature gradients can be applied to assess more energetically favorable configuration, resulting in lower cleavage energies [64, 133].

3.5.1 Methods

The selected models belongs to the *Pc* and *Cm* space group (for M_1 and M_3 C_3S respectively), and thus have a glide symmetry in the (010) direction (see Figure 3.1). In this direction, Tasker type 2 surfaces with no net dipole can be built without the need for reconstruction [14, 128]. For the other planes, in order to minimize the dipole moment at the surface, the ions of the cleaved layer were equally distributed on both side of the slab. Five unified slabs with random distribution of superficial ions were constructud for each plane. The pymatgen Python module was used to generate surfaces in each plane, and a tcl script within the VMD program allowed to create orthorhombic, cleaved and unified systems in each direction. The scripts also performed moves on superficial atoms from one side of the slab to the other, for planes needing surface reconstruction. The size of the slabs was at least 5.6 nm thickness and at least 2.4 nm in the periodic directions, with a 20 nm vacuum between periodic images. The cleaved systems were created by separating the unified slabs in two parts along the z axis by a 10 nm vacuum space. For each cleaved and unified system, a series of five steep temperature gradients (10 ps) from 10 000 K to 298 K was applied on the superficial atoms in the NVT ensemble (with a Berendsen thermostat), while the rest of the atoms remained fixed. Such a method has already been used to reach more energetically favorable configurations [64, 133], but has never been described so precisely as follows. To avoid moves between two surfaces during this process, each ion was tethered in the z direction by a 1.0 kcal $Å^{-1}$ spring force. After energy

minimization by conjugate gradient method, the final configuration with the lowest energy for the whole series is subsequently submitted to a 200 ps equilibration run and to a 300 ps production run in NVT ensemble at 298 K (see Figure 3.10).

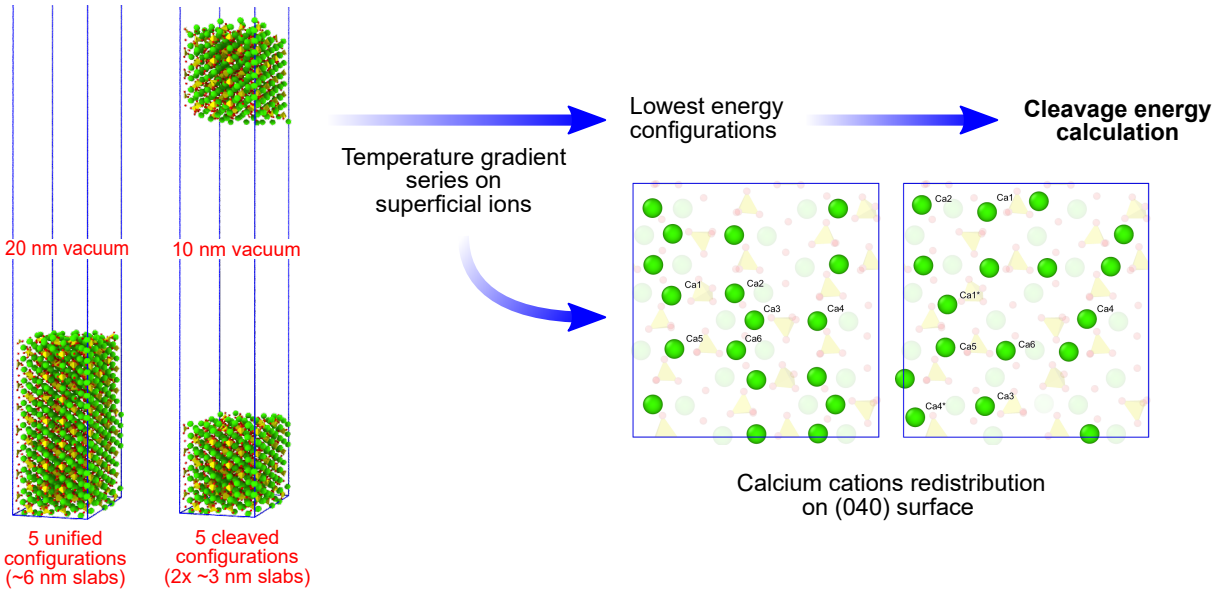

Figure 3.10. Workflow of the cleavage simulations.

For the cleaved system, because the cleaved slabs tend to agglomerate, a spring force of 100 kcal $Å^{-1}$ has been applied to maintain a distance of 10 nm between each surfaces. This process was repeated for several planes perpendicular to the principal directions.

3.5.2 Energy calculation

The cleavage energy is computed from the difference of the averaged energies of the unified and cleaved system, $E_{unified}$ and $E_{cleaved}$, where A is the area of one of the resulting cleaved surfaces (Equation (3.26)). The cleavage energy values are given in Table 3.6. The computed vales are in the range of 1.14 to 1.55 J m^{-2} (1.32 J m^{-2} in average) for M_3 C_3S, and 1.04 1.76 J m^{-2} (1.35 J m^{-2} in average) for M_1 C_3S, in good agreement with first results obtained on M_3 C_3S with the same force field, and almost match for the (040) plane (1.31 ± 0.04 J m^{-2} against 1324 ± 25 mJ m^{-2} [64]). Generally, they are in good agreement with other previous atomistic simulation studies [14, 123]. In general, the average values are very closed between the two models. The energies obtained for particular planes vary as a function of the structure of each polymorph, and is particularly influenced by coordination between calcium cations

M_1 C_3S		M_3 C_3S	
Miller index	Cleavage energy ($J\,m^{-2}$)	Miller index	Cleavage energy ($J\,m^{-2}$)
(100)	1.04 ± 0.04	(100)	1.39 ± 0.03
(010)	1.41 ± 0.04	(300)	1.14 ± 0.03
(040)	1.76 ± 0.03	(800)	1.17 ± 0.03
(003)	1.20 ± 0.03	(010)	1.55 ± 0.04
(008)	1.20 ± 0.04	(040)	1.31 ± 0.04
(110)	1.45 ± 0.04	(001)	1.38 ± 0.04
(101)	1.51 ± 0.03	(002)	1.45 ± 0.04
(011)	1.17 ± 0.04	(003)	1.31 ± 0.04
(111)	1.43 ± 0.03	(00$\bar{3}$)	1.33 ± 0.04
		(008)	1.22 ± 0.04
		(00$\bar{8}$)	1.22 ± 0.04

Table 3.6. Cleavage energies of M_1 and M_3 C_3S. Only the lowest energy plane is given in the (100) direction for M_1.

and oxygen atoms in silicates. The (100) direction of the M_1 polymorph is corresponding to the (001) direction of the M_3 polymorph, and vice-versa. For M_1 C_3S, the present calculation indicates that the lowest energy plane is in the (100) direction, at 2 Å from the origin. The (100) direction of the M_1 polymorph has many possible cleavage planes and the plane for which the lowest energy was computed has no equivalent in the M_3 polymorph.

The Wulff construction can give theoretical insights on the shape of a crystal at equilibrium. It is based on the assumption that a crystal growth in a such way that the Gibbs free energy of its surface is minimized. The surface energy of a plane is proportional to the distance of this surface from the center of the crystal. This means that the crystal growth in a direction is inversely proportional to the energy of the surfaces perpendicular to this direction. Thus, low energy surfaces have larger area than high energy surfaces. From the lowest energy obtained in each direction, the equilibrium shapes of M_1 and M_3 C_3S in Figure 3.11 were created with the construction algorithm implemented in the pymatgen library [97, 134]. In the M_1 polymorph, the crystal grows only along three planes, while in the M_3, seven planes are represented. Maki related that the equilibrium form of alite is usually made up of three

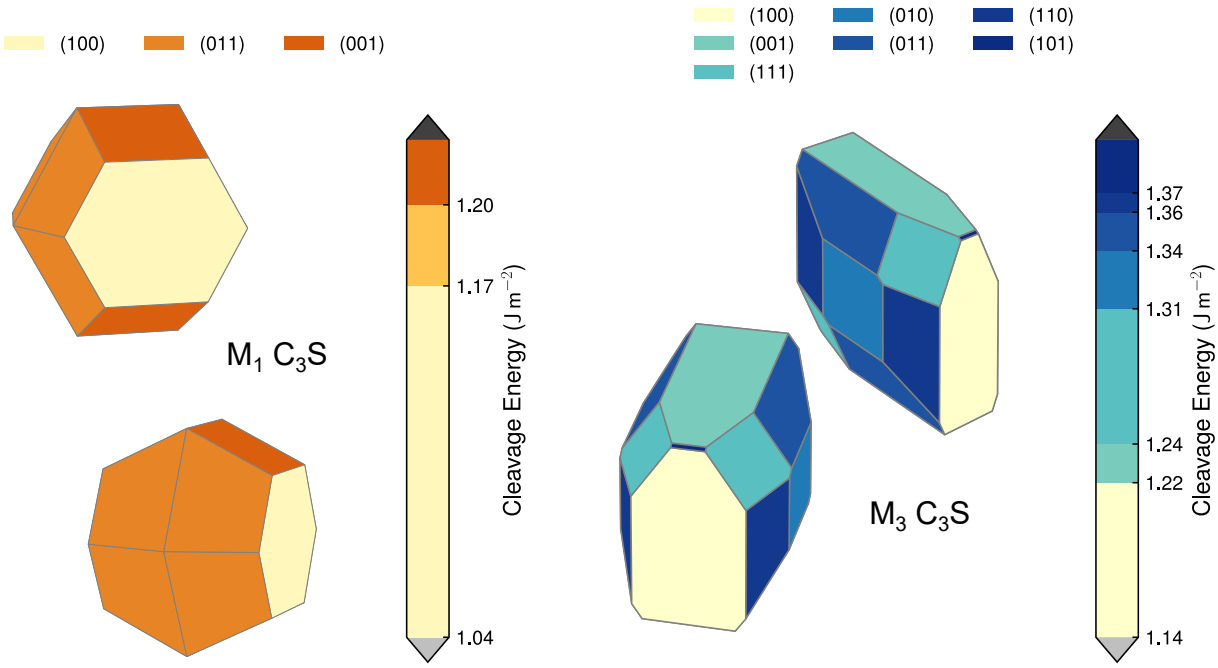

Figure 3.11. Equilibrium shapes of M_1 and M_3 C_3S

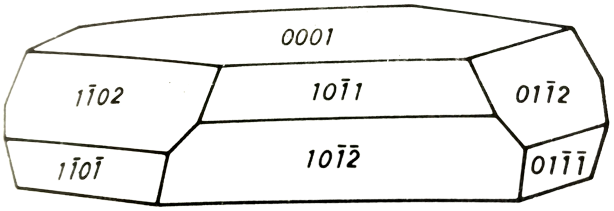

Figure 3.12. Equilibrium form of C_3S, adapted from Maki and Chromý [21, 25].

special forms: one pedion and two rhombohedra, as depicted in Figure 3.12 [21]. The author proposed a morphology similar to the M_1 obtained by Wulff construction, though more flat and with only one rhombohedra form. Maki explains that the crystal form of alite changes during recrystallization from the platelet illustrated in Figure 3.12 to massive granules with well developed pyramidal faces (10$\bar{1}$1) and (1$\bar{1}$02). The ratio between the width and the length of the platelet is function of the environment during the growth. The M_3, which overgrows M_1, is formed as a recrystallization product [21, 28] (see Figure 3.13). One should note that the obtained equilibrium shapes are not fully definitive, since they were determined on a relatively finite number of planes, more calculations would probably refine these shapes, and produce a more accurate prediction.

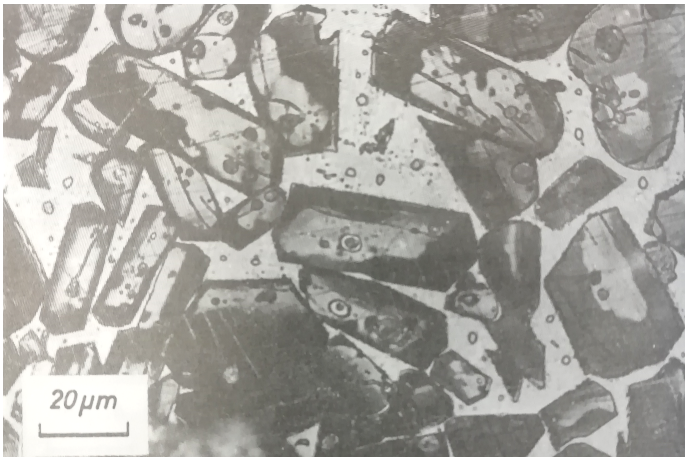

Figure 3.13. Zonal structure with M_3 overgrowing M_1. Reflected light image adapted from Maki [21]

3.6 Conclusion

In this chapter, the mechanical and thermal properties of M_1 and M_3 C_3S were investigated, as well as cleavage energies and equilibrium shapes. The elastic constants were calculated by static and dynamical methods. The elastic constants found by Voigt-Reuss-Hill homogenization of the stiffness constants obtained in static calculation with IFF were found in good agreement with experimental measurements. However, results from DFT calculation and ClayFF overestimated and underestimated experimental results, respectively. Isotropic distribution of elastic moduli in space was observed for M_1, whereas an anisotropic distribution was found for M_3. Bulk modulus was obtained by EMD calculation, and elastic, shear modulus, as well as Poisson's ratio were calculated by NEMD. The results are in good agreement with static calculations and experimental measurements.

Specific heat capacities were calculated by the direct method and from VACF. The direct method provides results greater than experimental measurements, and with much larger error than the VACF method. On the other hand, the VACF allowed to analyse the phonon density of states and provide results much more accurate. The results obtained with ClayFF are very close to previous experimental measurements, and results from IFF are slightly smaller. The DOS obtained from VACF are in good agreement with infrared spectroscopy measurements, and the differences between IFF and ClayFF arise mainly from the bond description of silicates.

Cleavage energy calculations were performed on both M_1 and M_3 C_3S, using a temperature gradient method to relax superficial ions to configurations of lower energy. The energies ob-

tained for both polymorphs are in the same range. The resulting equilibrium shapes, obtained by Wulff construction, are however different, but the planes of low index with lowest energies are the (100) and (001) for both polymorphs. The M_1 construction possess three facets against seven for the M_3. The cleavage energies were calculated for a relatively limited number of planes, and further calculation could lead to even more accurate shapes.

Chapter 4

MD simulation of C_3S/water interface: influence of the protonation state on water's behavior

At the interface with solid surfaces, the structure and dynamics of water are affected by several effects. First, superficial dipolar moments induce an electrostatic field into the fluid. Second, the excluded volume, or "hard-wall" effect induces the packing of water molecules because of the spatial geometrical constraint created by the surface on water molecules [87]. Moreover, within a critical distance, water-surface and water-water hydrogen bonds lead to a layered water structure [87, 135], more disordered than ice nonetheless. The diffusion coefficient of water molecules in these layers is lowered, affecting local density and viscosity. To consider such a heterogeneous behavior, MD overcomes the limitation of continuum mechanics methods by defining the fluid as discrete molecules [136]. When the water is confined between two surfaces, the effects of both surfaces overlap when the confinement is thicker than a critical distance of 15 Å for C – S – H [87], and approximately 2 nm for C_2S and C_3S [135]. The hydrophobicity or hydrophilicity of surfaces affect the preferential interaction of water. In contact with hydrophilic surface, water molecules tend to make H-bonds with surface ions, whereas in interface with hydrophobic surface, water molecules would prefer make H-bonds among them.

In this chapter, the structural and dynamical properties of water at the interface with monoclinic C_3S (040) surface are simulated using a classical force field. IFF is chosen for its ability to reproduce surface and interfacial properties and the recently developed parameters for hydrated C_3S are used [71]. In the computational scheme, various degrees of hydration of the first atomic layer are considered, covering the range of pH at which cement hydration usually occurs. The pH values are given with base on pKa of free silicic acid in solution, according to the model introduced by Pustovgar et al. [71]. For each degree of hydration, interfacial energies, atomic densities, orientation of superficial water molecules and pair distribution functions analysis allow to describe the structural properties of the C_3S/water interface. Finally, diffusion coefficients and hydrogen bonds density and lifetime were computed to depict the dynamic of water molecules near the mineral surface, strongly influenced by hydrogen bonding. The study of water properties at the interface with the mineral could give a first insight on the understanding of the hydration reaction and its influence on the behavior of water close to the mineral surface.

4.1 Methods

The Ca-rich (040) plane, created in Chapter 3 was chosen for this study of the C_3S/water interface. The lower slab of the cleaved system (~3 nm thick) was used to create an interface system with an equilibrated water slab of 9 nm. Based on the methodology of previous interface studies of Portlandite [56, 58], the periodic images of mineral and water slabs were separated by a vacuum of approximately 7 nm to avoid any interaction through the periodic boundary and to allow the volume of both slabs to fluctuate perpendicularly to the interface and thus lowering the influence of confinement stresses. Four degrees of hydration were investigated, covering pH from largely greater than 15 for the dry C_3S/water interface, to 11.5 for the most hydrated system. To model pH conditions, we applied the last IFF model for hydrated C_3S [71]. The superficial silicate and oxygen anions of the bottom subslab of the cleaved system were protonated, and the charge neutrality of the system was respected, according to the following chemical reactions:

$$
\begin{aligned}
O^{2-} &\xrightarrow{H_2O} 2\,OH^- \\
SiO_4{}^{4-} &\xrightarrow{H_2O} HSiO_4{}^{3-} + OH^- \\
HSiO_4{}^{3-} &\xrightarrow{H_2O} H_2SiO_4{}^{2-} + OH^- \\
H_2SiO_4{}^{2-} &\xrightarrow{H_2O} H_3SiO_4{}^{-} + OH^-
\end{aligned}
\tag{4.1}
$$

In the NVT ensemble at 298 K, an equilibration was performed for 0.5 to 1 ns before starting a production run of 2 ns. For the whole set of simulations, the equations of motion were integrated with a 1 fs timestep using the time integration of the Verlet algorithm and a Nose-Hoover thermostat, with a damping factor of 0.1 ps respectively. The trajectory was recorded for analysis every 0.1 ps. All the simulations were carried out using the LAMMPS package [107]. The PCFF function expression of the INTERFACE FF (PCFF-IFF) was employed to reproduce interactions of both water and C_3S with a cutoff distance of 12 Å for van der Waals interactions and an Ewald summation with an accuracy of 10×10^{-5} for Coulomb interactions was adopted. For water, the full PCFF description of bonded interactions was employed, including cubic and quartic terms of bonded interactions while the PCFF-IFF force field for C_3S only contains quadratic terms (see Chapter 2). Note that the PCFF-IFF uses partial atomic charges, different from those appearing in Equation (4.1). The methodology used in this study is illustrated in Figure 4.1.

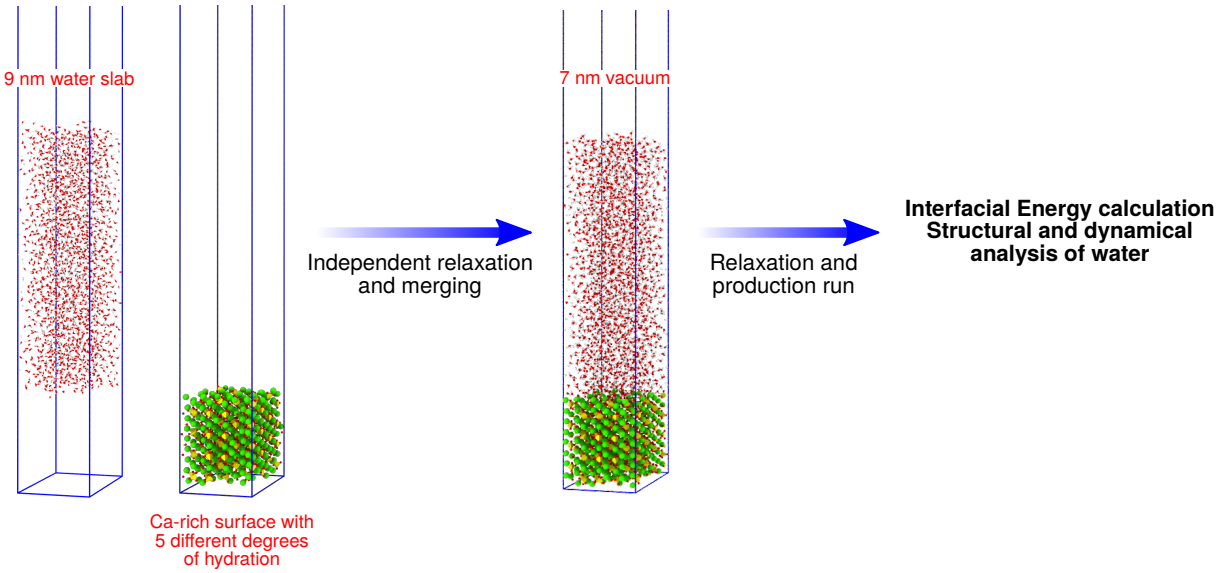

Figure 4.1. Workflow of the interface simulations.

Several properties were computed from the trajectories to analyse the structure and the dynamics of interfacial water. The 1D density profile of water oxygen and hydrogen along the axis perpendicular to the surface, allows to quantify the number of layers and the critical distance, where the water layering decays. The 2D density allows to identify the bonding sites between water molecules and superficial ions. First, volumetric maps were created with the VolMap plugin of the VMD software [137], by dividing the box volume in spacial bins. The occupancy of every bins was evaluated at each step during the simulation run and averaged. The averaged values divided by the bin volume gives the atomic density profile. The obtained 3D density maps were read with the gridData module of the MDAnalysis Python library [138] and projected over the desired axes. The evolution of the number of hydrogen bonds (HB) by water molecule at the interface was obtained with a Python script using the MDAnalysis library [138]. This script takes a donor and an acceptor selection as input. So the water selection can be donor, acceptor or both. For each timestep, the occurrences of hydrogen bond are determined by a geometrical criteria (angle and bond), and the positions of donors and acceptors, as well as the positions of water molecules, are collected in arrays. The arrays are histogrammed over the length of the simulation box in the desired direction, resulting in three histograms h_{donor}, $h_{acceptor}$, h_{water}. The number of donor and acceptor of HB by water molecule is given by the quotients h_{donor}/h_{water} and $h_{acceptor}/h_{water}$, respectively.

4.2 Results and discussion

4.2.1 Energy calculation

The interfacial energy is computed by subtracting the energy of the C_3S slab system E_{C_3S} and the energy of the water slab system E_{water} to the energy interface system $E_{C_3S/water}$, and dividing by the contact surface area A:

$$E_{int} = \frac{E_{C_3S/water} - E_{C_3S} - E_{water}}{A} \tag{4.2}$$

The interfacial energy of simulated systems are given in Table 4.1 with corresponding pH, according to the last IFF model [71]. The interfacial energy is an indicator of the hydrophilic/hydrophobic behavior of the surface. The loss of energy in absolute value traduces a more hydrophobic behavior of the surface as the degree of hydration increases. This behavior is di-

System	pH	Interfacial energy ($J\,m^{-2}$)
Dry C_3S	$\gg$15	-1.42 ± 0.16
1st hyd.	>15	-1.03 ± 0.17
2nd hyd.	~15	-0.64 ± 0.16
3rd hyd.	~13.5	-0.60 ± 0.16
4th hyd.	~11.5	-0.50 ± 0.16

Table 4.1. Interfacial energy for different degree of hydration

rectly related to the charge distribution occurring during the reactions in Equation (4.1), making the hydrogen bonds (H-bonds) between water molecules and surface ions weaker. The energies computed are different and follows the reverse trend than values obtained in previous work [71]. Sign convention and difference in methodology could be the reason for such disagreement. Note that in the present scheme, the water and the C_3S slabs are separated by a vacuum and only interact on one side. The energy of the interface system is greater than the sum of the energies of the two separated systems, because it includes Coulombic and van der Waals interactions between water and C_3S. As expected, the surface is becoming more hydrophobic and hence less reactive upon hydration. The attraction forces between the water molecules and the surface are weakened with hydration of the superficial atomic layer, which is traduced by a decrease in absolute value of the interfacial energy.

4.2.2 Structural properties

The atomic density profile ρ perpendicularly to the surface pictures the structural change occurring with hydration of the first layer of C_3S (Figure 4.2). Looking at the atomic structure of the mineral, the diffusion of calcium cations Ca^{2+} starts slightly with the protonation of oxide O^{2-} to hydroxyl OH^-, but is greatly increased by the first protonation of silicates ($SiO_4{}^{4-}$ to $HSiO_4{}^{3-}$). In fact, the structure of C_3S is known to be largely affected by the orientation of silicates, and by the coordination of Ca^{2+} with the oxygen atoms of silicate groups (Os herein) [16]. At pH ~11.5, Ca^{2+} and OH^- desorb up to 4 Å from their initial positions. The partial charges used in this simulation (+1.5 for Ca, and -0.75 for OH^-) allow to describe properly the solid state of C_3S and to balance the charge of the protonation of oxide Oi (with partial charge

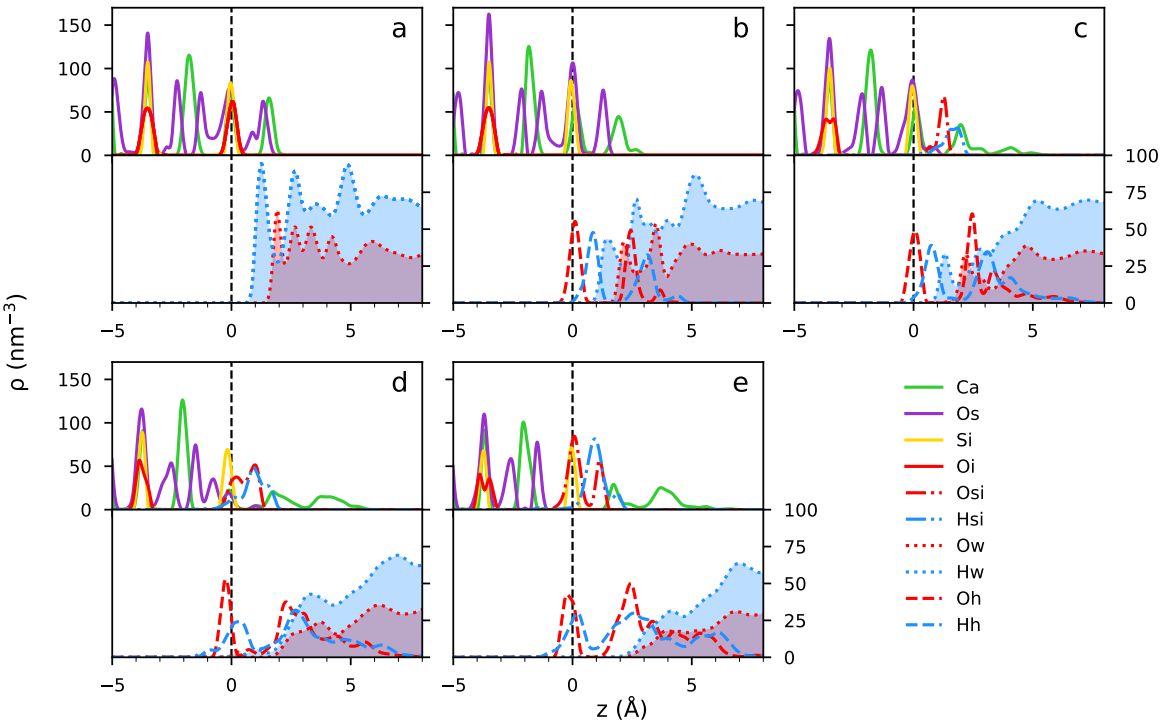

Figure 4.2. Atomic density profiles of the interface for a) Dry C_3S (pH $\gg$15), b) 1st hyd. (pH >15), c) 2nd hyd. (pH ~15), d) 3rd hyd. (pH ~13.5), e) 4th hyd. (pH ~11.5). The interface (z = 0) is defined as the average position of the uppermost layer of silicon atoms. Code for atom nomination: Os for silicate oxygen, Oi for oxygen anion, Oh and Hh for hydroxyl oxygen and hydrogen, Osi and Hsi for silanol oxygen and hydrogen, Ow and Hw for water oxygen and hydrogen.

-1.5), however the solvated species cannot be reproduced with great accuracy by considering these charges, this is why ionic diffusion in water was not investigated here. Water molecules exhibit a layered organization up to 8 Å from the interface, defined as the average position of the uppermost Si layer. The top Si layer was chosen as reference because its position does not change significantly between each simulation. This behavior of silicates is consistent with 2 ns reactive MD simulations of C_3S hydration where only rotational motion was observed [14]. The first, strongly bonded water layer is characterized by a clear peak of the Ow atomic density profile at approximately 2 Å of the interface with an atomic density of almost twice the bulk atomic density (~63 nm^{-3}). Each water molecule of the first layer shares two H-bonds with the oxygen atoms of the surface and three types of hydrogen bonding were identified from the density map: two Hw–Oi bonds (a), two Hw–Os bonds (b), one Hw–Oi and one Hw–Os bond (c) Figure 4.3.

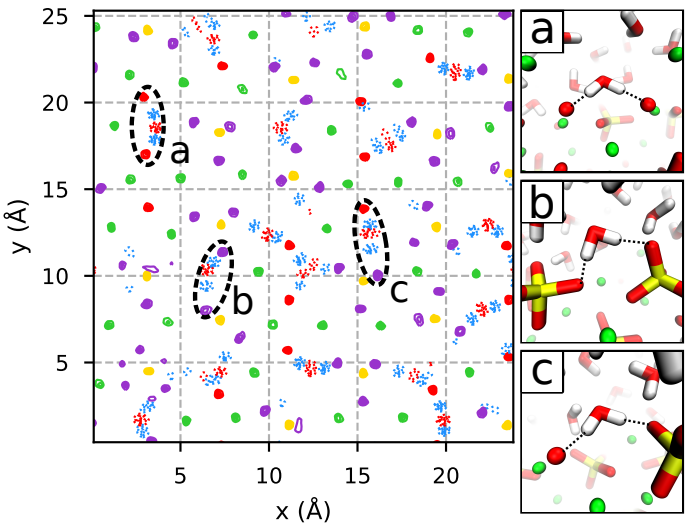

Figure 4.3. Atomic density maps for dry C_3S / water interface of water molecules of the first layer (0.5 Å < z < 2.4 Å) (left). Zoom on the three hydrogen bonding types: a) two Hw–Oi, b) two Hw–Os bonds, c) one Hw–Oi and one Hw–Os bond (right). Color map: Ca in green, Oi in red, Si in yellow, Os in violet, Ow in red dotted line, Hw in blue dotted line.

These three bonding types are the bases of the H-bonds network at the origin of the layered structural arrangement. In the second layer, water molecules form H-bonds with Os or Oi atoms from the surface, and with near water molecules. This intermediate position is more unstable and explains the scattering of the following peaks on the Ow density profile. While the hydration occurs, the strong layered structure formed by water molecules decays with the diffusion of Ca^{2+} and OH^-. After the first protonation reaction (O^{2-} to OH^-), the positions

of the three Hw atomic density peaks, and the intensity of the third peak, remain almost unchanged. The decaying of the layered structure becomes much more significant after the protonation of SiO_4^{4-} to $HSiO_4^{3-}$, although the first Ow and Hw atomic density peaks are still observable at pH ~15. In the case of the dry surface, every water oxygen atoms are donors, but are becoming progressively acceptors when the protonation state of the surface increases, allowing for Hh–Ow and Hsi–Ow bonds to occur.

The orientation probability distribution (OPD) of a water molecules on the mineral surface gives information on the interactions occurring at the interface. This analysis was performed with the AngularDistribution method of the Water dynamics analysis module of the MDAnalysis Python library. The orientational preference of water molecules within 2.5 Å from the surface is here defined by the angle θ between the z axis, and the dipolar moment of water. Figure 4.4 shows the OPD function $P(\theta)$ versus $cos\theta$ for different hydration degree.

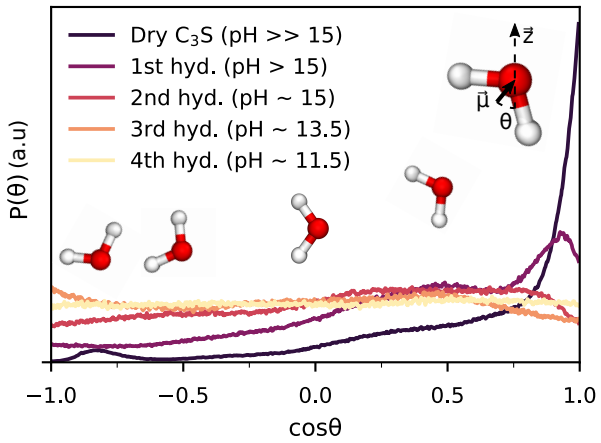

Figure 4.4. OPD of water molecules within 2.5 Å from the surface with variation of the degree of hydration.

Water molecules strongly interact with Os and Oi on the C_3S dry surface, which corresponds to a sharp peak at $cos\theta$ = 1.0, for the first degree of hydration (pH >15), a small orientational preference still exists, but $P(\theta)$ can be considered as uniform from the second degree of hydration investigated (first protonation of silicates), traducing a greater rotational motion of water molecules due to a loss of interaction with the surface.

Complementary structural information was given by the RDF between water and C_3S superficial atoms using the g(r) plugin implemented in the VMD program [139] Figure 4.5. For Ow-Ow pairs, the RDF was computed between Ow from every water molecules and Ow within

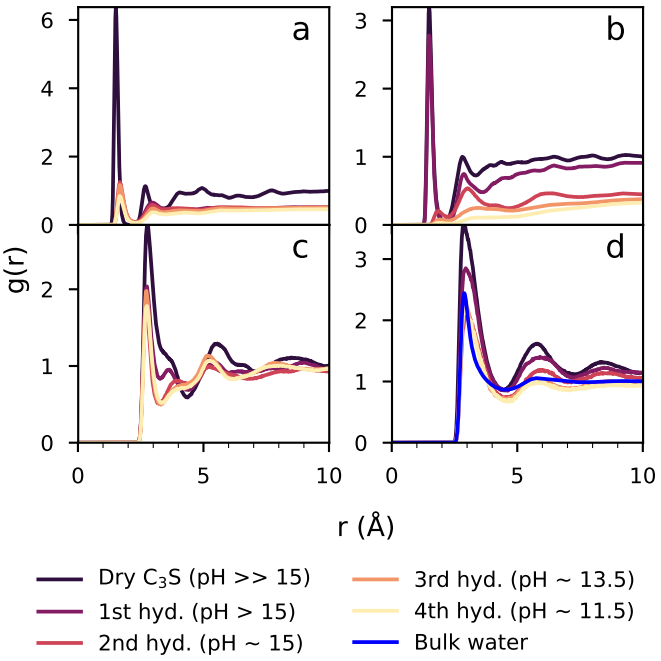

Figure 4.5. Radial distribution function of a) Oi-Hw and Oh-Hw, b) Os-Hw and Osi-Hw, c) Ca-Ow, d) Ow-Ow, for different degrees of hydration.

2.5 Å from the surface. The overall observation is that the water atoms lose coordination with the superficial species with increasing of the hydration degree. The coordination peaks of Oi-Hw and Os-Hw are shifted to the right with protonation of Oi and Os to Oh and Osi, traducing a weakening of H-bonds between these species. Oh-Hw pairs have a first coordination shell at ~1.7 Å and a second coordination shell at ~3.0 Å. Osi-Hw RDF shows a very weak first coordination shell at ~1.9 Å, and a second coordination shell at ~3.1 Å. Interestingly, a third Osi-Hw coordination shell exists at pH ~15 at an inter-atomic distance ~6.2 Å. Oh-Hw and Osi-Hw coordination peaks disappear with further hydration. The peak of the first Ca-Ow coordination shell is shifted to the left after the first hydration, due to the start of solvation of Ca^{2+} and the Ca-Ow RDF does not change significantly after the first protonation of silicates. The water interfacial structural features are well represented by the Ow-Ow RDF. A second and third coordination shell peak are present at 6.2 Å and 8.3 Å respectively for water molecules on the dry surface, and decay with hydration of the surface, until matching the Ow-Ow RDF of bulk water.

4.2.3 Dynamical properties

The investigation of dynamical effects can provide precious information on the interaction between water and mineral surfaces [140]. The dynamical properties such as diffusion coefficient and H-bonds lifetime can be significantly altered by the presence a mineral surface.

When a concentration gradient exists in a liquid, molecules tend to move towards a uniform distribution. This phenomenon is called diffusion. Changes in concentration over time can be described by the macroscopic Fick's second law:

$$\frac{\partial C(\mathbf{r}, t)}{\partial t} = D\nabla^2 C(\mathbf{r}, t) \tag{4.3}$$

where the proportionality constant D is the diffusion coefficient, and $C(\mathbf{r}, t)$ is the concentration of particles at time t and position $\mathbf{r}$. In 1905, Einstein related Fick's second law with the disordered motion of particles suspended in a liquid, assuming that particles move independently from each other according to a symmetrical distribution function $\varphi(\Delta)$ [141]:

$$D = \frac{1}{2\tau}\int_{-\infty}^{+\infty} \Delta^2 \varphi(\Delta) \mathrm{d}\Delta = \frac{1}{2\tau}\left\langle \Delta^2 \right\rangle \tag{4.4}$$

where Δ is the change in a specific coordinate of the individual particles, which differs for each particle. $\varphi(\Delta)$ describes the number of particle experiencing a displacement lying between Δ and $\Delta + \mathrm{d}\Delta$ in the time interval τ. The value $\left\langle \Delta^2 \right\rangle$ is called the mean squared displacement (MSD) in one direction. In the limit of an infinitely long observation time, and for n dimensions problem, the diffusion coefficient is:

$$D = \frac{1}{2n}\lim_{\tau\to\infty} \frac{\left\langle [\mathbf{r}(t_0 + \tau) - \mathbf{r}(t_0)]^2 \right\rangle}{\mathrm{d}\tau} \tag{4.5}$$

where $\left\langle [\mathbf{r}(t_0 + \tau) - \mathbf{r}(t_0)]^2 \right\rangle$ is the double averaged mean square displacement. The first average is applied on the water molecules contained in the specified group, the second average is performed over time intervals of span τ. In the present calculation, because of the mentioned perturbations caused by the mineral surface, the behavior of water molecules in an interfacial system is heterogeneous and isotropic. Water molecules are free to desorb and adsorb on the surface, moving along the z axis towards or away from the surface, meaning that depending on the position and the direction considered, the diffusion coefficient will vary. So the observation time τ must be sufficiently long to capture the molecules in diffusive regime, but sufficiently short to represent diffusivity in a specific region. Therefore, based on a calculation

method of a previous study [142], the trajectory of the Ow atoms was analyzed updating the selection every 10 ps time slices and in volume slices of 1 Å along the z axis. Within the 10 ps time slice, D was computed from the slope of MSD with τ varying from 2 to 8 ps, using the diffusion coefficient tool for VMD [143]. The evolution with distance from the C_3S surface for different degree of hydration is shown in Figure 4.6.

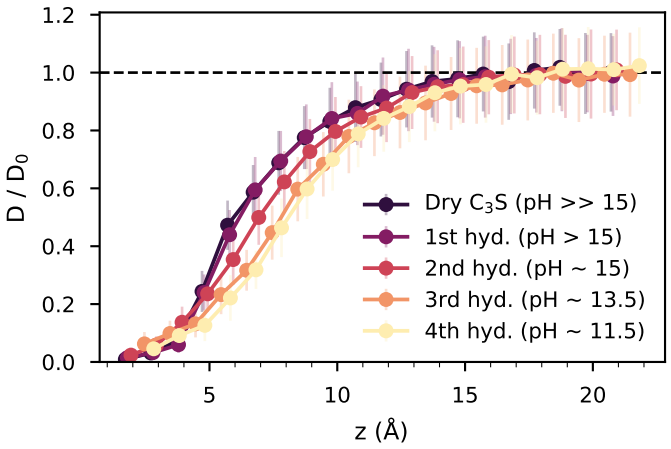

Figure 4.6. Evolution of the diffusion coefficient of water molecules with distance from the C_3S surface with variation of the degree of hydration. The interface ($z = 0$) is defined as the average position of the uppermost layer of silica atoms.

Up to 4 Å from the interface, no significant variation has to be noted between simulated systems. For greater distance, the diffusion coefficient D decreases with the degree of hydration of the surface because of the perturbation introduced by the diffusion of Ca^{2+} and OH^- ions. At approximately 20 Å from the surface, the calculated bulk diffusion coefficient D_0 was ~6.25×10^{-9} m^2 s^{-1} against $7.26 \pm 0.02 \times 10^{-9}$ m^2 s^{-1}, computed on a cubic box of 30 Å side, at T = 298 K in NVT ensemble. This difference could arise from the above described computation method. The shape and the size of the box may also cause such difference [144]. Note that the diffusion coefficient of PCFF water is much larger than for flexible SPC water model ($3.20 \pm 0.03 \times 10^{-9}$ m^2 s^{-1}, calculated in the same conditions than for bulk PCFF water), and experimental diffusion of pure water (2.3×10^{-9} m^2 s^{-1}) [145]. Because of differences in structure and dynamics of water models, as well as size and shape effects, the absolute values of D must be taken with care, and it is purposed here to characterize the decrease in translational mobility of interfacial water molecules with increasing of the degree of hydration of the first atomic layer.

The number of hydrogen bonds that water molecules create with a mineral surface depicts its hydrophilic or hydrophobic behavior. In this H-bonds analysis, we consider both the number of H-bonds created and their lifetime. The existence of H-bonds was defined by a geometric criterion. For every possible donor, hydrogen, acceptor combination, an H-bonds exists if and only if the distance r between the acceptor oxygen and the hydrogen is smaller than 2.45 Å, and the angle β between the hydrogen, the donor oxygen and the acceptor oxygen is smaller than 40°. The distance criterion was defined as the first minimum of the O-H radial distribution function of bulk PCFF water. Although an angle of 30° is usually proposed, a larger tolerance was chosen here because of the much larger dispersion in the distribution of β for the PCFF water model compared to the reference SPC model. Even increasing the angle tolerance, the average number of H-bonds at standard state resulted in 3.33 for PCFF bulk against 3.48 for SPC water, and ~3.3 obtained experimentally by K-edge X-ray absorption [146]. The number of H-bonds per water molecule was analyzed along the z axis with variation of the degree of hydration (see Figure 4.7). When considering water in contact with the dry C_3S, the total H-bonds number decreases at about 4.7 Å of the first Si layer because of a loss of H-bonds acceptance from water. Ow donates Hw to silicate oxygen Os, and interestingly, the water H-bonds acceptance from other water molecules also increases within 2.6 to 4.0 Å from the surface. The role of water molecules in this layer (the second layer from the surface) is intermediate between acceptor and donor. They donate on average, approximately one Hw to an Os from the surface and one Hw to an Ow of the first water layer, while they accept one hydrogen from the above water molecules. The total H-bonds nearest peak from the surface corresponds to the first water layer observed in the Figure 4.2. In this layer, water molecules only donate H-bonds to Oi and Os and accept H-bonds from water molecules of the second layer. For the first hydrated interface (pH $\gg$15), the hydrogen bonds distribution between water molecules against the distance from the C_3S surface follows the same trend but with a decreased intensity. This is because water molecules are accepting H-bonds from Oh. While the number of Ow-Oi and Ow-Os H-bonds per H_2O was about 1, the preferential interaction site is now Ow-Os due to hydroxylation of Oi and loss of polarity. Hence, the number of Ow-Os H-bonds per H_2O increases near the surface up to 2. The distribution of hydrogen bonds between water molecules decays almost linearly from the bulk to the surface after the second protonation reaction of silicates (pH < 13.5). As expected with the increase of the degree of hydration, water molecules are forming more H-bonds with Osi and Oh (donor and acceptor),

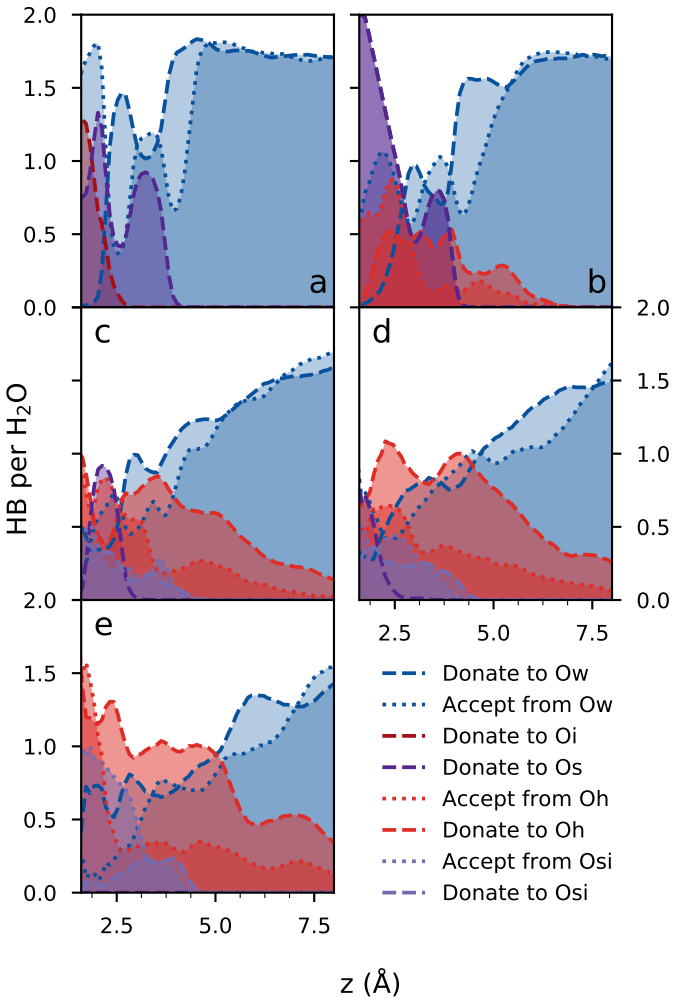

Figure 4.7. Evolution of the number of hydrogen bonds per water molecules along the z axis with variation of the degree of hydration: a) Dry C_3S(pH $\gg$15), b) 1st hyd. (pH >15), c) 2nd hyd. (pH ~15), d) 3rd hyd. (pH ~13.5), e) 4th hyd. (pH ~11.5). The interface (z = 0) is defined as the average position of the uppermost layer of silica atoms.

and less with Os. The total H-bonds/H_2O number is increasing up to 4.6 within 2.5 Å from the most hydrated surface (pH ~11.5) and no H-bond between Ow and Os is reported for this system because the remaining Os atoms point towards the bulk of C_3S. From the protonation of ${SiO_4}^{4-}$ to ${HSiO_4}^{3-}$, the hydrogen bonds formed between water molecules is decreasing and water in contact with the surface does not present structural features anymore.

Hydrogen bonds lifetime was measured using the continuous autocorrelation function definition implemented by Gowers and Carbone [147] in the MDAnalysis Python package [138]:

$$C_c(t) = \left\langle \frac{\sum_{i,j} h_{ij}(t_0) h_{ij}(t_0 + t)}{h_{ij}(t_0)^2} \right\rangle \tag{4.6}$$

where the binary function $h_{ij}(t)$ is equal to 1 if an H-bonds exists between an acceptor i and a donor j, and 0 if not. In the continuous autocorrelation function, if an H-bonds is broken at a particular moment, it remains broken for the rest of the analysis time and cannot reform. The autocorrelation function $C_c(t)$ is fitted using the sum of two exponential functions and integrating over time:

$$C_c(t) \approx A_1 \exp\left(\frac{-t}{\tau_1}\right) + (1 - A_1) \exp\left(\frac{-t}{\tau_2}\right) \tag{4.7}$$

Finally the lifetime τ of the bond is assessed by integrating the fitted function:

$$\tau = \int_0^\infty C_c(t) \tag{4.8}$$

All the binary function were evaluated every 0.1 ps during the entire production run of 2 ns. The resulting $C_c(t)$ and τ are presented in Table 4.2.

τ (ps)	Ow-Oi	Ow-Os	Ow-Oh	Oh-Ow	Ow-Osi	Osi-Ow	Ow-Ow
Dry C_3S	902.79	186.87	—	—	—	—	0.61
1st hyd.	—	146.29	5.19	0.44	—	—	0.37
2nd hyd.	—	14.50	4.87	0.43	1.48	0.90	0.64
3rd hyd.	—	0.96	2.90	0.59	0.31	1.96	0.52
4th hyd.	—	—	2.94	0.08	0.77	1.51	0.49

Table 4.2. Lifetime of hydrogen bonds with variation of the degree of hydration.

As expected, for the dry C_3S/water interface, the lifetime of Ow-Oi H-bonds is much higher than for Ow-Os. These values are related to the greater acidity of hydroxide anions compared

with free silicic acid in water. One should note that in this classical MD study, reactions of dissociation and protonation cannot occur so these two values are overestimated. In fact, water molecules would react preferentially with Oi. On average, and as expected, H-bonds lifetimes are decreasing with decreasing pH.

4.3 Conclusion

The model used here allowed to assess for the first time the behavior of water molecules on the Ca-rich (040) cleavage plane of M_3 C_3S, with variation of the degree of hydration of the first superficial atomic layer. The layered structure of water, observed at the interface with the surface, decays from the hydration of oxides and is strongly affected by the protonation of silicates ${SiO_4}^{4-}$ to ${HSiO_4}^{3-}$. We thus showed that the structural behavior of water is based on the strength of the hydrogen bonds created between the first water layer and the ionic species of the mineral surface. When those hydrogen bonds are stable, the existing network remains well defined and structured. The protonation of oxides and oxygen atoms of silicate leads to changes in charge distribution and weakens hydrogen bonds between the surface and the first water layer. This behavior is reflected in the orientation probability distribution water molecules of the first layer. A preferential orientation of water molecules on the dry C_3S exists because of the three bonding types observed (namely Oi-Ow-Oi, Os-Ow-Os and Oi-Ow-Os), whereas H_2O molecules gain rotational motion when hydration occurs, with uniform orientation probability distribution. In the range of 4 to 16 Å from the interface, their translational motion decreases with the degree of hydration because of the perturbation introduced by the solvated ionic species. The study of dynamical properties such as diffusion and lifetime hydrogen bonds adds new insights into the interfacial behavior related to hydration reactions. An even better accuracy regarding dissociation and solvation can be obtained by changing the charge of calcium cations and/or modifying the water model [64]. The present simulations treat the protonation steps incrementally, and allowed to describe the behavior of water at several degree of hydration of the first atomic layer. Reactive MD as well as *ab initio* MD are appropriate methods to investigate water dissociation and protonation reactions towards a better understanding of mechanisms responsible for dissolution and formation of C – S – H.

Chapter 5

AIMD simulation of C_3S/water interface: protonation state and proton transfer analysis

In recent studies, molecular and dissociative adsorption of single water molecule were investigated on multiple surface planes of M_3 C_3S polymorph [68, 69, 148]. Zhang et al. have shown that the adsorption energy decreases with increasing adsorbed molecules. Reactive MD studies indicates that after approximately 0.3 ns, the structural properties of the surface are lost, making further hydration process independent from the surface plane, and driven by proton hopping mechanisms towards the bulk [14, 149]. No correlation was found between water adsorption energy and surface energy, when using static computational methods [14]. However, the proton diffusion after the initial stage of hydration was related to the location of the valence band maximum (VBM), which is mainly constituted of oxygen 2p orbitals [149, 150]. Previous DFT studies reveal that the local density of state of the VBM is closed to the oxygen anions for C_3S, and closed to oxygen in silicates for C_2S [17]. The highest reactivity of C_3S when compared to C_2S is explained by the difference in their electronic structure, arising from the presence of oxygen anions in C_3S. Calculations of a single water molecule sorption on a (100) surface of T_1 C_3S, shown that chemisorption occured only in regions closed to oxide ions. This behaviour was associated to the higher degree of freedom of oxide ions when compared to oxygen in silicate [149].

Proton transfer (PT) frequency strongly depends on hydrogen bonds (HB) fluctuation due to thermal motion [151], and thus cannot be analyzed by a 0 K, DFT investigation. Furthermore, such a phenomenon cannot be captured considering single water adsorption. A previous computational study found structural changes, as well as a huge increase in PT rate from a solid/water monolayer interface to a thicker water film. Towards a better understanding of the C_3S/water interface, we performed an *ab initio* MD (AIMD) simulation, considering a water film thick enough to account for fluctuation of the HB network. AIMD is a powerful tool that has been used extensively to investigate the structural and dynamical behavior of water/oxide interfaces at the DFT level of theory [151–158]. However, only few AIMD studies were conducted on cimentitious materials [159–161]. As far as we know, this is the first time that the very early hydration stage of C_3S is investigated using AIMD. In particular, the structure of water and the PT dynamics are analysed and quantified, and the results are compared with reactive molecular dynamics calculations, performed for that purpose.

5.1 Computational Methods

A simulation of the C_3S/water interface was performed on the symmetric, Ca-rich, (040) plane. The M_3 C_3S model employed was refined from XRD analysis by Mumme et al. [34]. In order to build a surface model, the monoclinic unit cell optimized in Chapter 3 was converted to an orthorhombic supercell of 162 atoms, with lattice parameters a = 12.28 Å, b = 7.09 Å and c = 25.59 Å. The surface model was created from three orthorhombic supercells, with a 20 Å thick vacuum layer, thus resulting in a 12.28 Å × 25.59 Å × 21.28 Å structure. The relaxation of the surface and the AIMD simulation were performed with the CP2K code, using a PBE functional, and a combination of Gaussian and plane wave basis functions (GPW), with Grimme D2 correction. A 400 Ry planewave cutoff was adopted, and the reciprocal space was sampled only at the γ point. To relax the surface, the periodicity was applied for in-plane directions, and removed in the direction of the vacuum. The atoms of the surface were allowed to relax at the DFT level, ensuring that almost no change occurs within the middle of the slab. The interface model was created adding a 15 Å thick layer of water (157 molecules), with a 15 Å vacuum region. The structure of the C_3S(040)/water interface is depited in Figure 5.1.

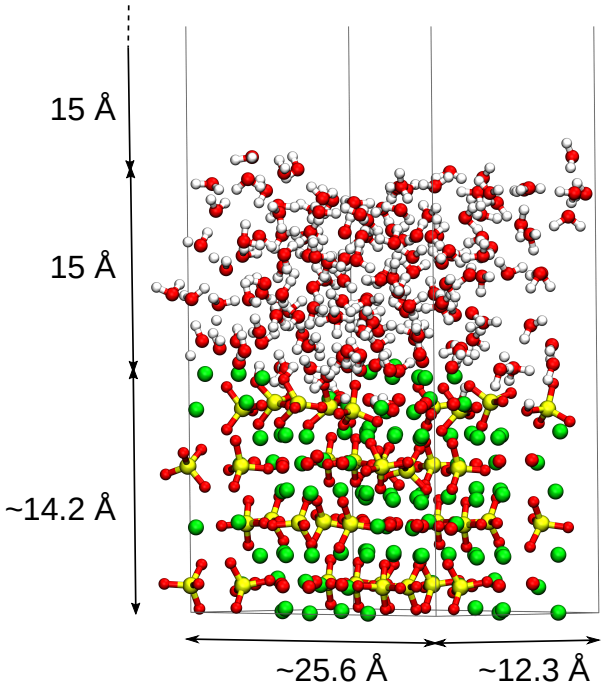

Figure 5.1. Structure of the investigated C_3S(040)/water interface.

While the atoms of the mineral surface were kept fixed, the water molecules were allowed to relax on the surface during a 2 ns classical MD run in NVT ensemble at 300 K, using the INTERFACE FF parameters for the C_3S [64] and a SPC model for water. In order to minimize the computational time, the bottom layer was removed so that the remaining slab was composed of two orthorhombic supercells (~14 Å thick) and during the AIMD run, the lower supercell, considered as the bulk, was fixed. Afterwards, a 12 ps AIMD run was performed within the Born-Oppenheimer approximation, in the canonical ensemble, with a Nose-Hoover thermostat, integrating the equation of motion with a 0.5 fs timestep. The equilibration of the system was performed on the first 2 ps simulation, and the remaining simulation time was used for analysis. A slightly higher temperature of 360 K (compared to standard conditions) was used to balance the low diffusivity of water using the PBE functional. Deuterium masses were used for protons to minimize the vibrational frequency of nuclei, allowing to keep a good energy conservation [162]. A reactive molecular dynamics simulation was performed using the ReaxFF, with the current optimized set of parameters for Ca/O/H/Si elements [46, 59, 94]. The simulation method and parameters, as well as the system size, are in accordance with previously reported calculations [14]. The total calculation time for the AIMD and ReaxFF simulation was 78 days and 6 hours, and 11 hours and 23 minutes on 48 and 24 Intel Xeon Gold 5120 CPUs @ 2.20 GHz, respectively.

The trajectory analysis involves Python scripts, using the MDAnalysis library [138]. The number of hydroxyl groups was determined by count of the number of water hydrogen atoms Hw at 1.2 Å from oxide ions Oi or oxygens in silicates Os. For hydroxyl groups resulting from water dissociation, water oxygens Ow at 3.0 Å from atoms in C_3S was selected, and Ow with only one Hw within 1.2 Å were counted. The selections were updated at each step. To analyse the orientation of water molecules, the dipole vector of each water molecule was constructed by addition of the vector made by the O-H bonds. In one script, the angles θ between the z axis and the dipole vector was collected in a array, as well as the distance with the interface, defined as the average z coordinate of the Os atoms. In another script, the angle θ and the x and y coordinates were collected. The collected values were histogrammed. The PT frequency was analysed by finding unique trinomials (Ow, Hw, Ok) within a distance allowing for proton exchange. Ok refers to an Os atom, or an oxygen atom from OH^- remaining upon protonation of Oi or Os, herein called Odw, within 3.0 Å atoms in C_3S. For each trinomials, the distances Ow-Hw and Ok-Hw where monitored over time and continuous time series where produced. The location in time where the PT occurs, allowing to determine their lifetime τ. The values were histogrammed to determine the frequency. The same selections were used to map the free energy as a function of the distance between oxygen atoms and relative distance between the hydrogen atoms and each oxygens in these trinomials. These variables were collected to create a 2D histogram. The general computational method to analyse the trajectory is depicted in Figure 5.2.

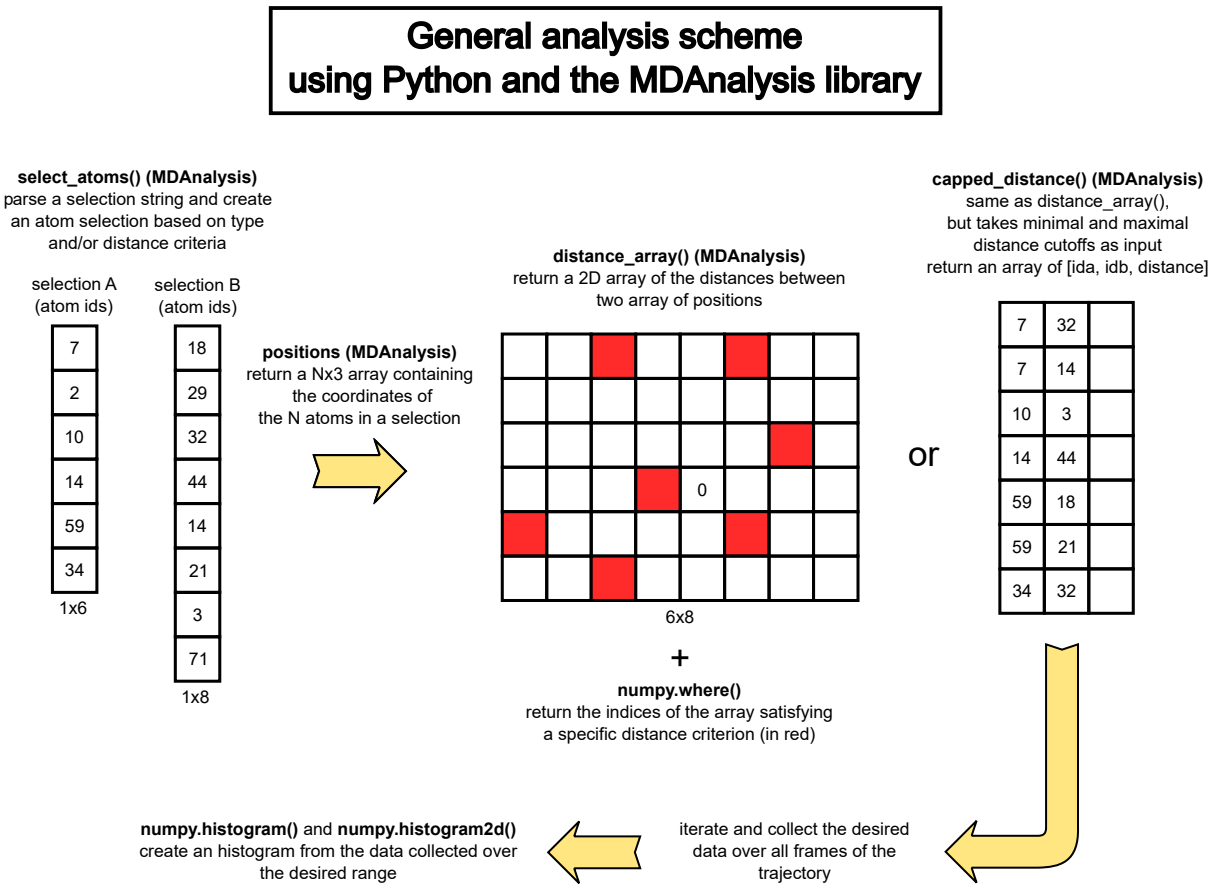

Figure 5.2. General analysis scheme using Python and the MDAnalysis library

5.2 Results

5.2.1 Water structure

At the very first steps of the simulation, three oxide ions Oi from equivalent sites are protonated. The hydration model for C_3S proposed by Pustovgar et al. considers that protonation of oxide ions occurs before protonation of silicates [71]. Although hydroxides are more stable than silanol groups, our simulation indicates that on the considered (040) Ca-rich surface, protonation of Oi only occurs on sites closed to silicates. The other superficial oxide ions are shielded by four calcium cations, hindering any protonation reaction. The negatively charged region allows water molecules to form hydrogen bonds between oxide ions and oxygens in silicates, thus leading to protonation of Oi (see Figure 5.3).

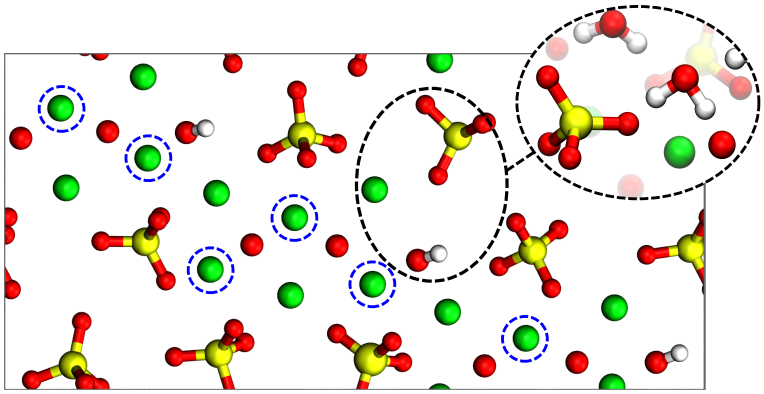

Figure 5.3. Atomic structure of the (040) surface. Color code: calcium cations in green, oxygen anions and silicate oxygen in red, silicon atoms in yellow and hydrogen in hydroxide H-Oi in white. The snapshot shows the position of the water molecule before protonation of the oxide. The ions of the surface are in the same layer, except for the calcium indicated by blue circles, having perpendicular coordinate z ~2 Å larger.

The number of H-Os groups formed on silicates tends to stabilize after ~1 ps whereas the number of H-Odw groups stabilize after ~0.25 ps (see Figure 5.4). Both hydroxyl groups fluctuate during the whole simulation due to proton transfer. Conversely, the hydroxides H-Oi formed on xygen anions Oi are very stable and no backward PT occurs. From our simulation using the ReaxFF, within the timescale of 12 ps, a steady state is reached very quickly as in the AIMD simulation. However, no PT dynamics is observed, meaning that with the hydroxyl groups formed in the ReaxFF simulation are very stable, and that ReaxFF cannot account for

proton transfer between water and Oi/Os atoms. The hydroxyl coverage of each hydroxyl type is closed to the result of the AIMD simulation. So within the timescale of the simulation, the ReaxFF is representing the protonation state of the (040) surface in good agreement with the AIMD simulation. The average total hydroxyl coverage at the steady state is $5.0 \pm 0.4\,\mathrm{HO/nm^2}$ for the AIMD simulation, and $5.13 \pm 0.07\,\mathrm{HO/nm^2}$ for the ReaxFF simulation. These values are also in agreement with previous investigation on C_3S hydration, using the ReaxFF [14, 149].

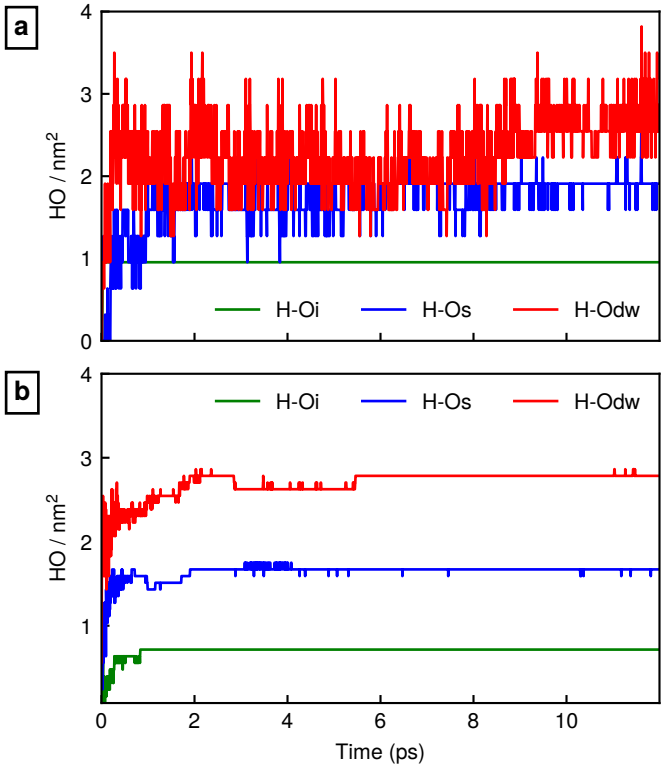

Figure 5.4. Number of hydroxyl groups formed at the surface on oxide ions (Oi-H), oxygen in silicates (Os-H), and from water dissociation (Odw-H) for (a) AIMD simulation, (b) ReaxFF simulation.

The atomic density profile of water oxygen and hydrogen atom, along the axis perpendicular to the surface, is reported in Figure 5.5. The layered structure of the interfacial water results from the effect of excluded volume, electrostatic force field, and hydrogen bonding network. Our previous investigation, based on classical MD simulations, showed that this layering is lost with protonation of the surface. The closest hydrogen's peak from the surface, is at the average position of oxygen in silicates Os ($z = 0$), and corresponds to chemisorbed H. The length of the layered region is approximately the same as in MD simulations (see Chapter 4): ~5 to 6 Å.

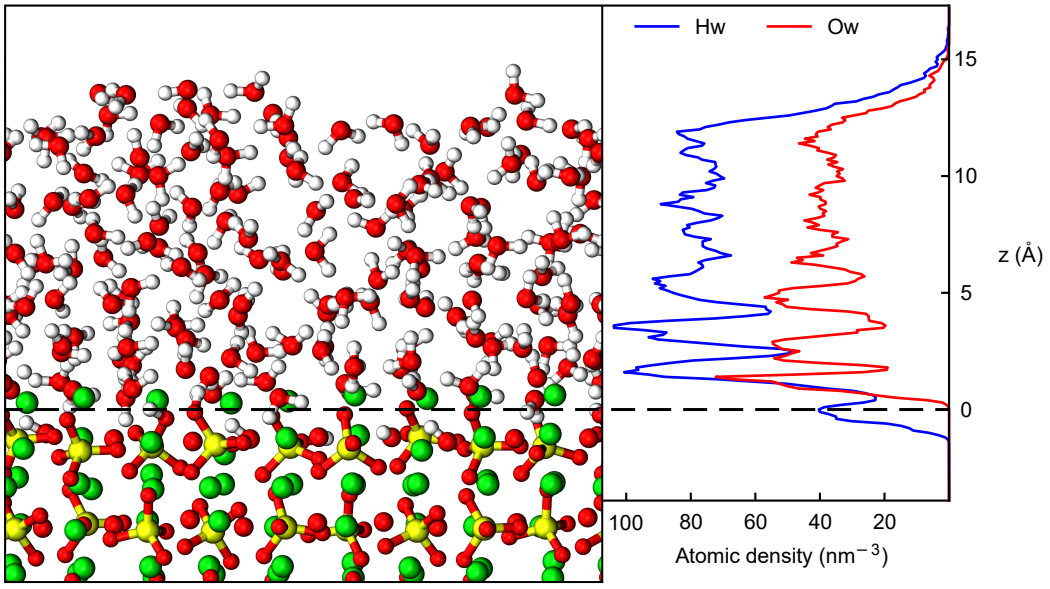

Figure 5.5. Atomic density profile of water molecules along the z axis for AIMD. The origin adopted is the average coordinate of the uppermost oxygen silicate layer. The layering observed results from the hydrogen bond network created between the strong interaction between the water molecules and the ionic surface.

The radial distribution functions (RDF) of H-Oi, H-Os and Ow-Ca pairs are plotted in Figure 5.6. For H-Oi and Ow-Ca pairs, a sharp first coordination peak raises at 0.97 Å and 2.50 Å

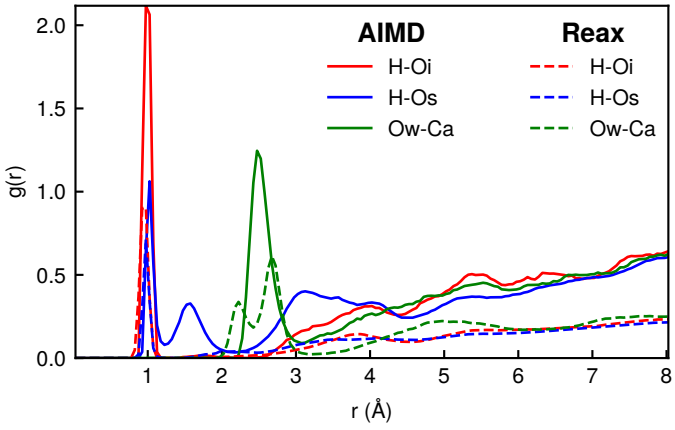

Figure 5.6. Radial distribution function H-Oi, H-Os, and Ow-Ca pairs for AIMD and ReaxFF simulations.

respectively, but no second coordination shell is noticed. As for the H-Os pairs, the first and second coordination peaks stand at 1.08 Å and 1.58 Å, respectively. The RDF obtained in the ReaxFF simulation are very similar, the differences being that only the first coordination shell H-Oi and H-Os pair is observed, and the first coordination peak for Ow-Ca pairs is split in two, traducing dissociation and solvation of Ca.

The orientation of water molecules in contact with the surface is a characteristic of the hydrophilic/hydrophobic behavior of the surface. The probability distribution of the angle θ between the water dipole moment and the z axis is depicted in Figure 5.7.

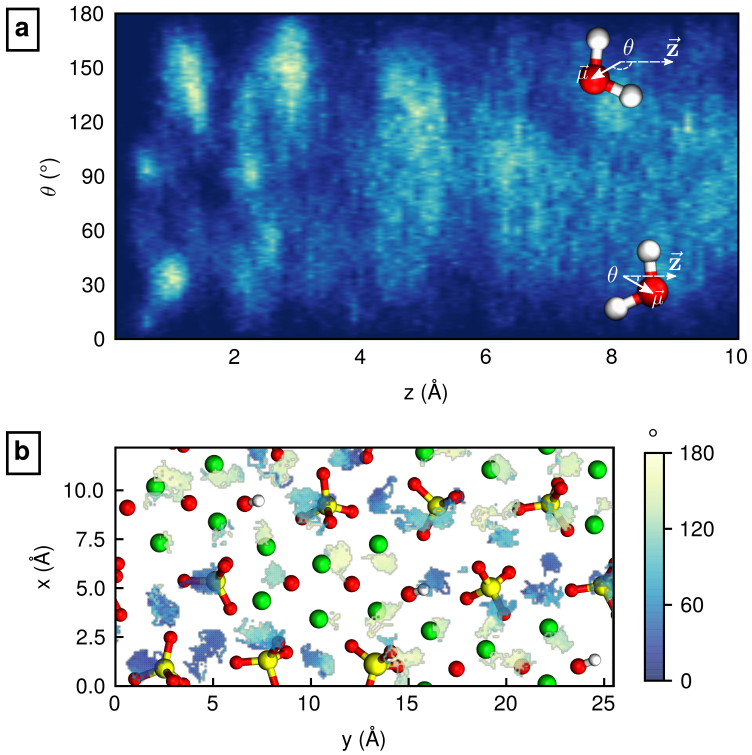

Figure 5.7. (a) Probability distribution of the angle θ between the water dipole moment and the z axis, perpendicular to the surface. Lighter regions correspond to higher probabilities (b) Density mapping of θ for water molecules within 3 Å from the surface. Color code: Ca in green, Os and Oi in red, Si in yellow, H in hydroxide H-Oi in white.

Within the contact layer, most of the water molecules have θ ~22–47° or θ ~115–170°, meaning that their dipole moments point preferentially towards or against the surface. This feature is characteristic of hydrophilic surfaces. The water molecules of the contact layer orientate according to the charge of the ionic species from the surface. Thus, two regions can be distinguished: one where the water dipole is oriented upward and H coordinate with Os, and a second where the water dipole is oriented downward and Ow coordinate with Ca. These regions are mapped on the surface in Figure 5.7 by collecting θ and the x and y coordinates of water molecules within 3 Å from the surface, during the whole simulation. The effect of the topology of C_3S surfaces on the structure of water molecules as already been reported in a previous molecular dynamics investigation [135]. The probability distribution of hydroxyl groups H-Os and H-Odw is plotted in Figure 5.8.

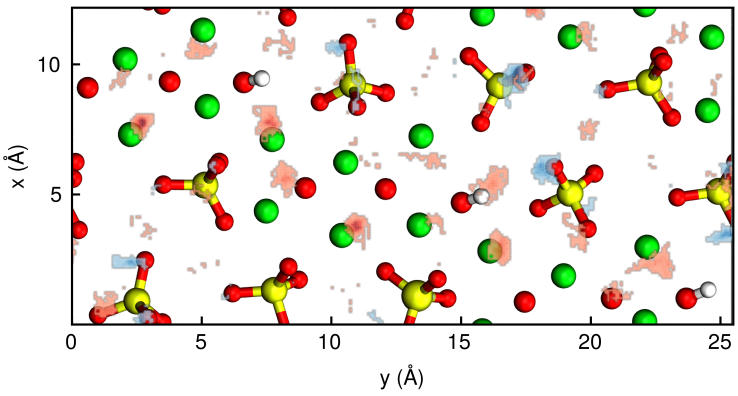

Figure 5.8. Normalized probability distribution of the H-Os (blue) and H-Odw groups (red).

H-Odw groups are principally located on Ca-rich, positively charged regions, but also close to protonated silicates.

5.2.2 Proton transfer analysis

The frequency of PT between water molecules and Os-H and Odw-H groups are reported in Figure 5.9. The plot on the right shows that proton hops start firstly between water and Odw-

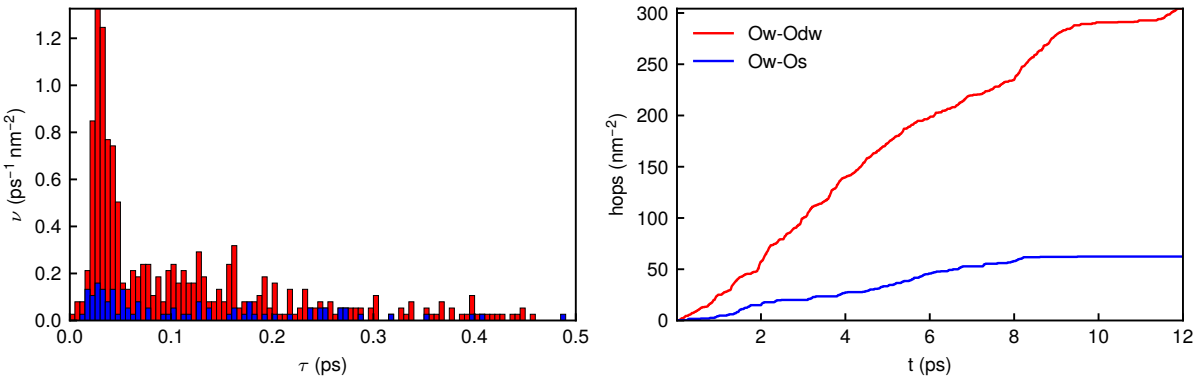

Figure 5.9. Frequency of PT as a function of its lifetime τ (left). Evolution of the total number of hops within the simulation time (right).

H groups. This is because the first Odw-H groups are formed when water dissociates to form Oi-H groups. The number of hops between Ow and Odw atoms increases more rapidly than between Ow and Os. The number of hops among Ow-Odw pairs seems to reach a plateau after 9 ps of simulation, and stabilize after 8 ps for Ow-Os pairs. The lifetime τ is defined as the time for a proton to return to the oxygen atoms to which it was initially bonded. The typical lifetime of PT events is shorter than 100 fs. This is the same time scale as Eigen-Zendel structure

interchanging in bulk water, obtained by femtosecond vibrational spectroscopy [163]. Lifetimes of approximately the same duration were reported for PT at water/ZnO($10\bar{1}0$) interface [151]. The longest lifetimes reported are ~0.2 ps for transfer between Ow and Os, and ~2 ps for transfer between Ow and Odw.

The free energy profiles of PT between Ow and Os and between Ow and Odw pairs were obtained from the standard histogram method as follows: $F = -k_B T \log P$ (see Figure 5.10).

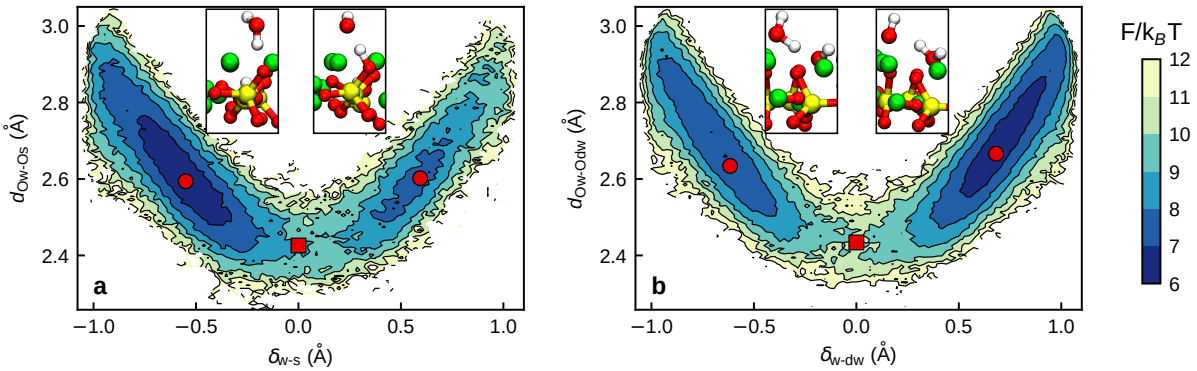

Figure 5.10. Free energy contour plot of PT between Ow and Os as a function of the distance $d_{\text{Oa-Ob}}$ between oxygen atoms, and of $\delta_{\text{a-b}} = d_{\text{Oa-H}} - d_{\text{Ob-H}}$. The red circles shows the local free energy minima, corresponding to the most stable configurations before and after the proton jump. The red square is the saddle point, where the proton is equidistant from both oxygen atoms.

P is a probability distribution function of the distance $d_{\text{Oa-Ob}}$ between two oxygen atoms Oa and Ob, and of $\delta_{\text{a-b}} = d_{\text{Oa-H}} - d_{\text{Ob-H}}$. In the case of PT between Ow and Os, the molecular configuration of water forming an H-bond with Os is more stable than the dissociative configuration. The free energy profile of PT between Ow and Odw suggests that the molecular adsorption of water on the surface is more stable than the dissociated form. This observation is contrary to previous DFT and reactive MD calculations on a single water molecule, where dissociative adsorption energies were generally larger than molecular adsorption energies, resulting in more stable configurations [14, 68, 69, 148]. This consolidates the idea that static calculations on single water molecule cannot describe accurately the properties of a solid/water interface. Tocci and Michaelides also reported considerable differences in PT rate between a monolayer and an thicker water film [151]. These differences arise from H-bond fluctuations, lowering the free energy barrier of proton transfers. The free energy barrier of PT is ~2.3 k_BT from Ow to Os and ~1.2 k_BT from Os to Ow. The barrier is ~2.7 k_BT for transfer from Ow to Odw and ~3.2 k_BT for the reverse reaction. Therefore, hydroxides formed by water dissocia-

tion are more stable than silanol groups (energy barrier ~2.6 time larger).

Electron density difference analysis allows to map the distribution of electrons involved in PT, and more generally in the adsorption. This analysis was realized performing static DFT calculation on the total system, as well as C_3S, and water independently on the system configuration at 5 ps. The electron density difference $\Delta\rho$ was calculated as follow:

$$\Delta\rho = \rho_{C_3S/H_2O} - \rho_{C_3S} - \rho_{H_2O} \tag{5.1}$$

where ρ_{C_3S/H_2O} corresponds to the electron density of the interface system, ρ_{C_3S} and ρ_{H_2O} are the electron density of the C_3S and water alone, respectively. A positive value of $\Delta\rho$ indicates a high electron density, while a negative value points out an electron depletion region.

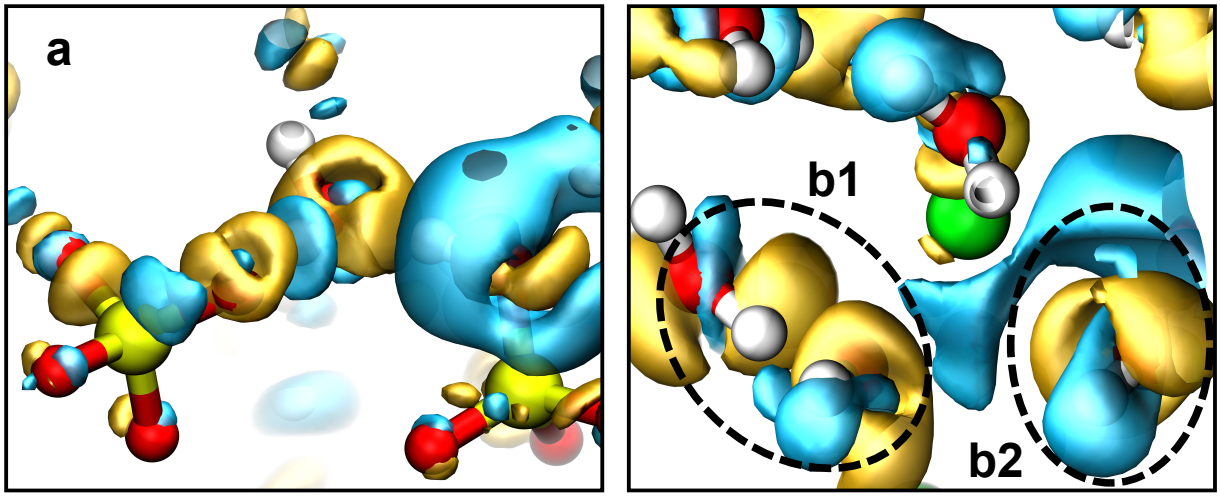

Figure 5.11. Snapshots of the isosurface of electron density difference. Orange and cyan isosurface represent positive and negative $\Delta\rho$, respectively. a) A water molecule between a silicate and a silanol group. b1) Electron density delocalization during a proton exchange between a molecular water and a hydroxide. b2) Electron abundance and depletion regions around an hydroxide created upon water dissociation.

The proton transfers occurring at the surface create an electron delocalization, and thus high and low electron density regions. Water molecules act as charge carrier and the electron depletion or gain highly depends on the location of the molecule (see Figure 5.11 a and b1). High electron density is observed around the silicate oxygen closed to the water molecule, creating a depletion region on the silicon atom. A large depletion region is observed around the silanol group (Figure 5.11 a). Charge depletion regions are observed around H of hydroxyl groups. Their magnitude increase in this order: H-Oi < H-Odw < H-Os. In other words, the

magnitude of the depletion regions on H decreases as a function of the stability of the hydroxyl group. A large depletion region indicates a greater charge separation, and a more ionic bond, while a small depletion region reveals a more covalent bond.

5.3 Conclusion

The very early hydration of the (040) surface of C_3S was investigated through a 12 ps AIMD simulation. As a first observation, only 1/3 of the oxide ions on the surface were protonated during the whole simulation. The hydroxides formed are highly stable and no proton exchange was observed. Although the oxide ion is very unstable in water, we found that its environment on the surface is an important factor for the creation of hydrogen bond with water molecules and for protonation to occur. Thus, the pKa of hydroxide and silicic acid in solution cannot predict accurately the protonation state of the surface during the very early hydration of C_3S. The structure of water at the interface, resulting from the hydrogen bond network, is very similar to that of our previous classical molecular dynamics study, with a length of layered region of approximately 5 to 6 Å from the surface. The (040) surface is composed of Ca-rich regions (positively charged) and Si-rich regions (negatively charged). Water molecules in the contact layer orient their dipole moment in accordance with the surface charge, making either H-bonds in Si-rich regions, or creating strong Ca-Ow interactions in Ca-rich regions. Energy barrier analysis suggests that the molecular adsorption of water on the C_3S surface is more stable than dissociative adsorption. Based on proton transfer energy analysis, the hydroxyl groups formed were classified in order of stability as follow: H-Oi > H-Odw > H-Os. From electron density difference, high electron density, and depletion regions were observed. These observations revealed that the magnitude of the electron depletion region upon adsorption is smaller for more stable hydroxyl groups.

General conclusion and perspectives

The present thesis has allowed to gain an insight on the mechanical and thermal properties of C_3S, as well as on its very early hydration. This work also presents different computational methods, from electronic density based to empirical ones. This allowed to estimate the abilities of atomistic simulations to describe the properties of C_3S, and to compare different models and computational methods.

The elastic constants of C_3S were computed using static optimization, EMD and NEMD. In agreement with a previous MD simulation study, we found that the ClayFF underestimates the stiffness and elastic constants. On the contrary, DFT calculation seems to overestimate these values. The accuracy of the results obtained by DFT could be confirmed including nanoscale and miscroscale porosity, and calculating the homogenized values. With respect to this issue, the values obtained by IFF are in very good agreement with experimental results,but are questionable if the porosity is considered. Moreover, the thermal properties were computed by direct method and by assessment of the VACF. Despite its robustness, the specific heat computed from direct method calculation had larger errors than with the VACF method. The cleavage energies obtained from MD calculation with the IFF are in relatively good agreement with previous study using the same FF. These results allowed to create the equilibrium shape of the M_1 and M_3 C_3S. The determined M_3 crystal consists of seven planes, while the M_1 consists on only three planes and is similar with the equilibrium shape of C_3S proposed by Maki [21], but with a larger rhombohedral face.

The influence of the degree of hydration of M_3 C_3S on the behavior of interfacial water was assessed by MD simulations on an incrementally protonated (040) surface, following a previously proposed hydration model. This investigation demonstrates that the hydrogen bond network initially created between the interfacial water molecules is weakened by the proto-

nation of the surface. One could expect an increase in translational motion of the interfacial water with the loss of interaction with the mineral surface. However, we showed that the dissociation of calcium cations decreases even more the translational motion. At high pH, when in contact with the dry surface, water molecules have dipole moments pointing preferentially away from the surface. Their rotational motion increase and become uniform after the first protonation of silicates. This chapter brings new information on the behavior of water at the interfaces during the hydration of minerals.

While classical MD cannot describe water dissociation and surface protonation, we have proposed to investigated these features by AIMD. Then, we undertook the study of the interface C_3S/water by AIMD, integrating DFT calculations in the equations of motion of the MD. This study made it possible to describe the dissociation reactions of water and protonation of the mineral surface. The importance of the environment of oxides ions on their early protonation was demonstrated. This means than pKa of solvated ions cannot describe accurately protonation reactions occurring at water/mineral interfaces. Also, this AIMD study showed that the (040) surface studied can be divided in two regions, positively and negatively charged, influencing the orientation of water molecules in the contact layer. Moreover, the free energy and frequency of proton transfer was quantified. Based on free energy analysis, the molecular adsorption of water molecule is more stable than dissociative adsorption. The method used to describe the configuration and energy of water adsorption is discussed. Static calculation method, especially on single or thin water film, does not account for H-bonds fluctuation, and thus cannot predict the actual adsorption configuration nor describe proton transfer properly.

In perspective, in a context of energy and ecological transition, new challenges are proposed to us in terms of knowledge and development of sustainable materials. For this, the modeling of civil engineering materials including biosourced additions is an important subject. More precisely, the main idea of such a study would be to assess through atomistic modeling the influence of additions on the mechanical and physical behavior of cementitious materials. Moreover, it seems really important to describe the hydration of C_3S at larger scale, and to make the bridge between atomistic mechanisms and microscopic processes. To this end, kinetic Monte Carlo simulation already allowed to model the hydration of alite and confirms the concept of etch pit driven dissolution [44]. This model includes a reversal process, where a precipitation can occur on the surface, but does not account for the importance of the proton

hopping mechanisms, responsible for the disruption of the bulk crystalline structure. A proposal for future investigation would be to calibrate a kMC model with rates of proton hopping occurring in the core of C_3S, after disordering, and loss of the surface properties. As another proposal for future investigation, the influence of impurities on C_3S hydration might also be taken into account. However, the optimization of force field parameters for MgO or SO_3 would be needed to provide an accurate description.

Bibliography

[1] R. M. Andrew. Global CO_2 emissions from cement production. *Earth System Science Data*, 10(1):195–217, 2018.

[2] T. Boden, R. Andres, and G. Marland. Global, Regional, and National Fossil-Fuel CO2 Emissions (1751 - 2014) (V. 2017), 2017.

[3] I. E. Agency. *Energy Technology Perspectives 2016*. OECD, 2016.

[4] K. L. Scrivener, P. Juilland, and P. J. M. Monteiro. Advances in understanding hydration of Portland cement. *Cement and Concrete Research*, 78:38–56, 2015.

[5] K. L. Scrivener and R. J. Kirkpatrick. Innovation in use and research on cementitious material. *Cement and Concrete Research*, 38(2):128–136, 2008.

[6] J. W. Bullard, H. M. Jennings, R. A. Livingston, A. Nonat, G. W. Scherer, J. S. Schweitzer, K. L. Scrivener, and J. J. Thomas. Mechanisms of cement hydration. *Cement and Concrete Research*, 41(12):1208–1223, 2011.

[7] K. Scrivener, A. Ouzia, P. Juilland, and A. K. Mohamed. Advances in understanding cement hydration mechanisms. *Cement and Concrete Research*, 124:105823, 2019.

[8] L. Nicoleau and A. Nonat. A new view on the kinetics of tricalcium silicate hydration. *Cement and Concrete Research*, 86:1–11, 2016.

[9] K. L. Scrivener and A. Nonat. Hydration of cementitious materials, present and future. *Cement and Concrete Research*, 41(7):651–665, 2011.

[10] J. J. Thomas, J. J. Biernacki, J. W. Bullard, S. Bishnoi, J. S. Dolado, G. W. Scherer, and A. Lüttge. Modeling and simulation of cement hydration kinetics and microstructure development. *Cement and Concrete Research*, 41(12):1257–1278, 2011.

[11] P. Juilland, E. Gallucci, R. Flatt, and K. Scrivener. Dissolution theory applied to the induction period in alite hydration. *Cement and Concrete Research*, 40(6):831–844, 2010.

[12] H. F. W. Taylor, P. Barret, P. W. Brown, D. D. Double, G. Frohnsdorff, V. Johansen, D. Ménétrier-Sorrentino, I. Odler, L. J. Parrott, J. M. Pommersheim, M. Regourd, and J. F. Young. The hydration of tricalcium silicate. *Materials and Structures*, 17(6):457–468, 1984.

[13] R. K. Mishra, D. Geissbuhler, H. A. Carmona, F. K. Wittel, M. L. Sawley, M. Weibel, E. Gallucci, H. J. Herrmann, H. Heinz, and R. J. Flatt. En route to multi-model scheme for clinker comminution with chemical grinding aids. *Advances in Applied Ceramics*, 114:393–401, 2015.

[14] H. Manzano, E. Durgun, I. López-Arbeloa, and J. C. Grossman. Insight on Tricalcium Silicate Hydration and Dissolution Mechanism from Molecular Simulations. *ACS Applied Materials & Interfaces*, 7(27):14726–14733, 2015.

[15] I. Shvab, L. Brochard, H. Manzano, and E. Masoero. Precipitation Mechanisms of Mesoporous Nanoparticle Aggregates: Off-Lattice, Coarse-Grained, Kinetic Simulations. *Crystal Growth & Design*, 17(3):1316–1327, 2017.

[16] H. F. W. Taylor. *Cement Chemistry*. Academic Pr, 1990.

[17] E. Durgun, H. Manzano, R. J. M. Pellenq, and J. C. Grossman. Understanding and Controlling the Reactivity of the Calcium Silicate phases from First Principles. *Chemistry of Materials*, 24(7):1262–1267, 2012.

[18] M. Laanaiya, A. Bouibes, and A. Zaoui. Understanding why Alite is responsible of the main mechanical characteristics in Portland cement. *Cement and Concrete Research*, 126:105916, 2019.

[19] P. Hewlett. *Lea's Chemistry of Cement and Concrete*. Butterworth-Heinemann, 2003.

[20] M. Bigaré, A. Guinier, C. Mazières, M. Regourd, N. Yannaquis, W. Eysel, T. Hanh, and E. Woermann. Polymorphism of Tricalcium Silicate and Its Solid Solutions. *Journal of the American Ceramic Society*, 50(11):609–619, 1967.

[21] I. Maki. Relationship of processing parameters to clinker properties; influence of minor components. In *Proceedings of the 8th International Congress on the Chemistry of Cement*, volume 1, pages 34–47, 1986.

[22] A. Guinier and M. Regourd. Structure of Portland Cement Minerals. In *5th Symposium on the Chemistry of Cement*, volume 1, pages 1–41, 1969.

[23] G. Yamaguchi and S. Takagi. Analysis of Portland cement clinker. In *5th Symposium on the Chemistry of Cement*, 1969.

[24] M. Regourd and A. Guinier. Cristallochimie des constituants du clinker de ciment Portland. In *6th International Congress on the Chemistry of Cement*, 1974.

[25] I. Maki and S. Chromý. Microscopic study on the polymorphism of Ca3SiO5. *Cement and Concrete Research*, 8(4):407–414, 1978.

[26] I. Maki and K. Kato. Phase identification of alite in portland cement clinker. *Cement and Concrete Research*, 12(1):93–100, 1982.

[27] I. Maki and S. Takahashi. Redistribution of impurity during recrystallization of alite in portland cement clinker. *Cement and Concrete Research*, 14(3):413–418, 1984.

[28] I. Maki and K. Goto. Factors influencing the phase constitution of alite in portland cement clinker. *Cement and Concrete Research*, 12(3):301–308, 1982.

[29] H. Zhou, X. Gu, J. Sun, Z. Yu, H. Huang, Q. Wang, and X. Shen. Research on the formation of M1-type alite doped with MgO and SO_3 —A route to improve the quality of cement clinker with a high content of MgO. *Construction and Building Materials*, 182:156–166, 2018.

[30] J. W. Jeffery. The crystal structure of tricalcium silicate. *Acta Crystallographica*, 5(1):26–35, 1952.

[31] A. M. Il'inets, Y. Malinovskii, and N. N. Nevskii. Crystal Structure of the Rhombohedral Modification of Tricalcium Silicate Ca_3SiO_5. *Doklady Akademii Nauk*, 281:332–336, 1985.

[32] F. Nishi and Y. Takéuchi. The rhombohedral structure of tricalcium silicate at 1200 °C. *Zeitschrift für Kristallographie - Crystalline Materials*, 168(1-4):197–212, 1984.

[33] F. Nishi, Y. Takeuchi, and I. Maki. Tricalcium Silicate $Ca_3O[SiO_4]$: The monoclinic superstructure. *Zeitschrift für Kristallographie - Crystalline Materials*, 172(1-4):297–314, 1985.

[34] W. G. Mumme. Crystal structure of tricalcium silicate from a Portland cement clinker and its application to quantitative XRD analysis. *Neues Jahrbuch fuer Mineralogie: Monatshefte*, 4:145–160, 1995.

[35] Á. G. D. L. Torre, S. Bruque, J. Campo, and M. A. G. Aranda. The superstructure of C_3S from synchrotron and neutron powder diffraction and its role in quantitative phase analyses. *Cement and Concrete Research*, 32(9):1347–1356, 2002.

[36] M.-N. D. Noirfontaine, M. Courtial, F. Dunstetter, G. Gasecki, and M. Signes-Frehel. Tricalcium silicate Ca3SiO5 superstructure analysis: a route towards the structure of the M1 polymorph. *Zeitschrift für Kristallographie*, 227(2):102–112, 2012.

[37] Ángeles G. De la Torre, R. N. D. Vera, A. J. M. Cuberos, and M. A. G. Aranda. Crystal structure of low magnesium-content alite: Application to Rietveld quantitative phase analysis. *Cement and Concrete Research*, 38(11):1261 – 1269, 2008.

[38] N. I. Golovastikov, R. G. Matveeva, and N. V. Belov. Crystal structure of the tricalcium silicate $(CaOSiO_2)_3$=C_3S. *Kristallografiya*, 20:721–729, 1975.

[39] L. Nicoleau and M. A. Bertolim. Analytical Model for the Alite (C_3S) Dissolution Topography. *Journal of the American Ceramic Society*, 99(3):773–786, 2015.

[40] M. Wolthers, D. D. Tommaso, Z. Du, and N. H. de Leeuw. Calcite surface structure and reactivity: molecular dynamics simulations and macroscopic surface modelling of the calcite–water interface. *Physical Chemistry Chemical Physics*, 14(43):15145, 2012.

[41] M. Wolthers, D. D. Tommaso, Z. Du, and N. H. de Leeuw. Variations in calcite growth kinetics with surface topography: molecular dynamics simulations and process-based growth kinetics modelling. *CrystEngComm*, 15(27):5506, 2013.

[42] E. Masoero. Mesoscale mechanisms of cement hydration: BNG model and particle simulations. In *Handbook of Materials Modeling*. Springer International Publishing, 2018.

[43] L. Briese, R. S. Arvidson, and A. Lüttge. The effect of crystal size variation on the rate of dissolution – A kinetic Monte Carlo study. *Geochimica et Cosmochimica Acta*, 212:167–175, 2017.

[44] P. Martin, H. Manzano, and J. S. Dolado. Mechanisms and Dynamics of Mineral Dissolution: A New Kinetic Monte Carlo Model. *Advanced Theory and Simulations*, 2(10):1900114, 2019.

[45] J. S. Dolado, M. Griebel, and J. Hamaekers. A Molecular Dynamic Study of Cementitious Calcium Silicate Hydrate (C-S-H) Gels. *Journal of the American Ceramic Society*, 0(0):070915225431002–???, 2007.

[46] H. Manzano, S. Moeini, F. Marinelli, A. C. T. van Duin, F.-J. Ulm, and R. J.-M. Pellenq. Confined Water Dissociation in Microporous Defective Silicates: Mechanism, Dipole Distribution, and Impact on Substrate Properties. *Journal of the American Chemical Society*, 134(4):2208–2215, 2012.

[47] R. J.-M. Pellenq, A. Kushima, R. Shahsavari, K. J. V. Vliet, M. J. Buehler, S. Yip, and F.-J. Ulm. A realistic molecular model of cement hydrates. *Proceedings of the National Academy of Sciences*, 106(38):16102–16107, 2009.

[48] M. J. A. Qomi, M. Bauchy, F.-J. Ulm, and R. J.-M. Pellenq. Anomalous composition-dependent dynamics of nanoconfined water in the interlayer of disordered calcium-silicates. *The Journal of Chemical Physics*, 140(5):054515, 2014.

[49] M. Bauchy, M. J. A. Qomi, F.-J. Ulm, and R. J.-M. Pellenq. Order and disorder in calcium–silicate–hydrate. *The Journal of Chemical Physics*, 140(21):214503, 2014.

[50] A. Lushnikova and A. Zaoui. Improving mechanical properties of C-S-H from inserted carbon nanotubes. *Journal of Physics and Chemistry of Solids*, 105:72–80, 2017.

[51] J. Fu, F. Bernard, and S. Kamali-Bernard. Assessment of the elastic properties of amorphous calcium silicates hydrates (I) and (II) structures by molecular dynamics simulation. *Molecular Simulation*, 39:1–15, 2017.

[52] J. Yang, D. Hou, and Q. Ding. Ionic hydration structure, dynamics and adsorption mechanism of sulfate and sodium ions in the surface of calcium silicate hydrate gel: A molecular dynamics study. *Applied Surface Science*, 448:559–570, 2018.

[53] A. Zaoui. Insight into elastic behavior of calcium silicate hydrated oxide (C–S–H) under pressure and composition effect. *Cement and Concrete Research*, 42(2):306–312, 2012.

[54] S. M. Mutisya, J. M. de Almeida, and C. R. Miranda. Molecular simulations of cement based materials: A comparison between first principles and classical force field calculations. *Computational Materials Science*, 138:392–402, 2017.

[55] S. M. Mutisya and C. R. Miranda. The surface stability and morphology of tobermorite 11 Å from first principles. *Applied Surface Science*, 444:287–292, 2018.

[56] S. Galmarini, A. Aimable, N. Ruffray, and P. Bowen. Changes in portlandite morphology with solvent composition: Atomistic simulations and experiment. *Cement and Concrete Research*, 41(12):1330–1338, 2011.

[57] S. Galmarini, A. K. Mohamed, and P. Bowen. Atomistic Simulations of Silicate Species Interaction with Portlandite Surfaces. *The Journal of Physical Chemistry C*, 120(39):22407–22413, 2016.

[58] S. Galmarini and P. Bowen. Atomistic simulation of the adsorption of calcium and hydroxyl ions onto portlandite surfaces — towards crystal growth mechanisms. *Cement and Concrete Research*, 81:16–23, 2016.

[59] H. Manzano, R. J. M. Pellenq, F.-J. Ulm, M. J. Buehler, and A. C. T. van Duin. Hydration of Calcium Oxide Surface Predicted by Reactive Force Field Molecular Dynamics. *Langmuir*, 28(9):4187–4197, 2012.

[60] J. Fu, F. Bernard, and S. Kamali-Bernard. First-principles calculations of typical anisotropic cubic and hexagonal structures and homogenized moduli estimation based on the Y-parameter: Application to CaO, MgO, CH and Calcite $CaCO_3$. *Journal of Physics and Chemistry of Solids*, 101:74–89, 2017.

[61] R. Shahsavari and L. Chen. Screw Dislocations in Complex, Low Symmetry Oxides: Core Structures, Energetics, and Impact on Crystal Growth. *ACS Applied Materials & Interfaces*, 7(4):2223–2234, 2015.

[62] R. Shahsavari, L. Tao, and L. Chen. Structure, Energetics, and Impact of Screw Dislocations in Tricalcium Silicates. *Journal of the American Ceramic Society*, 99(7):2512–2520, 2016.

[63] Q. Wang, H. Manzano, Y. Guo, I. Lopez-Arbeloa, and X. Shen. Hydration Mechanism of Reactive and Passive Dicalcium Silicate Polymorphs from Molecular Simulations. *The Journal of Physical Chemistry C*, 119(34):19869–19875, 2015.

[64] R. K. Mishra, R. J. Flatt, and H. Heinz. Force Field for Tricalcium Silicate and Insight into Nanoscale Properties: Cleavage, Initial Hydration, and Adsorption of Organic Molecules. *The Journal of Physical Chemistry C*, 117(20):10417–10432, 2013.

[65] Y. Zhang, X. Lu, Z. He, and D. Song. Molecular and dissociative adsorption of a single water molecule on a β-dicalcium silicate (100) surface explored by a DFT approach. *Journal of the American Ceramic Society*, 2017.

[66] H. Zhao, Y. Wang, Y. Yang, X. Shu, H. Yan, and Q. Ran. Effect of hydrophobic groups on the adsorption conformation of modified polycarboxylate superplasticizer investigated by molecular dynamics simulation. *Applied Surface Science*, 407:8–15, 2017.

[67] D. Tavakoli and A. Tarighat. Molecular dynamics study on the mechanical properties of Portland cement clinker phases. *Computational Materials Science*, 119:65–73, 2016.

[68] Y. Zhang, X. Lu, D. Song, and S. Liu. The adsorption behavior of a single and multi-water molecules on tricalcium silicate (111) surface from DFT calculations. *Journal of the American Ceramic Society*, 2018.

[69] Y. Zhang, X. Lu, D. Song, and S. Liu. The adsorption of a single water molecule on low-index C_3S surfaces: A DFT approach. *Applied Surface Science*, 471:658–663, 2019.

[70] R. K. Mishra, A. K. Mohamed, D. Geissbühler, H. Manzano, T. Jamil, R. Shahsavari, A. G. Kalinichev, S. Galmarini, L. Tao, H. Heinz, R. Pellenq, A. C. T. van Duin, S. C. Parker, R. J. Flatt, and P. Bowen. cemff : A force field database for cementitious materials including validations, applications and opportunities. *Cement and Concrete Research*, 102:68–89, 2017.

[71] E. Pustovgar, R. K. Mishra, M. Palacios, J.-B. d'Espinose de Lacaillerie, T. Matschei, A. S. Andreev, H. Heinz, R. Verel, and R. J. Flatt. Influence of aluminates on the hydration kinetics of tricalcium silicate. *Cement and Concrete Research*, 100:245–262, 2017.

[72] H. Heinz, T.-J. Lin, R. K. Mishra, and F. S. Emami. Thermodynamically Consistent Force Fields for the Assembly of Inorganic, Organic, and Biological Nanostructures: The INTERFACE Force Field. *Langmuir*, 29(6):1754–1765, 2013.

[73] R. T. Cygan, J.-J. Liang, and A. G. Kalinichev. Molecular Models of Hydroxide, Oxyhydroxide, and Clay Phases and the Development of a General Force Field. *The Journal of Physical Chemistry B*, 108(4):1255–1266, 2004.

[74] A. C. T. van Duin, S. Dasgupta, F. Lorant, and W. A. Goddard. ReaxFF: A Reactive Force Field for Hydrocarbons. *The Journal of Physical Chemistry A*, 105(41):9396–9409, 2001.

[75] L. Wang, D. Hou, H. Shang, and T. Zhao. Molecular dynamics study on the Tri-calcium silicate hydration in sodium sulfate solution: Interface structure, dynamics and dissolution mechanism. *Construction and Building Materials*, 170:402–417, 2018.

[76] E. Schrödinger. An Undulatory Theory of the Mechanics of Atoms and Molecules. *Physical Review*, 28:1049–1070, 1926.

[77] W. Koch and M. C. Holthausen. *A Chemist's Guide to Density Functional Theory*. Wiley-VCH, 2001.

[78] M. Born and R. Oppenheimer. Zur Quantentheorie der Molekeln. *Annalen der Physik*, 389:457–484, 1927.

[79] P. Hohenberg and W. Kohn. Inhomogeneous Electron Gas. *Physical Review*, 136(3B):B864–B871, 1964.

[80] B. S. Daan Frenkel. *Understanding Molecular Simulation*. Elsevier LTD, Oxford, 2001.

[81] A. R. Leach. *Molecular Modelling*. Prentice Hall, 2001.

[82] E. Polak and G. Ribière. Note sur la convergence de méthodes de directions conjuguées. *Revue française d'informatique et de recherche opérationnelle. Série rouge*, 3:35–43, 1969.

[83] S. Nosé. A unified formulation of the constant temperature molecular dynamics methods. *The Journal of Chemical Physics*, 81(1):511–519, 1984.

[84] W. G. Hoover. Canonical dynamics: Equilibrium phase-space distributions. *Physical Review A*, 31:1695–1697, 1985.

[85] R. K. Mishra, L. Fernández-Carrasco, R. J. Flatt, and H. Heinz. A force field for tricalcium aluminate to characterize surface properties, initial hydration, and organically modified interfaces in atomic resolution. *Dalton Trans.*, 43(27):10602–10616, 2014.

[86] T. R. Zeitler, J. A. Greathouse, R. T. Cygan, J. T. Fredrich, and G. R. Jerauld. Molecular Dynamics Simulation of Resin Adsorption at Kaolinite Edge Sites: Effect of Surface Deprotonation on Interfacial Structure. *The Journal of Physical Chemistry C*, 121(41):22787–22796, 2017.

[87] A. G. Kalinichev, J. Wang, and R. J. Kirkpatrick. Molecular dynamics modeling of the structure, dynamics and energetics of mineral–water interfaces: Application to cement materials. *Cement and Concrete Research*, 37(3):337–347, 2007.

[88] I. Androniuk, C. Landesman, P. Henocq, and A. G. Kalinichev. Adsorption of gluconate and uranyl on C-S-H phases: Combination of wet chemistry experiments and molecular dynamics simulations for the binary systems. *Physics and Chemistry of the Earth, Parts A/B/C*, 99:194–203, 2017.

[89] A. G. Kalinichev and R. J. Kirkpatrick. Molecular Dynamics Modeling of Chloride Binding to the Surfaces of Calcium Hydroxide, Hydrated Calcium Aluminate, and Calcium Silicate Phases. *Chemistry of Materials*, 14(8):3539–3549, 2002.

[90] K. D. Nielson, A. C. T. van Duin, J. Oxgaard, W.-Q. Deng, and W. A. Goddard. Development of the ReaxFF Reactive Force Field for Describing Transition Metal Catalyzed Reactions, with Application to the Initial Stages of the Catalytic Formation of Carbon Nanotubes. *The Journal of Physical Chemistry A*, 109(3):493–499, 2005.

[91] T. P. Senftle, S. Hong, M. M. Islam, S. B. Kylasa, Y. Zheng, Y. K. Shin, C. Junkermeier, R. Engel-Herbert, M. J. Janik, H. M. Aktulga, T. Verstraelen, A. Grama, and A. C. T. van Duin. The ReaxFF reactive force-field: development, applications and future directions. *npj Computational Materials*, 2, 2016.

[92] W. J. Mortier, S. K. Ghosh, and S. Shankar. Electronegativity-equalization method for the calculation of atomic charges in molecules. *Journal of the American Chemical Society*, 108(15):4315–4320, 1986.

[93] A. K. Rappe and W. A. Goddard. Charge equilibration for molecular dynamics simulations. *The Journal of Physical Chemistry*, 95(8):3358–3363, 1991.

[94] J. C. Fogarty, H. M. Aktulga, A. Y. Grama, A. C. T. van Duin, and S. A. Pandit. A reactive molecular dynamics simulation of the silica-water interface. *The Journal of Chemical Physics*, 132(17):174704, 2010.

[95] J. E. Ash, M. G. Hall, J. I. Langford, and M. Mellas. Estimations of degree of hydration of portland cement pastes. *Cement and Concrete Research*, 23(2):399–406, 1993.

[96] M. Vandamme, F.-J. Ulm, and P. Fonollosa. Nanogranular packing of C–S–H at substochiometric conditions. *Cement and Concrete Research*, 40(1):14–26, 2010.

[97] R. Tran, Z. Xu, B. Radhakrishnan, D. Winston, W. Sun, K. A. Persson, and S. P. Ong. Surface energies of elemental crystals. *Scientific Data*, 3:160080, 2016.

[98] H. Manzano, E. Durgun, M. J. A. Qomi, F.-J. Ulm, R. J. M. Pellenq, and J. C. Grossman. Impact of Chemical Impurities on the Crystalline Cement Clinker Phases Determined by Atomistic Simulations. *Crystal Growth & Design*, 11(7):2964–2972, 2011.

[99] L. Nicoleau, A. Nonat, and D. Perrey. The di- and tricalcium silicate dissolutions. *Cement and Concrete Research*, 47:14–30, 2013.

[100] K. Velez, S. Maximilien, D. Damidot, G. Fantozzi, and F. Sorrentino. Determination by nanoindentation of elastic modulus and hardness of pure constituents of Portland cement clinker. *Cement and Concrete Research*, 31(4):555–561, 2001.

[101] L. Brunarski. Recommendations for the use of resonance methods for testing concrete. *Matériaux et Constructions*, 2(4):269–273, 1969.

[102] X. Gao, Y. Wei, and W. Huang. Effect of individual phases on multiscale modeling mechanical properties of hardened cement paste. *Construction and Building Materials*, 153:25–35, 2017.

[103] F.-J. Ulm, M. Vandamme, C. Bobko, J. A. Ortega, K. Tai, and C. Ortiz. Statistical Indentation Techniques for Hydrated Nanocomposites: Concrete, Bone, and Shale. *Journal of the American Ceramic Society*, 90(9):2677–2692, 2007.

[104] H. Manzano, J. S. Dolado, and A. Ayuela. Elastic properties of the main species present in Portland cement pastes. *Acta Materialia*, 57(5):1666–1674, 2009.

[105] M. J. A. Qomi, D. Ebrahimi, M. Bauchy, R. Pellenq, and F.-J. Ulm. Methodology for Estimation of Nanoscale Hardness via Atomistic Simulations. *Journal of Nanomechanics and Micromechanics*, 7(4):04017011, 2017.

[106] M. Parrinello and A. Rahman. Polymorphic transitions in single crystals: A new molecular dynamics method. *Journal of Applied Physics*, 52(12):7182–7190, 1981.

[107] S. Plimpton. Fast Parallel Algorithms for Short-Range Molecular Dynamics. *Journal of Computational Physics*, 117(1):1–19, 1995.

[108] P. Giannozzi, S. Baroni, N. Bonini, M. Calandra, R. Car, C. Cavazzoni, D. Ceresoli, G. L. Chiarotti, M. Cococcioni, I. Dabo, A. D. Corso, S. de Gironcoli, S. Fabris, G. Fratesi, R. Gebauer, U. Gerstmann, C. Gougoussis, A. Kokalj, M. Lazzeri, L. Martin-Samos, N. Marzari, F. Mauri, R. Mazzarello, S. Paolini, A. Pasquarello, L. Paulatto, C. Sbraccia, S. Scandolo, G. Sclauzero, A. P. Seitsonen, A. Smogunov, P. Umari, and R. M. Wentzcovitch. QUANTUM ESPRESSO: a modular and open-source software project for quantum simulations of materials. *Journal of Physics: Condensed Matter*, 21(39):395502, 2009.

[109] P. Giannozzi, O. Andreussi, T. Brumme, O. Bunau, M. B. Nardelli, M. Calandra, R. Car, C. Cavazzoni, D. Ceresoli, M. Cococcioni, N. Colonna, I. Carnimeo, A. D. Corso, S. de Gironcoli, P. Delugas, R. A. DiStasio, A. Ferretti, A. Floris, G. Fratesi, G. Fugallo, R. Gebauer, U. Gerstmann, F. Giustino, T. Gorni, J. Jia, M. Kawamura, H.-Y. Ko, A. Kokalj, E. Küçükbenli, M. Lazzeri, M. Marsili, N. Marzari, F. Mauri, N. L. Nguyen, H.-V. Nguyen, A. O. de-la Roza, L. Paulatto, S. Poncé, D. Rocca, R. Sabatini, B. Santra, M. Schlipf, A. P. Seitsonen, A. Smogunov, I. Timrov, T. Thonhauser, P. Umari, N. Vast, X. Wu, and S. Baroni. Advanced capabilities for materials modelling with Quantum ESPRESSO. *Journal of Physics: Condensed Matter*, 29(46):465901, 2017.

[110] Z. jian Wu, E. jun Zhao, H. ping Xiang, X. feng Hao, X. juan Liu, and J. Meng. Crystal structures and elastic properties of superhard IrN_2 and IrN_3 from first principles. *Physical Review B*, 76(5), 2007.

[111] A. Boumiz, D. Sorrentino, C. Vernet, and F. C. Tenoudji. Modelling the development of the elastic moduli as a function of the hydration degree of cement pastes and mortars.

In A. Nonat, editor, *Second International RILEM Symposium on Hydration and Setting*, pages 295–316. RILEM Publications SARL, 1997.

[112] R. M. Elder, D. B. Knorr, J. W. Andzelm, J. L. Lenhart, and T. W. Sirk. Nanovoid formation and mechanics: a comparison of poly(dicyclopentadiene) and epoxy networks from molecular dynamics simulations. *Soft Matter*, 12(19):4418–4434, 2016.

[113] S. L. Teich-McGoldrick, J. A. Greathouse, and R. T. Cygan. Molecular Dynamics Simulations of Structural and Mechanical Properties of Muscovite: Pressure and Temperature Effects. *The Journal of Physical Chemistry C*, 116(28):15099–15107, 2012.

[114] R. Gaillac, P. Pullumbi, and F.-X. Coudert. ELATE: an open-source online application for analysis and visualization of elastic tensors. *Journal of Physics: Condensed Matter*, 28(27):275201, 2016.

[115] G. G. Almeida, A. Borges, and J. M. Cordeiro. On the hydrogen bonding between N-methylformamide and acetone and tetrahydrofuran. *Chemical Physics*, 434:25–29, 2014.

[116] G. G. Almeida, J. M. M. Cordeiro, M. E. Martín, and M. A. Aguilar. Conformational Changes of the Alanine Dipeptide in Water–Ethanol Binary Mixtures. *Journal of Chemical Theory and Computation*, 12(4):1514–1524, 2016.

[117] J. M. M. Cordeiro and A. K. Soper. A hybrid neutron diffraction and computer simulation study on the solvation of N-methylformamide in dimethylsulfoxide. *The Journal of Chemical Physics*, 138(4):044502, 2013.

[118] J. M. Cordeiro and A. K. Soper. Investigation on the structure of liquid N-methylformamide–dimethylsulfoxide mixtures. *Chemical Physics*, 381(1-3):21–28, 2011.

[119] P. Atkins and J. de Paula. *Physical Chemistry, 9th Edition*. W. H. Freeman, 2009.

[120] J. Hickman and Y. Mishin. Temperature fluctuations in canonical systems: Insights from molecular dynamics simulations. *Physical Review B*, 94(18), 2016.

[121] Q. Wang, D. J. Keffer, S. Petrovan, and J. B. Thomas. Molecular Dynamics Simulation of Poly(ethylene terephthalate) Oligomers. *The Journal of Physical Chemistry B*, 114(2):786–795, 2010.

[122] M. J. A. Qomi, F.-J. Ulm, and R. J.-M. Pellenq. Physical Origins of Thermal Properties of Cement Paste. *Physical Review Applied*, 3(6), 2015.

[123] E. Durgun, H. Manzano, P. V. Kumar, and J. C. Grossman. The Characterization, Stability, and Reactivity of Synthetic Calcium Silicate Surfaces from First Principles. *The Journal of Physical Chemistry C*, 118(28):15214–15219, 2014.

[124] T. L. Hughes, C. M. Methven, T. G. J. Jones, S. E. Pelham, P. Fletcher, and C. Hall. Determining cement composition by Fourier transform infrared spectroscopy. *Advanced Cement Based Materials*, 2(3):91–104, 1995.

[125] P. Yu, R. J. Kirkpatrick, B. Poe, P. F. McMillan, and X. Cong. Structure of Calcium Silicate Hydrate (C-S-H): Near-, Mid-, and Far-Infrared Spectroscopy. *Journal of the American Ceramic Society*, 82(3):742–748, 2004.

[126] T. Matschei, B. Lothenbach, and F. P. Glasser. Thermodynamic properties of Portland cement hydrates in the system $CaO–Al_2O_3–SiO_2–CaSO_4–CaCO_3–H_2O$. *Cement and Concrete Research*, 37(10):1379–1410, 2007.

[127] S. S. Todd. Low-temperature Heat Capacities and Entropies at 298.16°K of Crystalline Calcium Orthosilicate, Zinc Orthosilicate and Tricalcium Silicate. *Journal of the American Chemical Society*, 73(7):3277–3278, 1951.

[128] P. W. Tasker. The stability of ionic crystal surfaces. *Journal of Physics C: Solid State Physics*, 12(22):4977–4984, 1979.

[129] C. Noguera. Polar oxide surfaces. *Journal of Physics: Condensed Matter*, 12(31):R367–R410, 2000.

[130] A. K. Ivanov-Schitz and G. N. Mazo. Atomistic Simulation of Interfaces in Materials of Solid State Ionics. *Crystallography Reports*, 63(1):1–25, 2018.

[131] W. Sun and G. Ceder. Efficient creation and convergence of surface slabs. *Surface Science*, 617:53–59, 2013.

[132] V. Fiorentini and M. Methfessel. Extracting convergent surface energies from slab calculations. *Journal of Physics: Condensed Matter*, 8, 1996.

[133] Y.-T. Fu and H. Heinz. Cleavage Energy of Alkylammonium-Modified Montmorillonite and Relation to Exfoliation in Nanocomposites: Influence of Cation Density, Head Group Structure, and Chain Length. *Chemistry of Materials*, 22(4):1595–1605, 2010.

[134] S. P. Ong, W. D. Richards, A. Jain, G. Hautier, M. Kocher, S. Cholia, D. Gunter, V. L. Chevrier, K. A. Persson, and G. Ceder. Python Materials Genomics (pymatgen): A robust, open-source python library for materials analysis. *Computational Materials Science*, 68:314–319, 2013.

[135] A. Alex, A. K. Nagesh, and P. Ghosh. Surface dissimilarity affects critical distance of influence for confined water. *RSC Adv.*, 7(6):3573–3584, 2017.

[136] T. Q. Vo and B. Kim. Transport Phenomena of Water in Molecular Fluidic Channels. *Scientific Reports*, 6(1), 2016.

[137] W. Humphrey, A. Dalke, and K. Schulten. VMD: Visual molecular dynamics. *Journal of Molecular Graphics*, 14(1):33–38, 1996.

[138] N. Michaud-Agrawal, E. J. Denning, T. B. Woolf, and O. Beckstein. MDAnalysis: A toolkit for the analysis of molecular dynamics simulations. *Journal of Computational Chemistry*, 32(10):2319–2327, 2011.

[139] B. G. Levine, J. E. Stone, and A. Kohlmeyer. Fast analysis of molecular dynamics trajectories with graphics processing units - Radial distribution function histogramming. *Journal of Computational Physics*, 230(9):3556–3569, 2011.

[140] R. J. Kirkpatrick, A. G. Kalinichev, and J. Wang. Molecular dynamics modelling of hydrated mineral interlayers and surfaces: structure and dynamics. *Mineralogical Magazine*, 69(3):289–308, 2005.

[141] A. Einstein. Über die von der molekularkinetischen Theorie der Wärme geforderte Bewegung von in ruhenden Flüssigkeiten suspendierten Teilchen. *Annalen der Physik*, 322(8):549–560, 1905.

[142] I. C. Bourg and C. I. Steefel. Molecular Dynamics Simulations of Water Structure and Diffusion in Silica Nanopores. *The Journal of Physical Chemistry C*, 116(21):11556–11564, 2012.

[143] T. Giorgino. Computing diffusion coefficients in macromolecular simulations: the Diffusion Coefficient Tool for VMD. *Journal of Open Source Software*, 4(41):1698, 2019.

[144] G. Kikugawa, S. Ando, J. Suzuki, Y. Naruke, T. Nakano, and T. Ohara. Effect of the computational domain size and shape on the self-diffusion coefficient in a Lennard-Jones liquid. *The Journal of Chemical Physics*, 142(2):024503, 2015.

[145] K. Krynicki, C. D. Green, and D. W. Sawyer. Pressure and temperature dependence of self-diffusion in water. *Faraday Discussions of the Chemical Society*, 66:199, 1978.

[146] J. D. Smith. Energetics of Hydrogen Bond Network Rearrangements in Liquid Water. *Science*, 306(5697):851–853, 2004.

[147] R. J. Gowers and P. Carbone. A multiscale approach to model hydrogen bonding: The case of polyamide. *The Journal of Chemical Physics*, 142(22):224907, 2015.

[148] C. Qi, L. Liu, J. He, Q. Chen, L.-J. Yu, and P. Liu. Understanding Cement Hydration of Cemented Paste Backfill: DFT Study of Water Adsorption on Tricalcium Silicate (111) Surface. *Minerals*, 9(4):202, 2019.

[149] J. Huang, B. Wang, Y. Yu, L. Valenzano, M. Bauchy, and G. Sant. Electronic Origin of Doping-Induced Enhancements of Reactivity: Case Study of Tricalcium Silicate. *The Journal of Physical Chemistry C*, 119(46):25991–25999, 2015.

[150] J. Huang, L. Valenzano, T. V. Singh, R. Pandey, and G. Sant. Influence of (Al, Fe, Mg) Impurities on Triclinic Ca3SiO5: Interpretations from DFT Calculations. *Crystal Growth & Design*, 14(5):2158–2171, 2014.

[151] G. Tocci and A. Michaelides. Solvent-Induced Proton Hopping at a Water-Oxide Interface. *The Journal of Physical Chemistry Letters*, 5(3):474–480, 2014.

[152] O. Björneholm, M. H. Hansen, A. Hodgson, L.-M. Liu, D. T. Limmer, A. Michaelides, P. Pedevilla, J. Rossmeisl, H. Shen, G. Tocci, E. Tyrode, M.-M. Walz, J. Werner, and H. Bluhm. Water at Interfaces. *Chemical Reviews*, 116(13):7698–7726, 2016.

[153] B. F. Ngouana-Wakou, P. Cornette, M. C. Valero, D. Costa, and P. Raybaud. An Atomistic Description of the γ-Alumina/Water Interface Revealed by Ab Initio Molecular Dynamics. *The Journal of Physical Chemistry C*, 121(19):10351–10363, 2017.

[154] J. M. Rimsza, J. Yeon, A. C. T. van Duin, and J. Du. Water Interactions with Nanoporous Silica: Comparison of ReaxFF and ab Initio based Molecular Dynamics Simulations. *The Journal of Physical Chemistry C*, 120(43):24803–24816, 2016.

[155] Á. Cimas, F. Tielens, M. Sulpizi, M.-P. Gaigeot, and D. Costa. The amorphous silica–liquid water interface studied by ab initio molecular dynamics (AIMD): local organization in global disorder. *Journal of Physics: Condensed Matter*, 26(24):244106, 2014.

[156] S. Laporte, F. Finocchi, L. Paulatto, M. Blanchard, E. Balan, F. Guyot, and A. M. Saitta. Strong electric fields at a prototypical oxide/water interface probed by ab initio molecular dynamics: MgO(001). *Physical Chemistry Chemical Physics*, 17(31):20382–20390, 2015.

[157] M.-S. Lee, B. P. McGrail, R. Rousseau, and V.-A. Glezakou. Structure, dynamics and stability of water/scCO2/mineral interfaces from ab initio molecular dynamics simulations. *Scientific Reports*, 5(1), 2015.

[158] L. Liu, M. Krack, and A. Michaelides. Density Oscillations in a Nanoscale Water Film on Salt: Insight from Ab Initio Molecular Dynamics. *Journal of the American Chemical Society*, 130(27):8572–8573, 2008.

[159] S. V. Churakov. Structure of the interlayer in normal 11 å tobermorite from an ab initio study. *European Journal of Mineralogy European Journal of Mineralogy*, 21(1):261–271, 2009.

[160] S. V. Churakov. Structural position of H2O molecules and hydrogen bonding in anomalous 11 A tobermorite. *American Mineralogist*, 94(1):156–165, 2009.

[161] S. V. Churakov and C. Labbez. Thermodynamics and Molecular Mechanism of Al Incorporation in Calcium Silicate Hydrates. *The Journal of Physical Chemistry C*, 121(8):4412–4419, 2017.

[162] K. Leung and S. B. Rempe. Ab initio rigid water: Effect on water structure, ion hydration, and thermodynamics. *Physical Chemistry Chemical Physics*, 8(18):2153, 2006.

[163] S. Woutersen and H. J. Bakker. Ultrafast Vibrational and Structural Dynamics of the Proton in Liquid Water. *Physical Review Letters*, 96(13), 2006.